



1 **A Dissertation Submitted to**
2 **Shanghai Jiao Tong University for the degree of**
3 **Doctor of Philosophy in Physics**

4
5
6 Search for new phenomena in dijet events with
7 quark/gluon tagger using the ATLAS detector

8
9
10
11
12 Wanyun Su

13
14
15
16
17 Tsung-Dao Lee Institute
18 Shanghai Jiao Tong University
19 Shanghai, P.R.China
20 August 28, 2023

21

22



23

申请上海交通大学博士学位论文

24

25

26

在 ATLAS 双喷注末态中利用 夸克/胶子标定寻找新粒子

27

28

29

30

作者：苏琬云

31

导师：李数、Shih-Chieh Hsu (University of Washington,
Seattle)

32

33

李政道研究所
上海交通大学

34

35

36

37

2023 年 8 月 28 日

38

39

上海交通大学

学位论文原创性声明

40 本人郑重声明：所呈交的学位论文，是本人在导师的指导下，独立进行研究
41 工作所取得的成果。除文中已经注明引用的内容外，本论文不包含任何其他个人
42 或集体已经发表或撰写过的作品成果。对本文的研究做出重要贡献的个人和集体，
43 均已在文中以明确方式标明。本人完全知晓本声明的法律后果由本人承担。

44 学位论文作者签名：
日期： 年 月 日

45
46

47

48

上海交通大学

学位论文使用授权书

49 本人同意学校保留并向国家有关部门或机构送交论文的复印件和电子版，允
50 许论文被查阅和借阅。

51 本学位论文属于：

- 52 公开论文
53 内部论文，保密 1年 / 2年 / 3年，过保密期后适用本授权书。
54 秘密论文，保密 ____ 年（不超过 10 年），过保密期后适用本授权书。
55 机密论文，保密 ____ 年（不超过 20 年），过保密期后适用本授权书。
56 （请在以上方框内选择打“√”）

57

58 学位论文作者签名： 指导教师签名：
日期： 年 月 日 日期： 年 月 日

摘要

摘要

60 关键词：

61

ABSTRACT

62

ABSTRACT

63

64 The physics analyses presented in this PhD dissertation search for new physics be-
65 yond the Standard Model (BSM) in the dijet mass distribution using an integrated lumi-
66 nosity of 140 fb^{-1} of proton-proton collisions with a centre-of-mass energy at 13 TeV
67 recorded by the ATLAS detector. This analysis aims at searching for the evidence of
68 the BSM resonances in three different spectra: the untagged dijet invariant mass, one
69 gluon-tagged and two gluon-tagged channels. In order to increase the sensitivity to ob-
70 serve new resonances that preferentially decaying to one or more gluons, a gluon-tag
71 method based on the number of associated particle tracks is employed. Jets originating
72 from quarks and gluons can be identified using quark/gluon tagger. Two taggers are in-
73 vestigated: one tagger based on the number of charged tracks associated with the jets,
74 while the other employs a boosted decision tree to combine various jet substructure ob-
75 servables. Differences between data and Monte Carlo simulation of tagging efficiency
76 are provided. A matrix method is performed on data to retrieve the quark/gluon fraction
77 from quark/gluon-enriched subsamples, defined by the pseudorapidity of the jet. In the
78 analysis, the quantum chromodynamics (QCD) background is estimated by the statistical
79 framework which parameterised the dijet mass spectrum. Upper limits then are set at the
80 95% confidence level on a variety of theories of BSM physics and a model-independent
81 generic Gaussian shape signal.

82

83 **KEY WORDS:** Standard Model, ATLAS, calibration, jet tagging

Contents

85

1 Introduction

86 Over the past seventy years, the theories and discoveries of thousands of physi-
87 cists have developed a notable insight into the fundamental structure of matters, called
88 fundamental particles, which are governed by four fundamental forces. One of the best
89 understandings of how these particles and three of the forces interact with each other is
90 encapsulated in the Standard Model (SM) of particle physics. Developed in the early
91 1970s, it has been successfully proved by almost all experimental results. The huge
92 success of the discovery of Higgs Boson in 2012 predicted by the SM was awarded the
93 Nobel Prize in Physics in 2013. The SM has become established as a well-tested physics
94 theory.

95 Although the SM accurately describes the phenomena within its domain, there are
96 still theoretical flaws that prevent some fundamental physical phenomena from being
97 fully explained by the SM. First of all, the model contains many parameters that cannot
98 be derived from calculations alone but must be determined by experiment. In 1998, the
99 Japanese Super Kamioka neutrino detector published results on neutrino oscillations that
100 suggested the neutrinos have a non-zero rest mass, which did not match the prediction
101 made by the SM. Besides, the existence of gravity and dark matter has not yet been
102 described by the SM theory.

103 Many models of physics beyond the Standard Model (BSM) predict the presence of
104 new particles that couple to quarks and/or gluons. Such particles could be produced in
105 proton-proton collisions at the Large Hadron Collider (LHC) and then decay into quarks
106 and gluons, during this process two hadronic jets are created, which then can be seen by
107 the detector. The new energy regime ($\sqrt{s} = 13$ TeV) with an integrated luminosity of 140
108 fb^{-1} provided by the LHC opens a window to search for BSM particles.

109 In the SM, these dijet events are generated mainly by quantum chromodynamic
110 (QCD) processes and appeared to be a smoothly decreasing invariant mass (m_{jj}) dis-
111 tribution, however, a new particle that decays into quarks or gluons could appear as a
112 resonance in the m_{jj} spectrum. If the resonant samples can be classified based on the
113 type of parton that initiated the jets, the sensitivity of the search for such resonances
114 could be largely increased. Hence, classifying jets as initiated from a quark or a gluon
115 can be effective for improving SM measurements and searches for BSM physics.

116 Recent developments in quark/gluon (q/g) tagging have resulted from advances in

Introduction

the theoretical, phenomenological and experimental understanding of q/g tagging as well as the development of powerful machine learning techniques that can utilize the entire jet internal radiation pattern. The calibration of q/g taggers is performed to account for the systematics of searching results.

This thesis is structured as follows. Chapter 2. describes the theoretical framework of the SM, its limitations and various potential extensions beyond it. An introduction to the LHC and the ATLAS detector is given in Chapter 3. Jet reconstructions and calibrations are briefly described in Chapter 4. The quark/gluon tagger definitions and the selection criteria used to generate the various event samples employed in the discriminant extraction, the method and the scale factor results are presented in Chapter 5. The details of the search for new resonances in the dijet spectrum and the limit setting results are shown in Chapter 6. In the end, the conclusion and outlook of the research are presented in Chapter 7.

130

2 The theory framework

131 2.1 The Standard Model

132 The Standard Model of particle physics, which describes the three fundamental
 133 interactions - strong, weak and electromagnetic interactions - and the fundamental par-
 134 ticles that make up all matter, is the most successful theory of particle physics known.
 135 The SM divides particles into two categories, fermions and bosons, based on the values
 136 of their spin: fermions are the particles that makeup matter, such as electrons in leptons,
 137 quarks and neutrinos, which have half-integer spin; bosons are the particles that trans-
 138 mit forces, such as photons and mesons that transmit electromagnetic forces, gluons that
 139 transmit strong nuclear forces, W and Z that transmit weak nuclear forces, have integer
 140 spin. Different properties shown in fermions and bosons are due to the difference in
 141 spin. According to the spin-statistics theorem, fermions obey the Pauli exclusion princi-
 142 ple, whereas bosons do not, thus bosons do not have a theoretical limit on their spatial
 143 density.

144 The SM is a paradigm of a quantum field theory which provides the mathematical
 145 framework for it. The Lagrangian controlled the dynamics and kinematics of the system
 146 satisfies the $SU(3) \times SU(2)_L \times U(1)_Y$ gauge symmetry, in which $U(1)_Y$ corresponds to
 147 a particle B with weak hypercharge Y . $SU(2)_L$ corresponds to particles W_α ($\alpha = 1, 2,$
 148 3) with weak isospin T and only left-handed chiral particles. The electroweak force
 149 which unifies the electromagnetism and the weak interaction as a Yang-Mills field is
 150 represented by the group $SU(2)_L \times U(1)_Y$, mathematically. In SM, the Z^0 boson and the
 151 photon (γ) are given by:

$$\begin{pmatrix} \gamma \\ Z^0 \end{pmatrix} = \begin{pmatrix} \cos \theta_W & \sin \theta_W \\ -\sin \theta_W & \cos \theta_W \end{pmatrix} \begin{pmatrix} B \\ W_3 \end{pmatrix} \quad (2.1)$$

152 where θ_W is the weak mixing angle.

153 The charged massive bosons W^\pm are given by W_1 and W_2 :

$$W^\pm = \frac{1}{\sqrt{2}} (W_1 \mp iW_2) \quad (2.2)$$

154 $SU(3)$ corresponds to eight vector fields A^α ($\alpha = 1, 2, \dots, 8$) representing gluon fields,
 155 which are vector gauge bosons that carry the colour charge of the strong interaction and

156 mediate between quarks in QCD. The Higgs boson, unlike all other known bosons such
 157 as the photon, is a scalar boson and has a non-zero average value in vacuum. It is resulted
 158 from the process of spontaneous symmetry breaking. The Higgs mechanism explains the
 159 generation of the property "mass" for gauge bosons. At a critical temperature, the Higgs
 160 field introduces a vacuum expectation value that causes spontaneous symmetry breaking
 161 during interactions, leads the bosons it interacts with acquire masses. A Yukawa coupling
 162 is used in the SM to describe the interaction between the Higgs field and fundamental
 163 fermions, explain the generation of the masses of fermions.

164 This chapter therefore focuses on the present SM, various extensions and variants
 165 of the SM that have been proposed by theoretical physicists are explored in Section 2.2.

166 **2.1.1 Quantum chromodynamics**

167 QCD is the theory of the strong interaction between quarks and gluons, and it is a
 168 fundamental component of the SM of particle physics. Satisfying the $SU(3)$ symmetry
 169 group invariant, QCD is a non-abelian gauge theory, over the years, QCD has collected
 170 a huge body of experimental evidence, proved that it has been a successful application
 171 from a quantum field theory.

172 The Lagrangian of QCD can be expressed as:

$$\mathcal{L}_{\text{QCD}} = \bar{\psi}_i \left(i\gamma^\mu (D_\mu)_{ij} - m\delta_{ij} \right) \psi_j - \frac{1}{4} G_{\mu\nu}^a G_a^{\mu\nu} \quad (2.3)$$

173 where ψ_i is the quark field in the fundamental representation of the $SU(3)$ gauge group,
 174 indexed by i and j running from 1 to 3; m corresponds to the quark mass; the γ^μ are Dirac
 175 matrices relating the spinor representation to the vector representation of the Lorentz
 176 group.

177 D_μ is defined as the gauge covariant derivative:

$$(D_\mu)_{ij} = \partial_\mu \delta_{ij} - ig_s (T_a)_{ij} \mathcal{A}_\mu^a \quad (2.4)$$

178 which couples the quark field with a coupling strength g_s to the gluon fields via the
 179 infinitesimal $SU(3)$ generators T_a . By including the Gell-Mann matrices λ_a ($a=1\dots 8$), an
 180 explicit representation of T_a is defined by $T_a = \lambda_a/2$.

181 The gauge invariant gluon field strength tensor $G_{\mu\nu}^a$ is given by:

$$G_{\mu\nu}^a = \partial_\mu A_\nu^a - \partial_\nu A_\mu^a + g_s f^{abc} A_\mu^b A_\nu^c \quad (2.5)$$

182 where A_μ^a are the gluon fields, indexed by a, b and c running from 1 to 8; f^{abc}
183 are the structure constants of $SU(3)$. The coupling strength g_s can be referred to strong
184 coupling constant α_s :

$$\alpha_s = \frac{g_s^2}{4\pi} \quad (2.6)$$

185 There are some salient properties that QCD exhibits:

186 Colour confinement

187 This is a consequence of the force between two colour-charged particles that can
188 not be isolated in a condition that below the Hagedorn temperature of approxi-
189 mately 2 terakelvin. To separate two quarks in a hadron, extremely high energy
190 is required, leading to the creation of a quark-antiquark pair that formed a pair of
191 hadrons rather than a single hadron. In addition, glueballs which are formed only
192 of gluons are colourless and also consistent with confinement, causing difficulty
193 in identification in experiments.

194 Asymptotic freedom and the running coupling

195 This is a feature of QCD that demonstrates the strong interactions between quarks
196 and gluons become asymptotically weaker as the energy scale of them increases
197 and the corresponding length scale decreases. This is opposite to the behaviour of
198 colour-charged particles at low energies where the confinement of quarks and glu-
199 ons exhibits. At high energy, the coupling decreases logarithmically as a function
200 of momentum transfer Q :

$$\alpha_s(Q^2) \stackrel{\text{def}}{=} \frac{g_s^2(Q^2)}{4\pi} \approx \frac{1}{\beta_0 \ln(Q^2/\Lambda^2)} \quad (2.7)$$

201 where β_0 is a one-loop beta function in QCD and has the dependence of the cou-
202 pling parameter g_s . The quantity Λ is referred to QCD scale that is measured
203 in processes where the strong coupling constant and other measurables vary with
204 momentum transfer Q . However, this is only effective at leading order (LO). By

205 including higher order terms, the calculation expanded in order of α_s resulted in
 206 more complexity and less significance as the scale of Q increases. On the other
 207 hand, as Q tends to be infinite large, the coupling strength becomes zero thus the
 208 behaviors of quarks are asymptotically free. These variation of coupling α_s under
 209 the different scales of energy in QCD is described as the running coupling.

210 The calculation of matrix element in QCD can be rather complex as more and more
 211 perturbative contributions are considered, which requires the application of complicated
 212 integrals over a large number of variables. A Feynman diagram is used as a representa-
 213 tion of the expressions of these integrals pictorially and an improvement of undertaking
 214 the critical calculations.

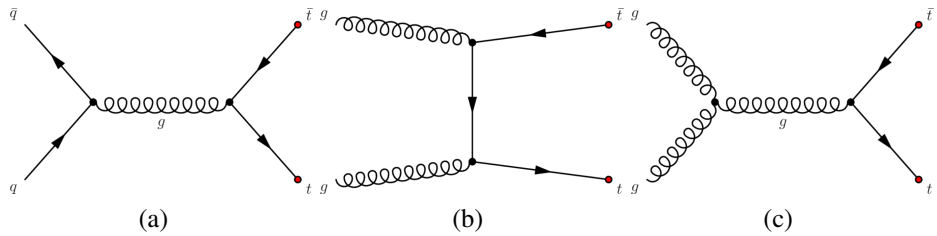


Figure 2.1 Feynman diagrams of strong interaction in top-antitop quarks production via (a) one gluon exchange in quark-antiquark annihilation, gluon-gluon fusion in (b) t-channel and (c) s-channel.

215 With more interactions points involved in, more complicated the calculations be-
 216 come. The effects of self-interactions between particles themselves can happen by pro-
 217 ducing a virtual particle which is restricted by the uncertainty principle, represented as a
 218 loop in a Feynman diagram. The accuracy of the calculation has dependency on the cou-
 219 pling α_s and is contributed to a fraction at each order. By including an infinite number
 220 of virtual particles, the calculations are led to divergent and infinite. A set of techniques
 221 named renormalization are employed in solving the infinities showed up in the calcu-
 222 lations, by which the infinite self-interactions are parameterized by re-scaling them as
 223 finite values to compensate the effects. The ultraviolet divergence that occurs from inte-
 224 grating the contributions at extreme high energy is represented by renormalization scale
 225 μ_R , on the contrast, μ_F represents the condition of an integral diverges at infinitesimal
 226 energy.

227 2.2 Physics beyond the Standard Model

228 2.2.1 H'

229 Many extensions of the SM predict the existence of new heavy Higgs-boson-like
230 particles. 2HDMs are a wide set of models in which the couplings scale with Yukawa
231 couplings thus leads to a relatively small branching ratio of the scale H or pseudoscalar
232 A to gluons. New particles that decay into photons are also predicted by BSM and have
233 a branching ratio to gluons. Besides, some classes of models predicted the new particle
234 decaying into photons with a branching ratio to gluons, where the relative branching
235 ratio of photons to gluons is model-dependent. Models with new heavy fermions through
236 scalar decays to gluons are also exist.

237 The motivation of a model-independent di-gluon resonances is that the m_{jj} back-
238 ground is dominated by valence quark scattering at high energy, which leads gluon tag-
239 ging particularly effective. At higher energy, there is higher jet constituent multiplicity
240 that makes gluon tagging becomes more effective, thus the search in this analysis could
241 gain the most from gluon tagging.

242 For this analysis, a high mass simulated $SU(3)$ singlet scalar H' decaying into a
243 pair of gluons is used. The physical width in practice is set to be narrow to be model-
244 dependent and thus the m_{jj} width is set by the detector resolution.

245 2.2.2 String

246 A mathematical framework named string theory has contributed to a variety of prob-
247 lems in the SM such as the existence of gravity, it offers a unified description of particle
248 physics and gravity. String theory handles point-like particles as one-dimensional objects
249 called strings and demonstrates the behaviours of these strings propagating through time
250 and space. By regarding particles as infinitesimal vibrating strings, the charge, mass,
251 and other properties of them are determined by the vibration or twist of the strings. A
252 dynamical object called brane is employed to generalize the representation of a point
253 particle to higher dimensions such that a string can be regarded as a brane of dimension
254 one and can propagate through time and space under the principles of quantum mechan-
255 ics. Among them, a so-called Dirichlet membrane (D-brane) is widely used as the open
256 strings satisfy the Dirichlet boundary conditions.

257 In this analysis, we consider type-II string theory which includes a D-brane local-

258 ized in $p + 3$ partial dimension: D p -brane, compactified on a six-dimensional torus. The
259 choice of the string mass scale M_s is to be smaller than the 4-dimensional Planck scale to
260 keep the coupling small, at the expense of introducing $9 - p$ large transverse dimensions
261 felt only by gravity. Only the fundamental string scale in the TeV range is what this
262 analysis is interested in.

263 By considering the main subprocesses in dijet production that are independent of
264 the details of the compactification. Amplitudes, which include $2 \rightarrow 2$ scattering processes
265 involving two gluons and two quarks, or four gluons, are independent of the details of the
266 compactification such as the configuration of branes. This model independence makes it
267 possible to compute the string corrections to QCD dijet processes.

268 **2.2.3 Quantum Black Holes**

269 Quantum Black Holes (QBH), also called micro black holes, are regarded as hy-
270 pothetical mini (less than a solar mass unit) black holes that dominated by quantum
271 mechanical effects. Some hypotheses predict that QBH could be produced at energies as
272 low as the TeV range, which can be generated in particle accelerators such as the LHC
273 and can be observed through the particles that are emitted by the process of Hawking
274 radiation.

275 In the simplest scenario, the decay of QBH via Hawking radiation can be approx-
276 imately described as isotropic decay to a many-particle final state. The threshold of
277 quantum-gravity energy scale M_D is set to be well below the the actual thermal black
278 hole production threshold for gravitational interactions so that two-body states in final
279 states are the dominant, a resonance-like result is expected in predominantly two-body
280 final states as jets near M_D . Such isotropic final states is aimed as probes of quantum
281 gravitational effects in this dijet analysis.

282

3 The ATLAS Experiment

283 3.1 The Large Hadron Collider

284 The LHC, built by European Organization for Nuclear Research (CERN) located in
 285 Geneva, Switzerland, is the largest circular particle accelerator in the world. The goal of
 286 it is to probe the various theoretical predictions made by physicists.

287 It consists superconducting magnets that construct a 27-kilometer ring lying in the
 288 tunnel under the ground. Inside the LHC, two beams made of protons or ions are accel-
 289 erated to extreme high speed in opposite direction in individual vacuum pipes then made
 290 into collision by a strong magnetic field within the structures.

291 The LHC is the last section of the CERN accelerator complex where a series of
 292 machines accelerates the particles to increasingly higher and higher energies. The highest
 293 energies of beams are reached at the LHC.

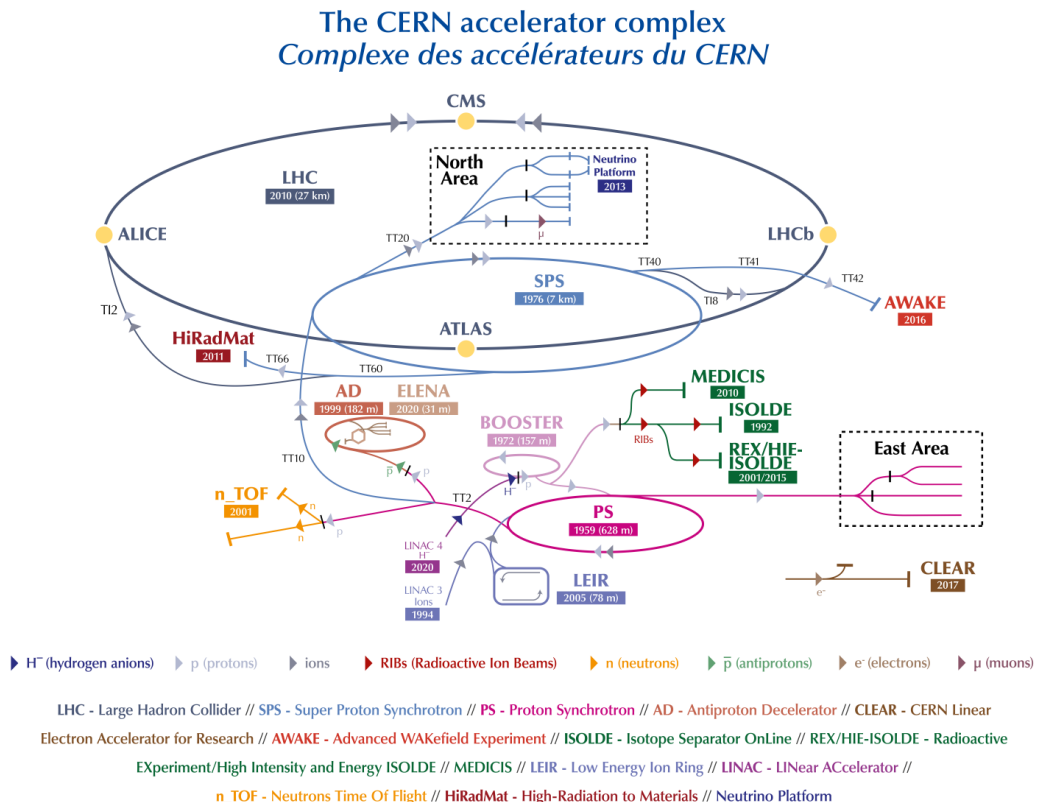


Figure 3.2 The CERN accelerator complex

294 Seven detectors are placed around four collision points in the collider. Different
 295 types of particles are accelerated according to the research, the main beams are protons,
 296 but the LHC also run beams of heavy ions as lead–lead collision or proton–lead collisions.

297 The energy of particles is increased by a series of processes before being injected
 298 into the main accelerator. For a proton-proton collision, negative hydrogen ions are gen-
 299 erated by the linear particle accelerator Linac4 at 160 MeV then injected into the Proton
 300 Synchrotron Booster, where protons are obtained by stripping electrons away from the
 301 atom and accelerated to 2 GeV. After entered the Proton Synchrotron the energy of the
 302 protons is 26 GeV, and then their energies are increased in Super Proton Synchrotron to
 303 450 GeV before they are finally injected into the main ring.

304 One of the characteristics that defines the power of an accelerator is the centre-of-
 305 mass energy, which represents the total momentum of the system and thus indicates the
 306 total mass of potential new particles as well as probes the internal structure of known
 307 particles under the law of energy invariant within the system. In 2010, the first collisions
 308 were made at an energy of 3.5 TeV each beam, later in 2018, an energy of 6.5 TeV per
 309 beam was achieved, resulted in the centre-of-mass energy of 13 TeV where the protons
 310 moved at a 99.9% speed of light. It took less than 90 μ s for photons to go through the
 311 whole LHC ring.

312 Other quantities such as luminosity, denoted as \mathcal{L} , also represents the performance
 313 of an accelerator. It is the rate of interactions during a certain period of time and can be
 314 expressed as:

$$\mathcal{L} = \frac{N^2 f_{rev}}{4\pi \sigma_x \sigma_y} \quad (3.1)$$

315 where N is the number of particles in a bunch, in the case that a beam has Gaussian
 316 distribution and has brunches crossing frecuency f_{rev} . σ_x and σ_y denote as transverse
 317 beam widths in the x- and y-plane. The luminosity takes the units of $\text{cm}^{-2} \cdot \text{s}^{-1}$.

318 The total number of physics events detected can be express as:

$$N_{\text{event}} = \sigma_{\text{event}} \cdot \int \mathcal{L} dt \equiv \sigma_{\text{event}} \cdot L \quad (3.2)$$

319 where L is the integrated luminosity with respect to time, σ_{event} is referred to the
 320 cross section of a specific physics process. The integrated luminosity takes the units of
 321 cm^{-2} which equals to the unit femtobarn (fb).

At the LHC, thousands of magnets around the accelerator are operated at a very low temperature of 271.3°C to maintain its superconducting state which allow them to conduct electricity without loss of energy. Hence, a system of liquid helium is used for cooling the accelerator and supply services.

Besides, superconducting radio frequency cavities which resonate electromagnetic fields are employed to accelerate the protons. Instead of having continuous beams, the protons are made into bunches, so that the collisions are taken place at discrete intervals between two beams with 115 billion protons per bunch at the frequency of 25 ns.

3.2 The ATLAS detector

The ATLAS detector is the largest volume detector ever constructed for general-purpose particle research at the LHC. It has the shape of a cylinder with 44 meters long, 7000 tonnes in weight and 25 meters in diameter, sitting in a cavern underground. It is designed to collect evidence of the properties of SM and search for new predictions made by particle physics beyond the SM.

To record the energy, momentum and trajectory of particles after collisions, the detector consisting of 6 different detecting subsystems placed in layers surrounding the interaction point to measure them individually and effectively.

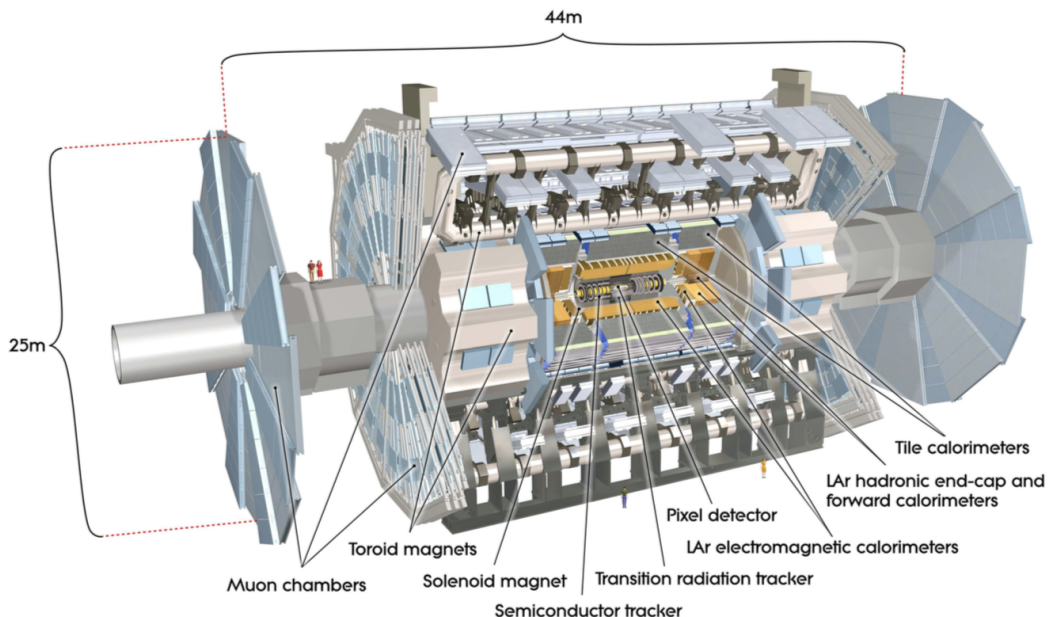


Figure 3.3 Cut-away view of the ATLAS detector

339 An overall layout of the ATLAS detector is shown in Figure 3.3.

340 **3.2.1 Inner detector**

341 Charged particles above a certain p_T threshold are detected by the ATLAS Inner
 342 Detector (ID) which immersed in a 2 T solenoidal field, covered the pseudorapidity range
 343 $|\eta| < 2.5$. Appearing as tracks in the ID, an excellent momentum resolution as well as
 344 both primary and secondary vertex of them are provided by the ID. Within the range
 345 $|\eta| < 2.0$, electron identification is also provided.

346 The layout of the ID is shown in Figure 3.4 in cylindrical coordinate: $r = \sqrt{x^2 + y^2}$,
 where x -axis alongside the LHC ring and y -axis is perpendicular to the x -axis.

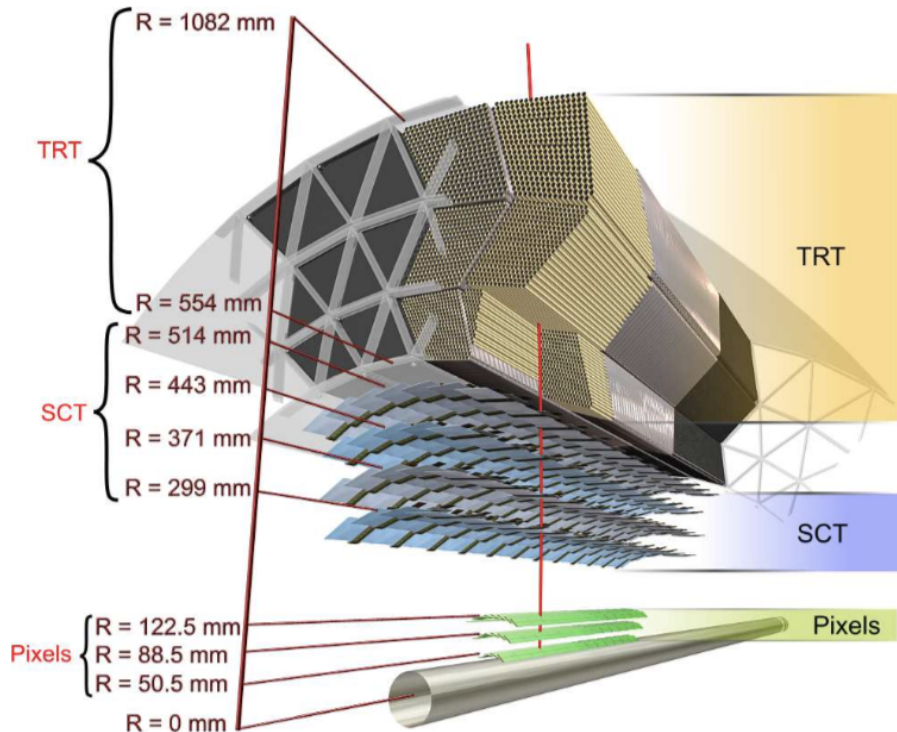


Figure 3.4 Cut-away view of the ATLAS ID. Sensors and structural elements traversed by a charged track of 10 GeV p_T in the barrel inner detector along with their envelopes in r .

347
 348 A cylindrical container around the ID has a length of 3512 mm each way and a
 349 radius of 1150 mm, tracks of 10 GeV traverse the sensors and structural elements in the
 350 barrel and end-cap regions, respectively.

351 Within the inner region, a series of discrete space points provided by the silicon

352 pixel detector and stereo pairs of silicon microstrip semiconductor tracking (SCT) lay-
353 ers gives high-resolution pattern recognition abilities. By increasing radial distances,
354 the transition radiation tracker (TRT) provides extra pattern recognition and momentum
355 resolution capabilities.

356 **The pixel detector**

357 A series of high-granularity measurements is provided by the pixel detector which
358 is composed of the innermost sub-detector of the ID, it is designed as close to the
359 interaction point as possible. Three sub-sections: two end-cap perpendicular to the
360 beam axis and a barrel alongside the beam axis as a concentric cylinder with four
361 layers (average radii of 33.25, 50.5, 88.5 and 122.5 mm, respectively) in it.

362 The innermost pixel layer (or B-layer, IBL) is essential to b-tagging performance
363 and supersymmetry searches as it cover the full acceptance of short-lived parti-
364 cles such as B hadrons and τ leptons from the beginning of Run-2 to enhance the
365 measurement of the secondary vertex. Besides, a new readout sensor and chip
366 responsible for higher radiation damage and higher hit rate, respectively, is em-
367 ployed in the IBL compared to the other three layers in the barrel region. A new
368 n-in-n planar and 3D silicon sensors with hit efficiency of greater than 97% is de-
369 veloped as well. The better impact parameter resolution is achieved by reducing
370 the pixel size of the chip down to $50 \times 250 \mu\text{m}^2$. Around 80 million readout sec-
371 tions counting them all provide the great hit resolution of $10 \mu\text{m}$ in radius plane
372 and $115 \mu\text{m}$ alongside the z-axis in the pixel detector.

373 **The semiconductor tracker**

374 Surrounding the pixel detector is the SCT which encompasses silicon based semi-
375 conductor sensing components in barrel and end-cap geometries. Four silicon mi-
376 crostrip layers, located at radii of 300, 373, 447 and 520 mm, in the barrel region
377 of the SCT provide high granularity points. The mean size of each strip pitch is
378 $80 \mu\text{m}$ for the rectangular barrel sensors as daisy-chained with 6 cm-long. For
379 the end-cap sensors, nine disks cover $|\eta| < 2.5$ are chosen. As a result, there are
380 thus 768 readout strips with $6.36 \times 6.40 \text{ cm}^2$ in size in total, with additional two
381 strips at the edge of the sensor. 6.1 m^2 of silicon detectors with 6.2 million readout
382 channels as a whole integrated the SCT.

383 **The transition radiation tracker**

384 The outermost layer of the ID is the TRT which encompasses polyimide drift(straw)
385 tubes that designed to enable as much less wall thickness and material as possible
386 while maintaining the good experimental properties. With 4 mm in diameter and
387 150 cm in length, 73 layers of 144 cm alongside the beam with 50 thousands tubes
388 and 37 cm tubes consisting 160 tubes planes in the end-cap with 320 thousands
389 radial tubes.

390 The xenon-based gas filled up in a given tube provides the track hit of a particle as
391 it ionized as the emitting electrons drifting to the center wire of the tube volume.
392 An average of 36 hits per charged-particle track is given by the TRT, The result-
393 ing electrical signals are obtained by converting the drifting charge currents. In
394 total 420 thousands of electronics channels in which a good spatial resolution and
395 drift-time measurement are provided by the TRT, enhancing the precision mea-
396 surements of momentum in the ID.

397 **3.2.2 Calorimeters**

398 Outside of the ID lies the ATLAS calorimeters system which is designed to obtain
399 the energy lost of the particles that travel through the detector components. Multiple
400 layers of high-density material are placed to consume the energy of the incoming par-
401 ticles inside the materials and stop them from further moving. An “active” medium
402 is left inside the layers that allows experimental physicists measure the energy of those
403 particles.

404 Two types of calorimeters are employed in the ATLAS calorimeters system: the en-
405 ergy of electrons and photons are measured by the electromagnetic calorimeters as they
406 create reaction with matter. Hadronic showers that created by the interaction between
407 hadrons and atomic nuclei, are sampled by the hadronic calorimeters. Muons and neutrini-
408 nos can not be stopped by the calorimeters as they interact only weak force but the track
409 footprints could be seem in the calorimeters. The layout of the calorimeters is shown in
410 Figure 3.5.

411 The electromagnetic (EM) calorimeter covers a range of $|\eta| < 3.2$ by combining
412 the one barrel and two end-cap modules as cylindrical cryostat, with an outer radius of
413 2.25 m, an end-cap thickness of 0.632 m and a length of 3.17 m. The hadronic calorime-
414 ter covers the central barrel region of $|\eta| < 1.0$ and two extended barrels in a region of
415 $0.8 < |\eta| < 1.7$. with a radius of 2.28 m at the inside and 4.25 m at the outside. Fig-

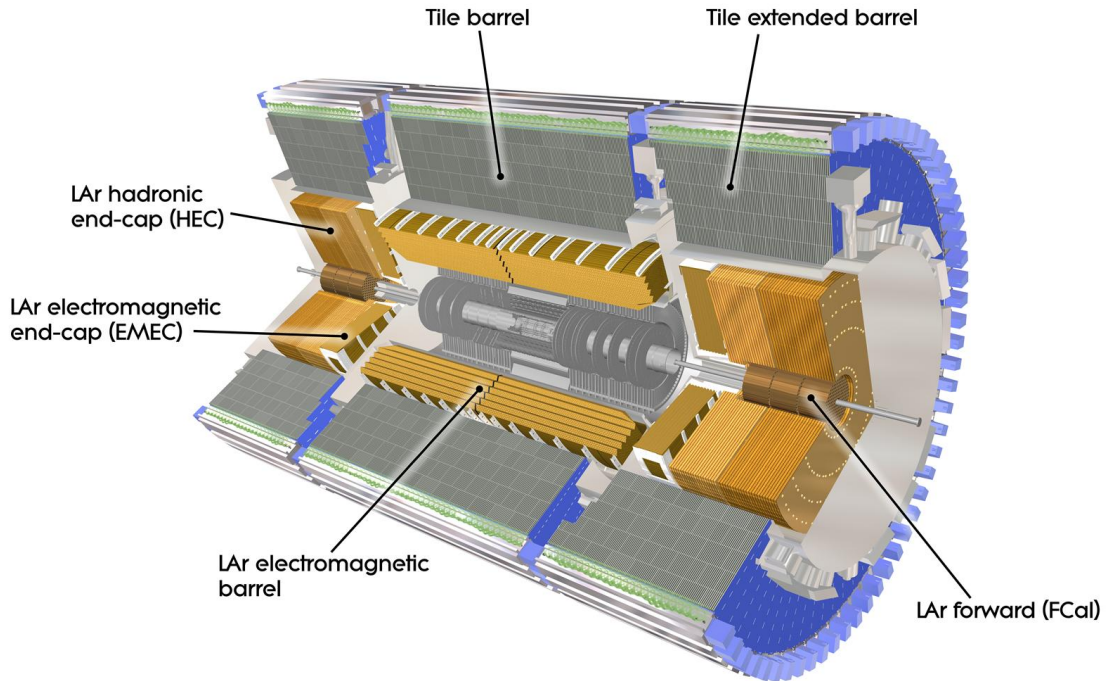


Figure 3.5 Outline of the ATLAS Run 2 trigger and data-acquisition system.

416 Figure 3.6 demonstrates the positions of the end-cap of the calorimeters including the EM
 417 and Hadronic calorimeters.

418 **The electromagnetic calorimeter**

419 The EM calorimeter that surrounds the ATLAS ID is designed for the high-
 420 granularity measurements of the energy of photons, electrons and hadrons with
 421 Liquid Argon (LAr) sandwiched between the multiple layers ionised. It converts
 422 the incoming particles into electric currents by absorbing the energy of these par-
 423 ticles as they interact with the metal with the bremsstrahlung phenomenon. A pair
 424 of electron-positron produced by an electron radiation in the EM calorimeter can
 425 initiate further electron-positron pairs (as showers) until the energy of the parti-
 426 cles fall below the certain threshold, the dominate process thus become ionisation
 427 in the LAr where drifting electrons are produced. Furthermore, the missing trans-
 428 verse energy can be obtained by subtracting the total energy of the known particles,
 429 which contributes to the analysis of neutrinos and new particles.

430 At -184 °C where the argon exists in liquid form, the calorimeter is kept as the

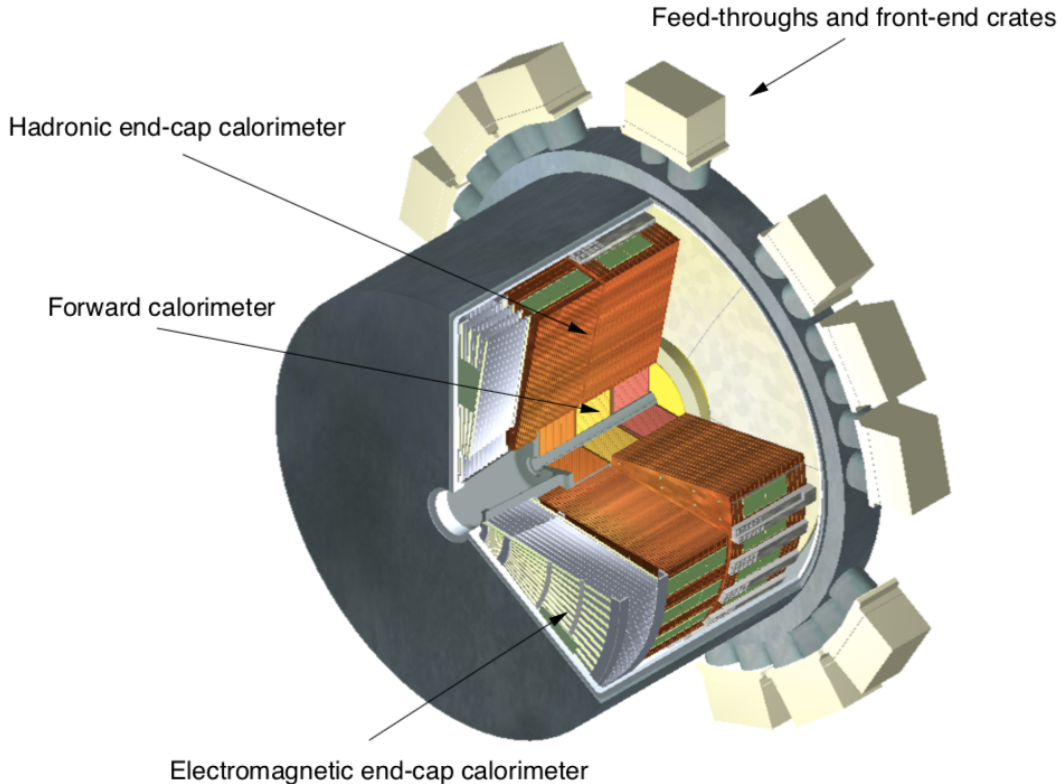


Figure 3.6 Cut-away view of an end-cap cryostat of the ATLAS calorimeter system.

431 cables that transverse electronic signals are sealed in vacuum and connected to the
 432 warmer area where located the readout system.

433 **The hadronic calorimeter**

434 Surrounded the EM calorimeter, lies the tile hadronic calorimeter where hadrons
 435 that contain strong force thus could not fully deposit their relatively large energy in
 436 the EM calorimeter are absorbed by the tile calorimeter. Steel and plastic scintillat-
 437 ing tiles are placed in layers in order to record the trajectories of incoming particles
 438 as hadronic showers are formed by the interactions of the particles with the ma-
 439 terials and emitting particles continue interacting with materials in the hadronic
 440 calorimeter and more particles are produced in steel layers. On the other hand,
 441 photons are produced by the plastic scintillators where electric currents are gained
 442 according to the energy of the particle.

443 By enveloping the EM calorimeter, a hadronic shower that contained EM showers
 444 can be fully absorbed by the great thickness in the hadronic calorimeter. Around

445 420 thousands of plastic scintillator tiles are placed in sync, leading a weight of
 446 2.9 thousands tonne in total.

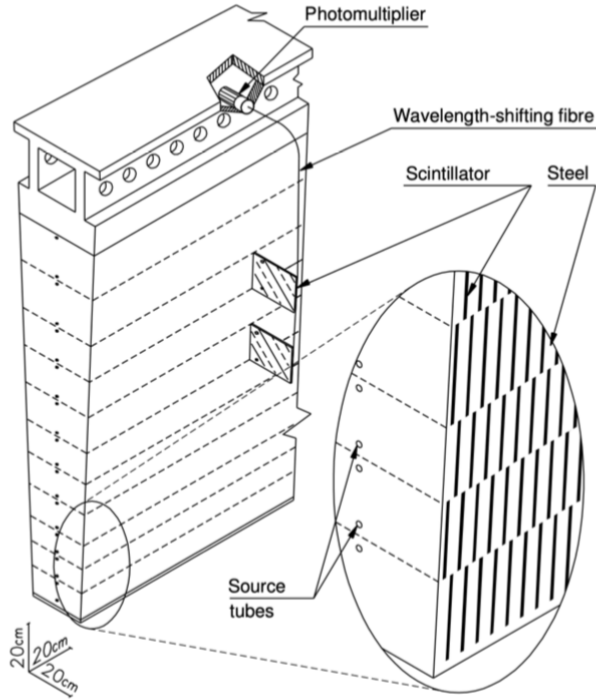


Figure 3.7 A schematic view of a tile calorimeter components of optical readout tiles and scintillating tiles.

447 As illustrated in Figure 3.7, photomultiplier tubes (PMT) are placed around the
 448 outer radii of the tile calorimeter and connected with wavelength-shifting fibres
 449 by which scintillation light is transferred. Projective geometry is designed for
 450 the whole readout system as the energy of most hadronic showers is deposited in
 451 the first or last two layers. Though the coarser granularity of the readout cells
 452 of hadronic calorimeter has been compared to the EM calorimeter, the hadronic
 453 calorimeter is qualified for the measurement of transverse momentum and jet re-
 454 construction.

455 In the forward regions, the hadronic calorimeters are integrated with LAr calorime-
 456 ters due to higher radiation exposition compared to the barrel regions. There are
 457 two calorimeters that were developed to tackle such issue: the hadronic end-cap
 458 calorimeter (HEC) that covers $1.5 < |\eta| < 3.2$ and the forward calorimeter (FCal)
 459 that covers $3.1 < |\eta| < 4.9$.

460 The HEC located further beside the EM end-cap calorimeter has two wheels in
461 each end-cap. LAr is used for filling up 8.5 mm between copper layers in the HEC,
462 by which the active medium is provided. The readout electrodes are provided in
463 separate drift zones in order to secure the stability of the whole system. The FCal
464 has three wheels placed alongside the z-direction: one electromagnetic layer (FCal
465 1) and two hadronic layers (FCal 2 and FCal 3). LAr is also used as an active
466 medium in all of the layers. As for the absorber, copper is employed in FCal 1 as
467 it has heat removal properties. Tungsten is used in both FCal 2 and FCal 3 in order
468 to constrain the lateral spread of hadronic showers.

469 **3.2.3 Muon spectrometer**

470 The muon spectrometer (MS), specially designed for the muon detection is located
471 in the outermost section of the ATLAS in order to provide sufficient measurement of
472 high-momentum muons which are almost "invisible" to the ID and calorimeters due to
473 little energy deposit when traveled through them. By deflecting the trajectories of
474 muons, the MS employs the magnetic field by a barrel toroid magnet system in $|\eta| < 1.4$
475 and end-cap toriod systems in $1.6 < |\eta| < 2.7$.

476 Four subsections of the MS: add up to 4000 separate muon chambers. Thin Gap
477 Chambers (TGC) and Resistive Plate Chambers (RPC) account for triggering and the
478 second coordinate measurement of muons. TGC is set at the end of the detector whereas
479 RPC which provides 5,000 V/mm electric field is placed in the central region. Monitored
480 Drift Tubes (MDT) is designed for the curve of muon tracks measurement with fine tube
481 resolution of 80 μm . Cathode Strip Chambers (CSC) accounts for measuring coordi-
482 nates precisely located at ends of detector with a fine resolution of 60 μm . Figure 3.8
483 demonstrates the MS with all four subsections. In total three separate points within the
484 muon trajectory are measured to reconstruct the momentum of the muon.

485 **3.2.4 Trigger and data acquisition**

486 At the LHC, approximately 1.7 billion proton-proton collisions occur per second at
487 an integrated luminosity of 140 fb^{-1} . However, many of these collisions are unlikely to
488 produce characteristics of interest. As a result, large numbers of events can be discarded
489 without affecting the search for new physics. The trigger and data acquisition systems
490 are introduced to eliminate the irrelevant data so that only events of suitable quality and

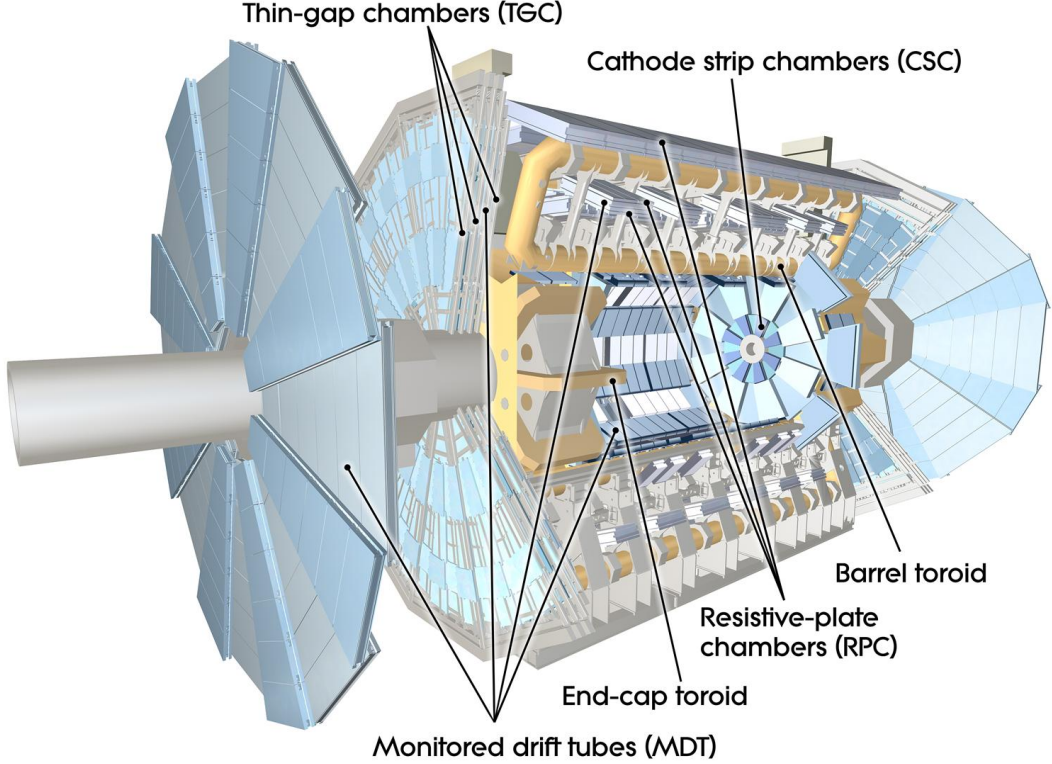


Figure 3.8 Cut-away view of the ATLAS Muons Spectrometer with subsections labeled.

491 quantity are recorded.

492 During the year of 2015-2018, the trigger system in ATLAS selected significant
 493 events in a two staged process, as illustrated in Figure 3.9: The first-level (L1) trigger is
 494 implemented on hardware, and reduced event rates from 40 MHz to 100 kHz in less than
 495 $2.5 \mu\text{s}$ right after the data happened. Working with the electrical information provided
 496 by the calorimeters and the MS, the L1 trigger employs custom-made electronics to
 497 filter and store the events in the readout sections as buffers before passing them to the
 498 High-Level trigger (HLT). Certain physics objects such as photons, jets and leptons are
 499 identified in the L1 trigger, in which energy depositions of electrons and photons in the
 500 EM calorimeter and jets in the hadronic calorimeter are provided. Information of tracks
 501 in high-momentum muons is recorded in the layers of the MS and forwarded to the L1
 502 trigger.

503 The events are further reduced from 100 kHz to 1 kHz in merely 250 microseconds
 504 by the second level trigger: HLT. Based on the offline software, the HLT utilize fast
 505 selection algorithms to analyse and reject events in the early stage, resulting in better

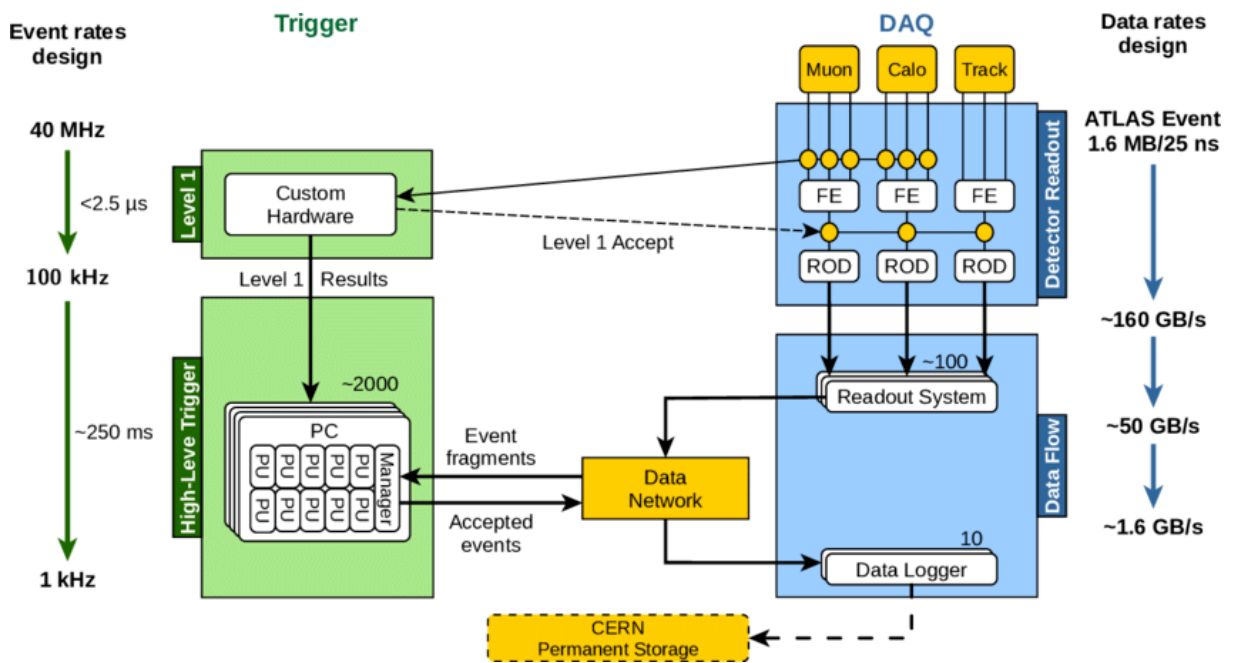


Figure 3.9 illustration of the ATLAS Run 2 trigger and data acquisition system.

506 precision and intense CPU usage of about 1.6 GB per second. The accepted data from
 507 the HLT will be passed to permanent storage at CERN via Data Logger.

508

4 Jets in ATLAS

509 In the LHC, a large number of quarks and gluons are produced during the inelastic
 510 proton-proton collisions, resulting in jets. These collimated outcome particles are hadro-
 511 nised because of colour confinement in the QCD process. As a result of this, only colour-
 512 neutral jets clustered by particles can be seen in the detector.

513 The information of jets is crucial to most of the analysis such as the measurements
 514 of the SM particles and searches for the BSM phenomena. Good qualities of jets, for
 515 example the high efficiency of jet reconstruction, jet energy calibration including energy
 516 scale and energy resolution, are thus important to the analysis.

517 **4.1 Jet reconstruction**

518 Jets are defined in two way: Monte Carlo (MC) simulated jets at particle level and
 519 detector level jets with the information from the ID and calorimeters. The production
 520 and hadronisation processes of jets are illustrated in Figure 4.10.

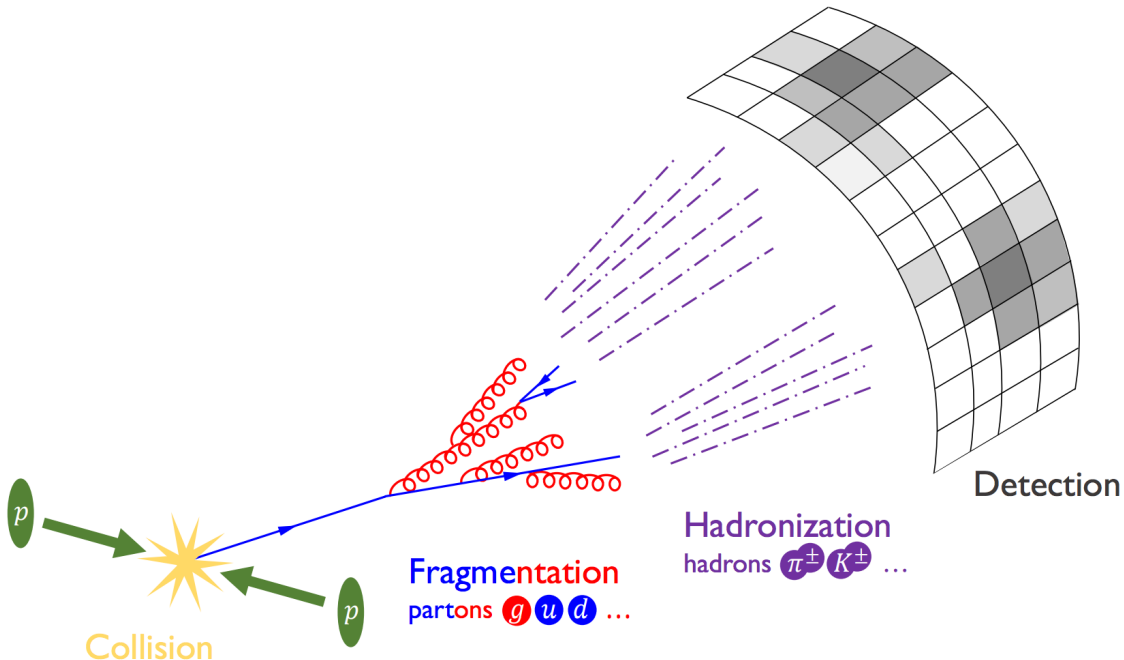


Figure 4.10 illustration of jets produced by pp collision and hadronised before seen by the detector.

521 Jets from the MC simulation are defined as truth-particle jets which have lifetimes

longer than 10 ps as stable particles. Truth-particles indicate the ideal measurement from a detector under perfect-condition and high resolution without defects or the effects from pile-up (background interactions per bunch-crossing in the LHC). Whereas track jets are constructed with the use of charged information in the ID, and calorimeter jets with the use of energy information in the calorimeters.

There are several types of jets aim for different analysis depended on the constituents and algorithm used for reconstructing the jets. ATLAS previously used topo-cluster jets, which is a group of topological related cells in calorimeter with significantly high energy deposits. A pile-up suppressed algorithm is applied to select certain cells with low noise. Cell above certain signal-to-noise (S/N) threshold (usually by four times its standard deviation) are used to seed the algorithm. By neighbouring the seed a topo-cluster is defined. In the hard-scatter process, jets of interest are expected to produced from the primary interaction point (known as vertex). The primary vertex is defined if there are at least two tracks with the highest sum of squared track momentum associated to it.

Jets are constructed from any set of four-vectors. EMTopo jets are the jets that use topo-cluster initially calibrated to electromagnetic (EM) scale in the calorimeters. A local cluster weighting (LCW) scale is also used for calibrating hadronic clusters by applying weights for low hadronic interaction response. Besides, particle flow (PFlow) jets are built by combining the information from both the ID and the calorimeter, where the energy deposited from the calorimeter are removed by the momentum in the ID by a cell-based energy subtraction algorithm. The inputs to the particle flow algorithm are the separate topo-clusters with local energy maxima, respectively.

A recombination algorithm called anti- k_t algorithm is employed to build the jets with a radius parameter R in rapidity-azimuth ($y - \phi$) plane around a cluster. The algorithms are defined as follows:

$$d_{ij} = \min \left(k_{ti}^{2p}, k_{tj}^{2p} \right) \frac{\Delta_{ij}^2}{R^2} \quad (4.1)$$

$$\Delta_{ij}^2 = (y_i - y_j)^2 + (\phi_i - \phi_j)^2 \quad (4.2)$$

$$d_{iB} = k_{ti}^{2p} \quad (4.3)$$

where the distance d_{ij} between any pair of particles i and j is given by the minimum transverse momenta k_t of the two particles. The geometrical distance Δ_{ij} represents the separation of a pair of particles in $(y - \phi)$ plane. Radius parameter R indicates the size of the final jets. The distance d_{iB} between any detected particle i and the beam B is also given. Parameter p indicates the relative power of energy with respect to geometrical scales and is used to distinguish the different types of algorithms.

When p is set to 0, the Cambridge-Aachen (CA) algorithm is given as the distance d_{ij} and d_{iB} only based on spatial separation and are independent of the transverse momenta. This algorithm is usually used for large-radius jets and jet substructure performance study.

For the k_t algorithm, p is set to 1 so that the distance d_{ij} is dominated by the minimum k_t . This algorithm is preferred for clusters that are soft and collinear splits are merged first, resulted in irregular footprint with the most interesting splits.

The algorithm on the other hand set $p = -1$, leaving the distance $d_{ij} \propto \min\left(\frac{1}{k_{ti}^2}, \frac{1}{k_{tj}^2}\right)$ shorten as the transverse momenta of two particles increase. This is widely used in the LHC for hard clustering as it is less vulnerable to the effects from the pile-up and resulted in circular footprint as shown in Figure 4.11 for $R = 1.0$.

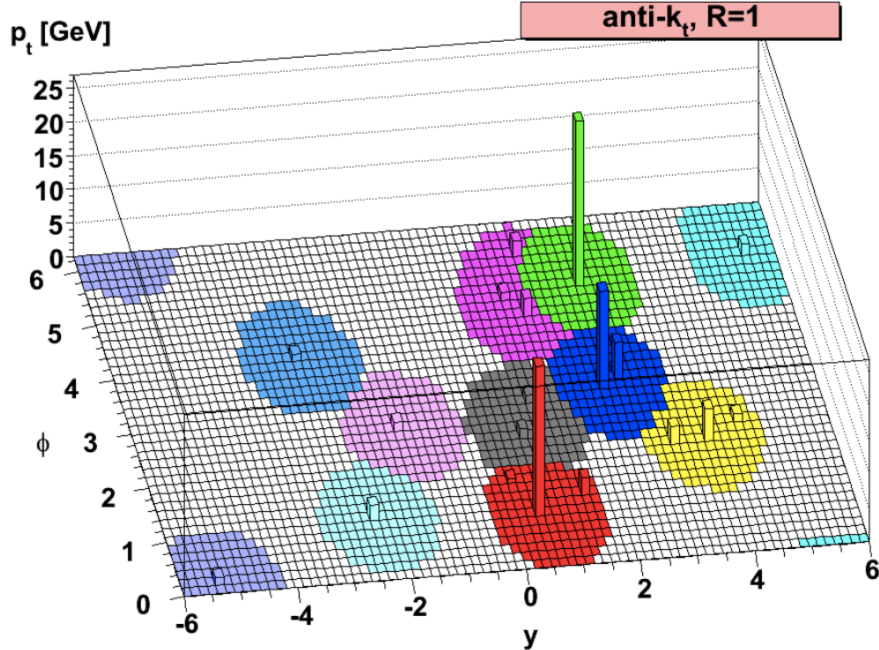


Figure 4.11 Plot of parton-level jets clustered using algorithms with radius parameter set to 1.

For most of ATLAS analysis, jets with $R = 0.4$ are used for quarks and gluons

566 analysis. Other ones such as $R = 1.0$ are also widely used to study energetic particles
 567 like W and Z bosons. $R = 0.2, 0.6, 1.2, 1.5$ and variable radii are also analysed.

568 The $R = 0.4$ PLow jets are used in the quark/gluon taggers calibration described in
 569 this thesis.

570 4.2 Jet calibration and cleaning

571 The motivation of jet calibration is to correct the translation from received signals to
 572 initial partons for several detector effects, including energy deposited in dead or beyond
 573 areas in the detectors, low response to hadronic reactions, pile-up, radiations that outside
 574 jet cone, etc. The calibration process is thus needed to account for the energy of jets to
 575 that of MC simulated jets at particle-level.

576 Calibration is performed to topological clusters at the EM scale where the sum of
 577 the energies in all constituent cell are taken, or at the LCW scale where low hadronic
 578 response in the ATLAS calorimeters is taken into account. The diagrams 4.12 shows the
 579 calibration scheme for small- R jets.

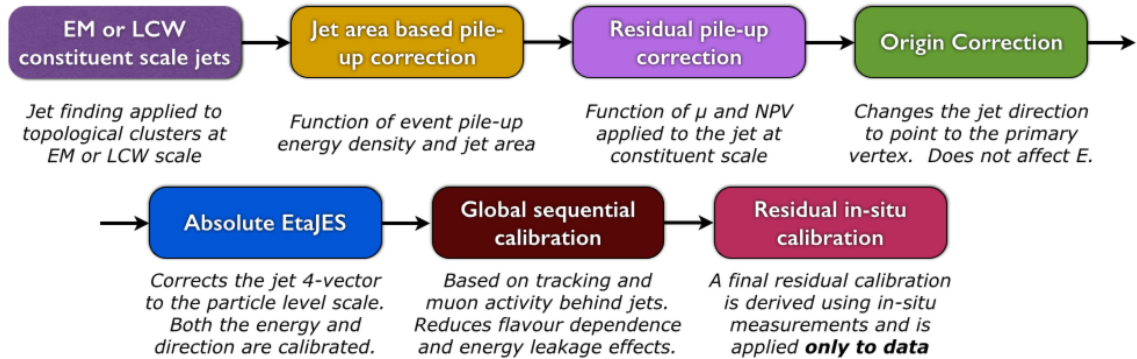


Figure 4.12 Overview scheme of jet calibration in the ATLAS.

580 4.2.1 Pile-up corrections

581 In order to eliminate a great amount of energy deposits from pile-up, a jet area-based subtraction of pile-up contribution to the p_T of each jet per event is applied as the
 582 start of the calibration chain.
 583

584 After all pile-up corrections are applied, the jet p_T is given by:

$$p_T^{\text{corr}} = p_T^{\text{reco}} - \rho \times A - \alpha \times (N_{\text{PV}} - 1) - \beta \times \mu \quad (4.4)$$

where p_T^{reco} indicates the reconstructed jet p_T before any pile-up correction is applied. The jet area A is defined by certain number of ghost tracks associated with a jet after clustering thus can quantify the liability of a jet to pile-up. The pile-up p_T density ρ is used to evaluate the contribution from pile-up in the y - ϕ plane. To calculate the density ρ of each jet in the distribution p_T/A , a k_t algorithm with radius $R = 0.4$ is employed to reconstruct jet from positive-energy topo-clusters within the range of $|\eta| < 2$. The calculation of ρ performed in such η range for pile-up measurement is due to the fact that ρ tend to be zero beyond $|\eta| \approx 2$ as a result of lower occupancy in coarser segmentation in the forward region. Therefore, pile-up sensitivity in the forward region is not fully described after such correction.

An additional residual correction is thus applied from the MC simulation to account for the difference between the reconstructed jet p_T and truth jet p_T as a function of the number of reconstructed primary vertices in the event N_{PV} and the mean number of interactions per bunch crossing μ , which are sensitive to in-time and out-of-time pile-up, separately.

Both the initial values of α and β coefficients are derived in bins of truth jet p_T and geometric centre of the detector $|\eta_{\text{det}}|$. A logarithmic dependence on truth jet p_T is observed.

4.2.2 Jet energy scale and η calibration

Following the pile-up mitigation, the absolute jet energy scale and η calibration are introduced to correct the four-momentum of the reconstructed jet to the truth-particle jets, accounting for defecting calorimeter response, energy losses when particles passed through certain materials, boundary effects and biases in the reconstructed jet in different η due to the transition between the granularities and technologies changes in calorimeter.

Since the detector responses differ across the detector η range, the reconstructed jets are thus divided into small bins of η_{det} and the energy of the truth jet E^{truth} as the response distribution for fixed E^{truth} is Gaussian. The average jet energy response \mathcal{R} is defined as $E^{\text{reco}}/E^{\text{true}}$ using the mean of a Gaussian fit in η_{det} and E^{truth} bins, and is further parameterized as a function of E^{reco} . Such response for PFlow jets is higher than that for EMtopo jet at low energies as the tracking information is considered.

Besides Jet energy scale (JES) correction, the bias from the η of the reconstructed jet to that of the truth jet is taken into account. The bias is defined as a significant devi-

617 ation from zero in the signed difference between the reconstructed jet η^{reco} and truth jet
 618 η^{truth} , separately. Then a second correction is applied as such difference is parameterized
 619 as a function of η_{det} and E^{truth} .

620 The calibration is derived as a function of energy and η from the MC samples which
 621 do not have the effects from pile-up, and only correct the jet p_T and η instead of full four-
 622 momentum. The EMtopo and PFlow jets after full JES and η calibration are regarded as
 623 EM+JES scale and PFlow+JES scale, respectively. Small non-closures beyond $|\eta_{det}| \approx$
 624 3.2 in the calibration are seen due to approximate treatment of hadronic showers in the
 625 forward region, lead to an additional systematic uncertainty.

626 4.2.3 Global sequential calibration

627 The global sequential calibration (GSC), based the global jet observables such as
 628 the fraction of jet energy measured in the different layer of hadronic and the EM
 629 calorimeters, the tracking information associated with the jets, and the number of muon
 630 track segment. For each observable, a series of multiplicative corrections are applied on
 631 the four-momentum as a function of p_T^{truth} and $|\eta_{det}|$. Considered any observable x , the
 632 correction is derived from the inverted jet response \mathcal{R} :

$$C(x) = \frac{\mathcal{R}^{-1}}{\langle \mathcal{R}^{-1}(x) \rangle} \quad (4.5)$$

633 where $\langle \mathcal{R} \rangle$ is the average jet response.

634 As a result, the fluctuations in the jet particle composition are reduced and the jet
 635 resolution can be improved without changing the average jet energy response which
 636 depends on the flavour and the energy distribution of the constituent particles. The shape
 637 of a jet varies between quark- and gluon-initiated jets as hadrons are often included in a
 638 quark-initiated jet with higher fraction of the jet p_T with higher calorimeter response.

639 After applied GSC for PFlow jet, the average jet p_T response on each observable is
 640 reduced to lower than 2% with small deviations from correlations between observables.

641 The fractional jet resolution $\sigma_{\mathcal{R}}/\mathcal{R}$ is derived from the jet resolution $\sigma_{\mathcal{R}}$, which is
 642 defined by the standard deviation of a Gaussian fit to the distributionof jet p_T response.
 643 This fractional jet resolution is used to determine the size of the fluctuations in the jet
 644 energy reconstruction.

645 **4.2.4 Residual *in situ* calibration**

646 The final step of the jet calibration is performed only in data to account for the
647 differences of jet response measurement in data and the MC, the derived ratio of it is
648 used as a correction in data. The differences are introduced by the inadequate nature of
649 the detector materials and the imperfect simulation of the real physics processes. Such
650 differences can be quantified by weighting the p_T of a jet to other reference objects that
651 well-measured. The correction factor can be denoted as follows:

$$c = \frac{\mathcal{R}_{\text{in situ}}^{\text{data}}}{\mathcal{R}_{\text{in situ}}^{\text{MC}}} \quad (4.6)$$

652 the response $\mathcal{R}_{\text{in situ}}$ represents the average ratio of the jet p_T to the reference object
653 p_T in bins of reference object p_T , where the average value is founded from peak value
654 of a Gaussian fit to the distribution. The double ratio is robust to secondary effects thus
655 more reliable in term of the measurement of jet energy.

656 Three stages are carried out in such *in situ* calibration. First, η -intercalibration is
657 performed on the energy scale of forward jets ($0.8 \leq |\eta_{\text{det}}| < 4.5$) to match the central jets
658 ($|\eta_{\text{det}}| < 0.8$) using the jet p_T in dijet events. Then $Z+\text{jet}$ and $\gamma+\text{jet}$ analyses balance the
659 measurement of p_T response of a well-calibrated Z boson or photon. Finally, a multijet
660 balance (MJB) analysis is employed to calibrate low- p_T jets to a very high- p_T jet. Both
661 MJB and $Z/\gamma+\text{jet}$ analyses are used only for jets in the central region ($|\eta| < 1.2$). All
662 three *in situ* calibrations are done sequentially so that the systematic uncertainties can be
663 propagated from each to the next. The systematic uncertainties in each calibration pro-
664 cess come from three sources: the MC modelling of physics processes, the uncertainties
665 in the measurement and from topology obtained by different event selections.

666 5 The calibration of quark/gluon jets taggers

667 The classification of jets originated from a quark or a gluon is useful for improving the
668 SM measurements and searches for BSM physics at the LHC. According to the QCD,
669 gluons are in the adjoint representation of the $SU(3)$ gauge group thus carry both colour
670 and anti-colour quantum numbers, whereas quarks are in the fundamental representation
671 and have only a single colour number. As a result, a gluon-initiated jet (gluon-jet) tend to
672 have more constituents and a broader radiation pattern than a quark-initiated jet (quark-
673 jets).

674 The manifestation of colour charges is intrinsic to quarks and gluons; however,
675 the confinement phenomenon inherent in QCD theory indicates that only colour neutral
676 hadrons can be observed in the detector. Such principle brings significant challenges
677 for the identification of quark- or gluon-jets in ATLAS. The identification method relies
678 on the number of charged tracks within the jets and the reconstruction algorithm for
679 it. The calibration described in this paper demonstrates the measurement of the tagging
680 efficiencies of the aforementioned jet taggers. The more advanced boosted decision tree
681 (BDT) algorithm is employed to constructed the jet tagging variable based on the charge
682 multiplicity inside jets. A matrix method is established with the use of quark/gluon
683 fraction in quark-/gluon-enriched subsamples, defined by the pseudorapidity of jets. The
684 scale factors extracted from the difference between data and simulation are provided
685 for tagger working points corresponding to 50%, 60%, 70% and 80% fixed quark-jet
686 efficiencies for both quark- and gluon-jets, respectively.

687 5.1 Data and Monte Carlo samples

688 5.1.1 Data

689 The data recorded in 2015-2018 with integrated luminosity of 140 fb^{-1} (full Run
690 2 data) is used in this study. The data samples are processed through the un-skimmed
691 DAOD_JETM1 derivation scheme in order to obtain multi-jet events. The lowest un-
692 prescaled small- R single-jet trigger is employed for this analysis. The jet p_T threshold
693 for the trigger in this analysis is 420 GeV, keeping the selection consistent across years,
694 together with additional requirements that ensure events of good qualities are used. The
695 additional selections are:

- 696 • Good Run List (GRL): Make sure a steady state of all relevant detectors so that
697 physics processes recorded by them are good.
- 698 • LAr: Liquid Argon Calorimeter error rejected.
- 699 • Tile: Tile Calorimeter error rejected.
- 700 • SCT: SCT single event upsets rejected.
- 701 • Core: Incomplete event build rejected.
- 702 • Primary Vertex: the highest $\sum p_T^2(trk)$ vertex has at least two tracks associated with
703 it
- 704 • Trigger: Passes the lowest unprescaled single-jet trigger, HLT_j420

705 Additional kinematic selection criteria are discussed in Section 5.2.

706 5.1.2 Monte Carlo simulation

707 For this calibration, multi-jet events are generated and modelled with several MC
708 simulations, processed through the same DAOD_JETM1 derivation scheme. For the
709 nominal result, PYTHIA 8.230 MC generator is used with leading-order (LO) matrix el-
710 ement (ME) for dijet production. Parton density functions (PDFs) are considered for
711 systematic uncertainties evaluation as the PDF set is used for PYTHIA 8.230. Alter-
712 native samples with different choices of parton shower modelling, ME generation, and
713 the simulation of the multi-parton interactions are included to estimate the systematic
714 uncertainties.

715 Two set of MC samples generated using SHERPA 2.2.5 are used with the same ME
716 for the (2→2) process at LO, to provide the uncertainties of hadronization modeling. The
717 CT10 PDF sets are included in both SHERPA samples where one based on the cluster
718 hadronization whereas the other used SHERPA interface to the Lund string fragmentation
719 model as PYTHIA 8.230.

720 Two set of MC samples generated using HERWIG 7.1.3 are used for parton shower
721 uncertainties as one uses angular ordering shower whereas the other one uses dipole
722 shower. These samples are produced at next-to-leading order (NLO) with a PDF set of
723 MMHT .

724 Another set of multijet samples that produced with POWHEG interfaced to PYTHIA at
 725 NLO accuracy is employed with NNPDF2.3 LO PDF set, to estimate the effects from
 726 the ME uncertainty as different perturbative scales in the ME and parton distribution
 727 functions are included. The renormalization and factorisation scales are set to the p_T of
 728 the underlying Born configuration. These samples included different perturbative scales
 729 in the ME and parton distribution functions are used for the estimation of ME uncertainty.

730 A list of the MC samples used is given in table 5.1.

PDF set	Generator	Cross-section	Parton shower	Hadronisation
NNPDF2.3	PYTHIA 8.230	LO	p_T -ordered	String
CT10	SHERPA 2.2.5	LO	p_T -ordered	Cluste
CT10	SHERPA 2.2.5	LO	p_T -ordered	String
MMHT	HERWIG 7.1.3	NLO	Dipole	Cluster
MMHT	HERWIG 7.1.3	NLO	Angular-ordered	Cluster
NNPDF2.3	Powheg+PYTHIA	NLO	p_T -ordered	String

Table 5.1 The MC simulation used for the multi-jet processes in this calibration. The PDF sets, generators for a hard process, the order in α_s of cross-section calculations and the simulator of parton showers, and hadronisation are shown.

731 5.2 Object and Event selection

732 In order to perform the calibration of the quark-/gluon-jet tagger, it is requisite to
 733 establish two distinct subsamples. One subsample should be predominantly composed of
 734 quark-jets, called quark-enriched sample, while the other should predominantly consist
 735 of gluon-jets, as gluon-enriched sample. These subsamples are gained from the dijet
 736 events. This section describes the reconstruction and selection of jet objects used in this
 737 calibration, as well as the approach to construct quark- and gluon-enriched subsamples.

738 5.2.1 Physics object definition

739 The PFlow jets that are reconstructed with the algorithm with a radius parameter
 740 R set to 0.4. An overall jet energy calibration described in section 4.2 has been done
 741 to rectify residual detector effects and pile-up. In order to ensure a good quality jet, an
 742 event-based jet cleaning with standard loose cut is applied to reject events with flawed
 743 leading or subleading jet.

744 Tracks that reconstructed from the ID are required to have $p_T > 500$ MeV, and
 745 within the ID range $|\eta| < 2.5$. Additional criteria such as primary vertex are required to
 746 ensure selected tracks originating from the collision and prevent the mis-reconstructed
 747 tracks from pile-up hits in the detector. The alignment of tracks with calorimeter-based
 748 jets is executed through the application of the ghost-association technique. This entails
 749 a repetition of the jet clustering procedure augmented by the inclusion of 'ghost' rep-
 750 resentations of registered tracks. These ghost tracks share the same direction as their
 751 actual counterparts but possess an infinitesimally small p_T , thereby ensuring that they do
 752 not induce any alterations to the intrinsic characteristics of the calorimeter-based jets. A
 753 criterion for track-jet correspondence is established: a given track is associated to a jet if
 754 its corresponding ghost track is contained in the jet after reclustering.

755 Jet reconstructed from the simulated MC is known as "truth jets", with the same
 756 $R = 0.4$ algorithm as PFlow jets. Geometric correspondence between truth jets and
 757 PFlow jets is established via angular proximity, adhering to the criterion $\Delta R < 0.4$. Each
 758 truth jet is bestowed with a flavour label, referred to as a truth label. The truth flavour
 759 label attributed to a jet is defined by the flavour of the highest-energy parton situated
 760 within a cone of size $\Delta R < 0.4$ around the jet's axis, prior to the process of hadronisation
 761 in the parton shower. Following this definition, jets arising from the splintering of glu-
 762 ons into b - or c -quark pairs are labelled as heavy flavour jets. These heavy flavour jets
 763 are often identifiable by the long-lived or leptonically decaying hadrons. Therefore, no
 764 distinct discriminant tailored for heavy-flavour quarks is investigated within the current
 765 framework. Jets will be unlabelled if there is no corresponding truth parton with $p_T > 1$
 766 GeV is found within the cone surrounding the truth jet. These instances of unlabelled jets
 767 commonly emerge as a consequence of pile-up effects, and less than 1% of the dataset
 768 used. They are thus ignored.

769 5.2.2 Event Selection and definition of quark and gluon-enriched samples

770 Events are chosen by the single-jet trigger, HLT_j420. The jet p_T is required to be
 771 greater than 500 GeV, as more quark-jets and better resolution on the jet constituents
 772 are given. Only the leading two jets with the highest p_T are used, as dijet events, and
 773 are required to be $|\eta| < 2.5$ so that their charged constituents are collected within the
 774 coverage of the ID. To maintain the equilibrium in p_T and suppress non-isolated jets, a
 775 criterion demands that the ratio of the p_T of the leading jet to that of the sub-leading jet

The calibration of quark/gluon jets taggers

remains within 1.5. The two leading p_T jets serve as the cornerstone for the formulation of quark-enriched and gluon-enriched subsamples.

The quark-enriched sample is derived from the jet with higher $|\eta|$ among the leading two jets, while the gluon-enriched sample is extracted from the jet with lower $|\eta|$. This selection strategy capitalizes on the intrinsic behaviour of PDFs at higher proton momentum fraction range, where there exists a higher likelihood of encompassing valence quark-jets. Consequently, jets situated in more forward regions (higher $|\eta|$) have a higher probability of being quark-jets, while jets positioned closer to the central region (lower $|\eta|$) manifest an increased likelihood of corresponding to gluon-jets.

Selection	Multi-jet sample
Trigger	HLT_j420
Number of jets	≥ 2
$p_T(j_1)$	> 500
$p_T(j_2)$	> 500
$p_T(j_1)/p_T(j_2)$	< 1.5
$ \eta(j_1) $	< 2.1
$ \eta(j_2) $	< 2.1
Target parton	Quark(Higher $ \eta $) or Gluon (Lower $ \eta $)

Table 5.2 The selections to retrieve quark/gluon-enriched samples. " j_i " represents the i -th jet in p_T -ordering.

The distribution of leading and subleading jets p_T in dijet event after selections is shown in Fig. 5.13 for both MC and data.

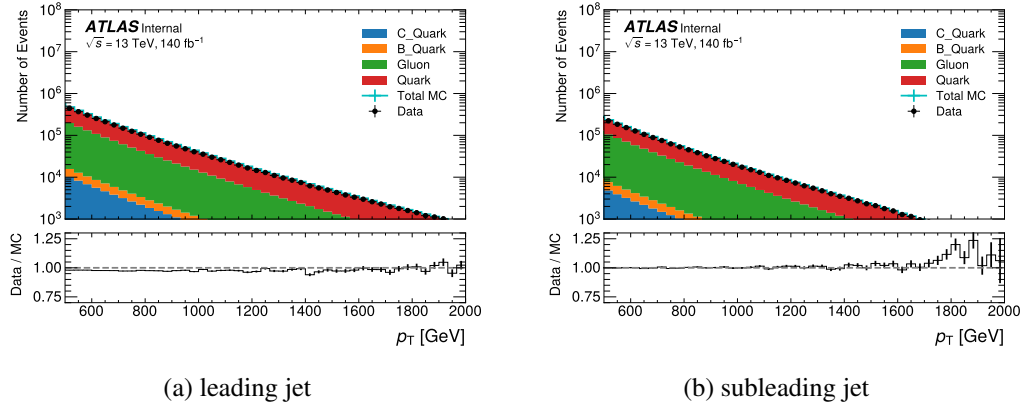


Figure 5.13 The p_T distribution of the leading jets and sub-leading jets with PYTHIA samples for dijet event.

787 **5.3 Quark/gluon tagging variables**

788 According to QCD, the colour factor of gluons is larger than that of quarks by factor
 789 9/4 ("Casimir ratio"), which makes gluons emit more particles in the hadronisation than
 790 quarks. As a result, a gluon-initiated jet has more charged multiplicity associated and its
 791 width is larger than that of a quark-initiated jet. Therefore, the information of the track
 792 multiplicity inside a jet is crucial to distinguish quarks from gluons.

793 The q/g tagging variables used in this study are based on the track multiplicity
 794 and are specified as : number of tracks (N_{trk}), jet width (W_{trk}), and two point energy
 795 correlation function ($C_1^{\beta=0.2}$) computed from the associated tracks. The expressions are
 796 defined as follows:

797 N_{trk}

798 N_{trk} is a number of tracks associated with the jet.

$$N_{\text{trk}} = \sum_{\text{trk} \in \text{jet}} \quad (5.1)$$

799 W_{trk}

800 W_{trk} is a track- p_{T} -weighted width of the jet divided by the scalar sum of track
 801 transverse momenta. It is defined as

$$W_{\text{trk}} = \frac{\sum_{\text{trk} \in \text{jet}} p_{\text{T},\text{trk}} \Delta R_{\text{trk,jet}}}{\sum_{\text{trk} \in \text{jet}} p_{\text{T},\text{trk}}}, \quad (5.2)$$

802 where $p_{\text{T},\text{trk}}$ is a p_{T} of a charged track reconstructed by the ID and $\Delta R_{\text{trk,jet}}$ is a
 803 distance in the $\eta - \phi$ plane between the track and the jet axis.

804 $C_1^{\beta=0.2}$

805 Two point energy correlation function is defined as

$$C_1^{\beta=0.2} = \frac{\sum_{i,j \in \text{jet}}^{i \neq j} p_{\text{T},i} p_{\text{T},j} (\Delta R_{i,j})^{\beta=0.2}}{\left(\sum_{\text{trk} \in \text{jet}} p_{\text{T},\text{trk}} \right)^2}, \quad (5.3)$$

806 where i and j denote tracks associated with the jet and the sum runs over all the
 807 combination of two tracks. The β is fixed to 0.2, which is known to be suitable for
 808 q/g tagging.

5.3.1 The BDT tagger

Multivariate Analysis (MVA) is a technique introduced to discriminate signal from background, one type of classification algorithm in MVA is the BDT. A tree structure is built to classify datasets through a sequence of branching binary decisions. Data with desirable features is kept by discriminating algorithm whereas others are rejected. Each decision point made construct a node at each level of the decision tree, and a score is assigned to every classifier that goes into the boosting process based on its error rate. One decision node can have two or more branches to split the datasets. Such procedure is iterated from top to down so that a termination condition such as the minimum number of samples in a node or a maximum depth in a tree depth is met. A diagram of a single decision tree is shown in Figure 5.14. After all series of cuts are applied, the BDT is defined. Therefore, a cut based on the BDT score can be employed as the most correct classification of datasets.

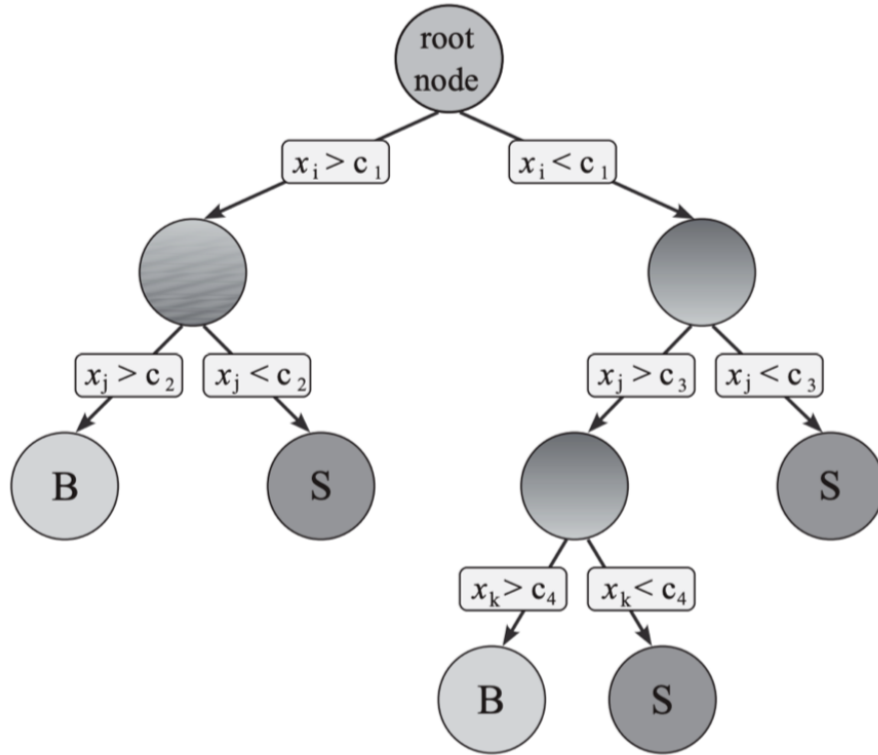


Figure 5.14 A scheme of a single decision tree with a depth of three

The BDT tagger is constructed by the combination of tracking-related observables: N_{trk} , W_{trk} , $C_1^{\beta=0.2}$ and p_T of a jet are included as the distribution of the track multiplicity

is affected by them. In this study, the BDT score is used to classify quark- or gluon-jets from the multi jet samples, with the truth-labelled information from MC to train until a quark signal efficiency larger than 90% is reached.

The BDT tagger is trained using the LGBMClassifier from lightGBM [?] framework, and hyper-parameter tuning is performed with Optuna [?]. The MC PYTHIA samples are employed.

An individual score is allocated to each BDT within the boosting procedure, factoring in its error rate. This BDT score serves as the criterion for classifying a given jet as either a quark-jet or a gluon-jet.

5.3.1.1 Feature selections

Drawing upon the features employed during the training process, an exploration of the correlation matrix is undertaken to assess the interdependence among jet attributes, including p_T , $|\eta|$, and jet substructure variables N_{trk} , W_{trk} , $C_1^{\beta=0.2}$, and the BDT. Figure 5.15 shows N_{trk} , W_{trk} and $C_1^{\beta=0.2}$ exhibit notable interrelationships among themselves, displaying relatively robust correlations. In contrast, p_T and η display a diminished level of correlation. The distributions of all single jet substructure variables and BDT score with systematic uncertainty in forward and central regions are shown in Figure 5.16. The distributions of all single jet substructure variables and BDT score with systematic uncertainty of quark- and gluon-jets in different p_T ranges from the MC simulation are shown in Figure 5.17.

Rather than employing multiple BDTs for different p_T ranges, an universal BDT can be trained using events in all p_T ranges. Given the intrinsic correlation between N_{trk} and the jet p_T , a natural way to choose features is including p_T in addition to three q/g tagging variables. Concerning the remaining variable, η , two comparative scenarios are juxtaposed: one involves its inclusion, and the other pertains to its exclusion. This comparison facilitates an assessment of whether or not to incorporate $|\eta|$.

1. p_T , N_{trk} , W_{trk} and $C_1^{\beta=0.2}$
2. p_T , $|\eta|$, N_{trk} , W_{trk} and $C_1^{\beta=0.2}$

The result depicted in Figure 5.18 shows a distinct discrepancy when $|\eta|$ is encompassed within the training. This violates the assumptions that the partons distribution in more forward and more central regions should not change. Specifically, the distribution

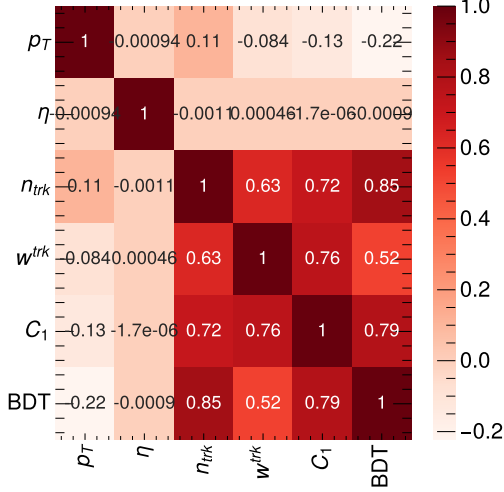


Figure 5.15 correlation matrix of jet variables.

of BDT scores for forward quarks substantially diverges from that of central quarks, a trend that is similarly observed for gluons. Moreover, adopting the BDT tagger that incorporates $|\eta|$ would result in inadequate performance for jets situated within the central region when this tagger is applied to a pure sample of quark-jets (e.g., $Z+jet$ samples). In the present analysis, the BDT is endowed with the spectra of p_T , N_{trk} , W_{trk} , and $C_1^{\beta=0.2}$, as exemplified in scenario 1. At detector-level, however, the observed radiation pattern within jets no longer remains unaffected by $|\eta|$, owing to variances in the detector material and technology. To counteract this effect, a subsequent re-weighting procedure is implemented, described in Section 5.5.

5.3.1.2 Training weights

An additional data processing step is conducted to modify the event weights, such that a flat distribution of the p_T spectrum is given. This adjustment is motivated by the observation that higher p_T jets have less probability to occur, so the training on the higher p_T jets need to be emphasise. This newly introduced weight, referred to as the "flat p_T -weight" within this context, is exclusively employed during the training process. Conversely, for other scenarios, such as assessing tagger performance on validation datasets and subsequent calibration endeavours, the original event weights based on physical considerations remain employed.

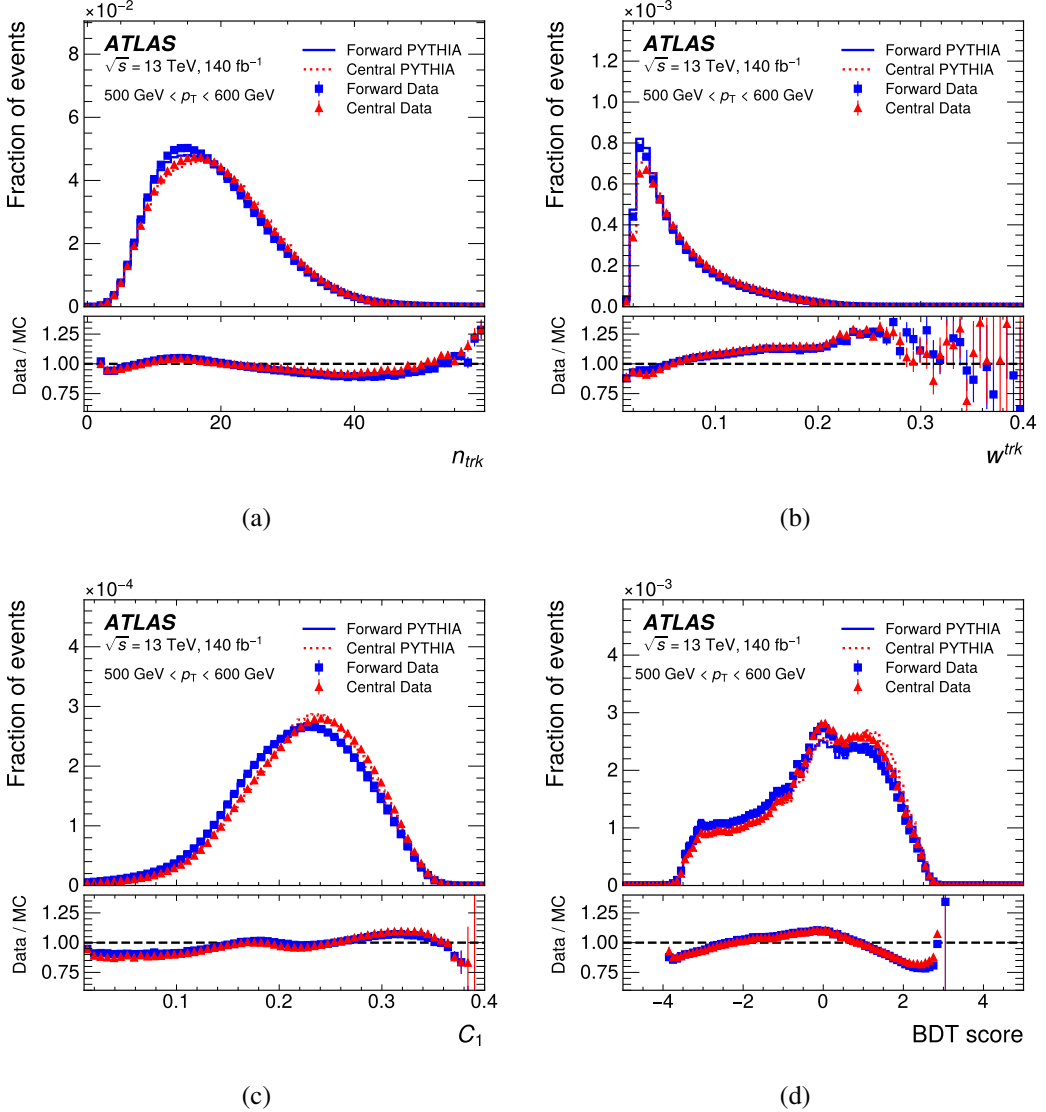


Figure 5.16 The distributions of N_{trk} (a), W_{trk} (b), C_1 (c) and BDT score (d) in the forward and central regions in data (closed symbols) and the PYTHIA MC (lines) are shown in the upper panels. The bottom panels show the ratio of the data and the MC. The distributions shown are for jet p_T in the range between 500 GeV and 600 GeV. The vertical error bars show the statistical uncertainty.

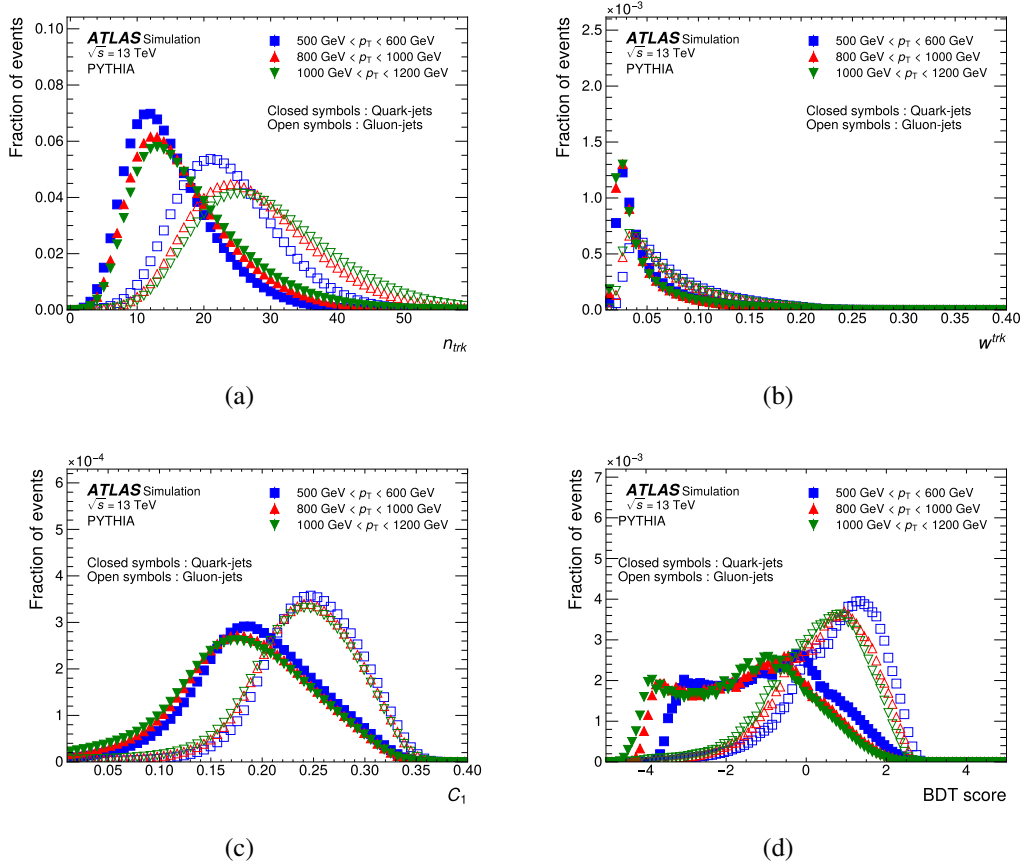


Figure 5.17 The distributions of N_{trk} (a), W_{trk} (b), C_1 (c) and BDT score (d) in the quark-jets (closed symbols) and gluon-jets (open symbols) in given p_T regions using the PYTHIA MC samples.

The calibration of quark/gluon jets taggers

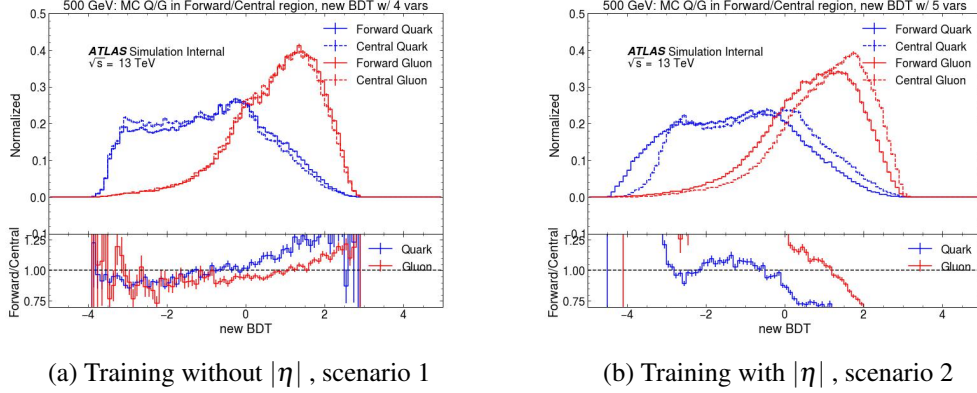


Figure 5.18 The comparison of BDT distribution for different scenarios in the jet p_T range from 500 to 600 GeV.

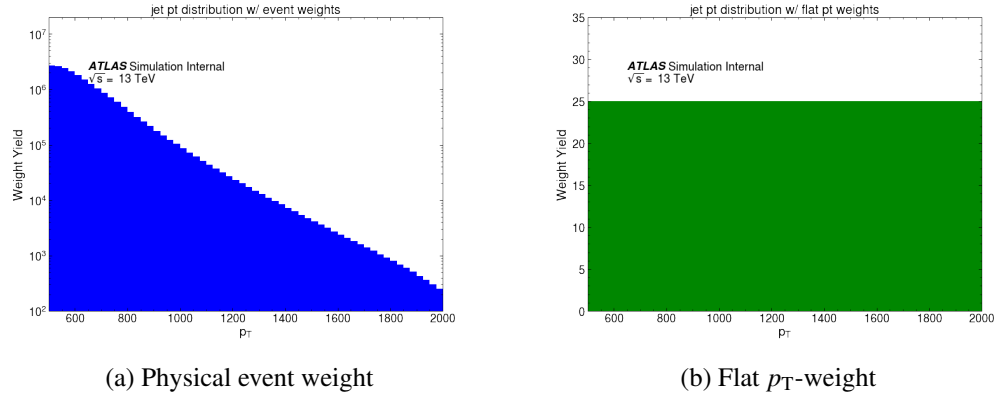


Figure 5.19 The comparison of jet p_T distributions with different weights.

5.3.1.3 Training Configuration

Approximately 30% of the data from each period of the MC PYTHIA 8 A, D, E is randomly allocated for the training investigation, constituting an aggregate of roughly 60 million jets. The dataset division for training, validation, and testing is structured in a ratio of 80% for training, 10% for validation, and 10% for testing.

Optuna is employed to conduct a search for optimal hyperparameters. Following the hyperparameter tuning process, the most optimal model is achieved after 100 iterations of such procedure. The optimised parameters are listed:

- bagging_fraction 0.9176347488279626
- bagging_freq 2

- 883 • feature_fraction 0.9084973008559477
- 884 • lambda_l1 0.0016400096502256838
- 885 • lambda_l0 0.006327330258011633
- 886 • min_child_samples 13
- 887 • num_leaves 224

888 The performance of a classification model at all classification criteria can be illus-
 889 trated using a receiver operating characteristic (ROC) curve. The idea is to compare
 890 the true positive rate (TPR, also known as sensitivity, recall or probability of detection)
 891 against the false positive rate (FPR, also known as the probability of false alarm) at dif-
 892 ferent criteria given. Consider a binary classification case, where the outputs are either
 893 labelled as positive (p) or negative (n), in total there are four possible outputs from a two-
 894 class prediction problem. A true positive (TP) is given if the output from a prediction is
 895 p and the actual value is also p, otherwise a false positive (FP) is assigned if the actual
 896 value is n. Conversely, a true negative (TN) is given if both the prediction outcome and
 897 the actual value are n, whereas a false negative (FN) is assigned if the actual value is p.
 898 TPR as a synonym for recall is defined as:

$$TPR = TP / (TP + FN) \quad (5.4)$$

899 while the FPR is defined as:

$$FPR = FP / (FP + TN) \quad (5.5)$$

900 In this analysis, the prediction true is defined by higher $|\eta|$ jet and prediction neg-
 901 ative is defined by lower $|\eta|$ jet. The actual truth value is given by the quark jet from
 902 the MC truth information, whereas the actual negative value is given by the gluon truth
 903 information. Thus the quark efficiency is the TPR and the gluon rejection is FPR. An
 904 Area Under the ROC Curve (AUC) is used to evaluate the performance of a classifier,
 905 the better performance is indicated by higher AUC values.

906 Several ROC plots are made to compare different features and the BDT in different
 907 p_T ranges. To check whether the BDT tagger is overtrained, the shape comparison is

908 shown in Figure 5.20, between training dataset and validation dataset. No overtraining
 909 is observed as the distribution of training dataset is very similar to that of testing dataset.

910 Figure 5.21 shows the ROC curve for all single jet variables and the BDT-tagger
 911 in given p_T ranges in forward and central regions. Figure 5.22 shows the AUC of both
 N_{trk} -only tagger and the BDT-tagger as a function of jet p_T .

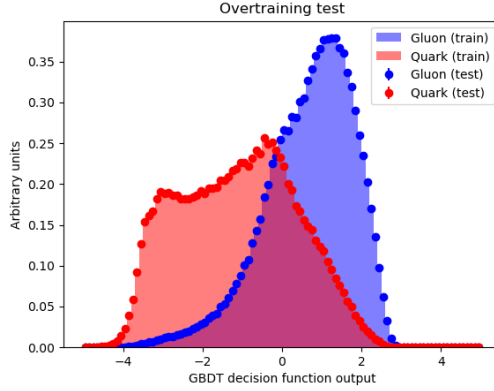


Figure 5.20 Overtraining validation

912

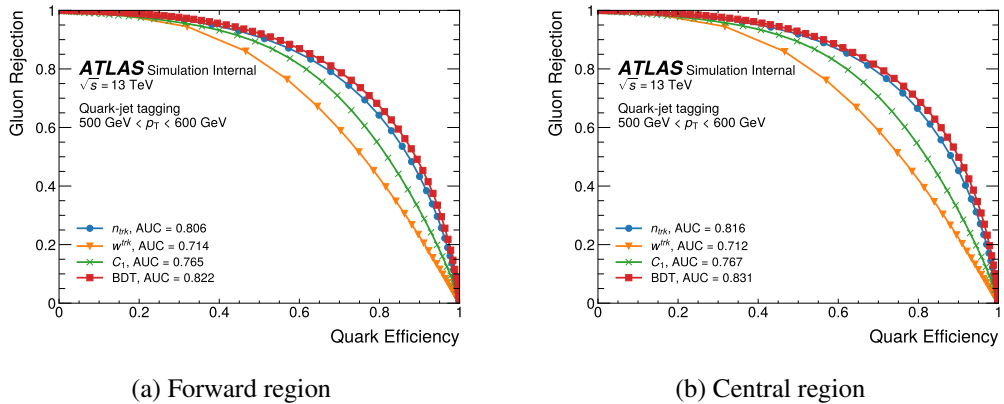
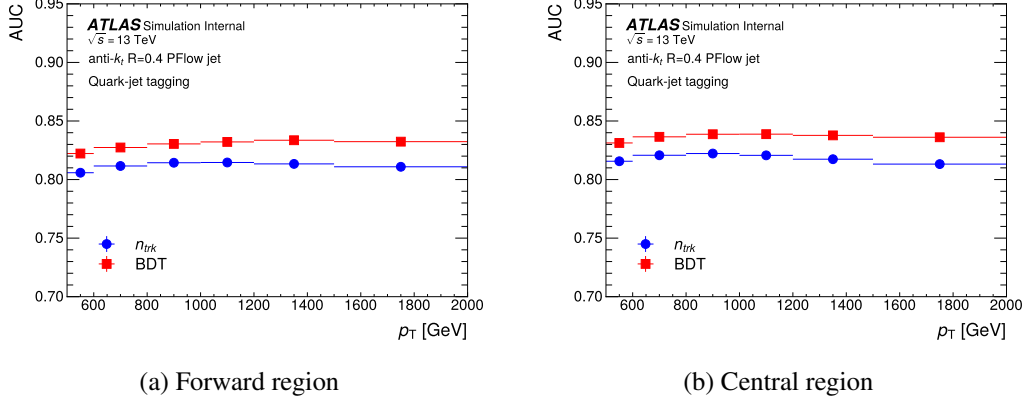


Figure 5.21 The ROC Curve for different taggers in the given jet p_T .

913 The N_{trk} -only tagger is found to be the most sensitive observable than other individual jet substructure variables for q/g tagging, W_{trk} and $C_1^{\beta=0.2}$ are less sensitive to the
 914 number of tracks inefficiencies because they are defined as ratios, the BDT-tagger which
 915 include the W_{trk} and $C_1^{\beta=0.2}$ has better AUC than N_{trk} -only tagger across all jet p_T ranges.
 916 This indicates that the BDT-based tagging mechanism has a heightened capacity to dis-
 917 criminate against gluon-jets at the same level of efficiency in identifying quark-jets with


 Figure 5.22 The AUC for different taggers across jet p_T .

919 N_{trk} -only tagger . Both taggers are calibrated in this paper, more details are presented in
 920 the next section.

921 5.4 Matrix Method

922 The distribution of q/g tagging variables depend strongly on jet p_T . Thus a matrix
 923 method approach used to extract the shape of the q/g tagging variables is performed on
 924 each p_T bin defined in Table 5.3 for quark- and gluon-jets, separately.

p _T bin boundary [GeV]					
500-600	600-800	800-1000	1000-1200	1200-1500	1500-2000
Forward & Central $ \eta $ jet samples in multi-jet					

Table 5.3 The p_T range division for the calibration of the q/g tagging variables and samples used in extraction of pure quark and gluon jets.

925 To measure the performance of the q/g taggers under study, samples exclusively
 926 composed of either quark-jets or gluon-jets are needed. In order to deduce the distribu-
 927 tion shapes of the q/g tagging variables pertaining to quark- and gluon-jets within the
 928 empirical data, a methodology that capitalizes on samples possessing varying q/g ratios
 929 is employed. This approach, known as the matrix method [?], facilitates the extraction of
 930 the distinct distributions of q/g tagging variables for the aforementioned jet categories.

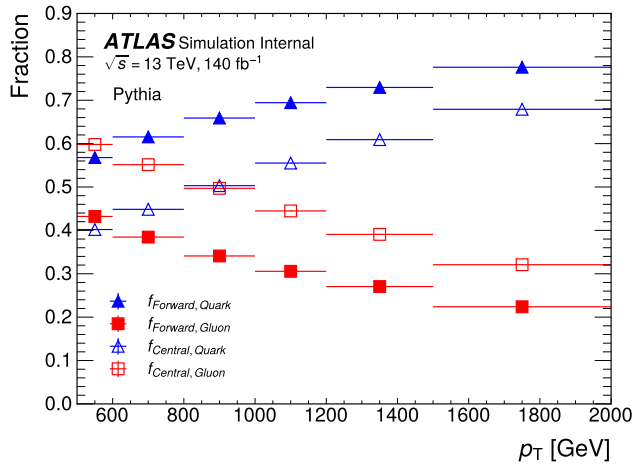
931 Pure quark- or gluon-jets can be extracted from forward and central jet samples

following the matrix:

$$\begin{pmatrix} p_F(x) \\ p_C(x) \end{pmatrix} = \underbrace{\begin{pmatrix} f_{F,Q} & f_{F,G} \\ f_{C,Q} & f_{C,G} \end{pmatrix}}_{\equiv F} \begin{pmatrix} p_Q(x) \\ p_G(x) \end{pmatrix} \quad (5.6)$$

$$\begin{pmatrix} p_Q(x) \\ p_G(x) \end{pmatrix} = F^{-1} \begin{pmatrix} p_F(x) \\ p_C(x) \end{pmatrix}. \quad (5.7)$$

where $p_{Q,G}(x)$ represents the distributions of the q/g tagging variable x in pure quark- and gluon-enriched jet samples, $p_F(x)$ and $p_C(x)$ show the distributions of jet variables in forward and central regions, respectively, $f_{F/C,Q/G}$ are the fractions of quarks and gluons in a forward or central region. The inverse matrix of F is thus constructed and used to extract pure quark/gluon $p_{Q,G}$. Data is used to obtain the distributions of the quark- and gluon-enriched samples, MC is used to calculate the fraction of quarks and gluons in them as shown in Figure 5.23, as well as the distributions of q/g tagging variables. The matrix is calculated in each x bin and each jet p_T range.



(a)

Figure 5.23 Fractions of quark-jets and gluon-jets in forward jet and central jet regions from PYTHIA dijet process. These values are used as elements in F matrix in Equation 5.6.

Figure 5.24 illustrates the fraction of light and heavy quark- and gluon-jets in the PYTHIA 8 dijet sample. These fractions are depicted in a stacked format, summing up to a cumulative value of 1. It should be noted that the involvement of heavy flavour quarks constitutes a minor fraction, amounting to a few percent, and is deemed negligible for the

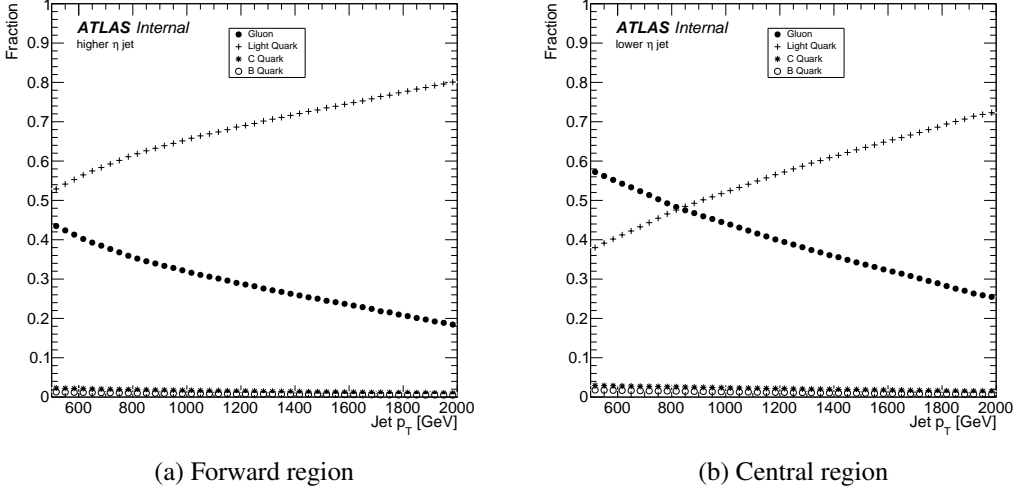


Figure 5.24 Flavor composition of forward (a) or central (b) multi-jet events.

945 later study. Previous investigations [?] have established that any discrepancies among the
 946 fractions derived from various MC event generators remain minimal. Furthermore, the
 947 shapes of distributions obtained from the MC simulations generally exhibit congruence
 948 with those observed within the data. The distributions of N_{trk} and BDT score in higher
 949 and lower jet regions are shown in Figure 5.25 and Figure 5.26 in jet p_{T} range 500 GeV
 950 - 600 GeV. The shapes of distributions obtained from the MC simulations is generally
 951 consistent with that from data.

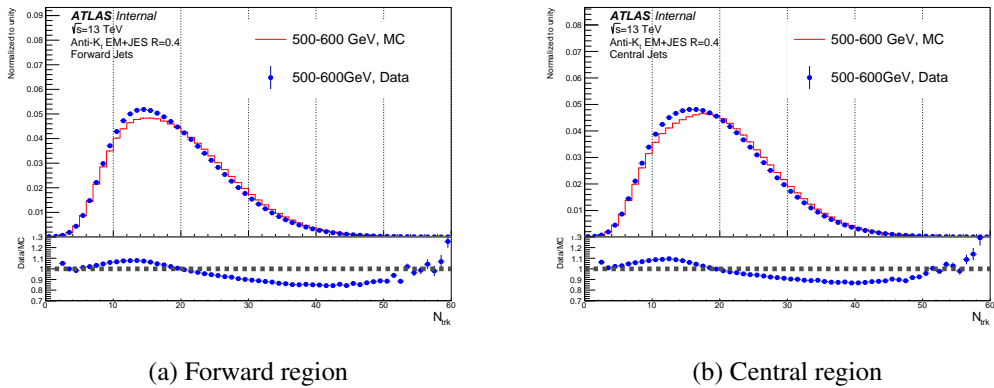


Figure 5.25 The N_{trk} distribution of the leading two jets with PYTHIA 8 in the MC and data.

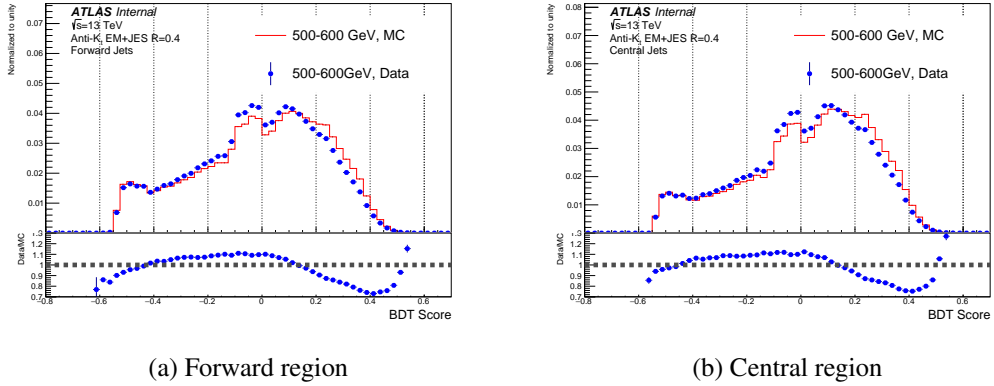


Figure 5.26 The BDT score distribution of the leading two jets with PYTHIA 8 in the MC and data.

5.5 MC non-closure

The matrix method is valid under the assumption that the shapes of $p_Q(x)$ and $p_G(x)$ remain consistent, regardless of whether the jets are situated in the central or forward regions. Jet fragmentation at a pp collider is expected to be predominantly influenced by the jet p_T and is generally considered independent of η , considering the underlying parton type. Consequently, an approach aimed at extracting distributions associated with the radiation patterns of quark-jets and gluon-jets should be valid at the particle level. At the detector level, however, the measured radiation pattern within jets no longer retains its η -independence. This is due to variations arising from differences in detector materials and technologies, leading to distinctions between the central and forward regions in terms of response. As a consequence of these effects, the matrix method experiences deviations from closure, indicating a disparity between the expected and actual outcomes.

The distributions of N_{trk} have been seen to have systematic difference for the truth-labelled quark/gluon jets in the quark-enriched and gluon-enriched regions in each p_T bin. To rectify this discrepancy and ensure alignment in the distribution of jet tagging variables between the central and forward regions, a re-weighting procedure is implemented. This procedure involves applying adjustments to account for the observed differences. For each event, the central jet is weighted by a re-weighting factor :

$$w_{Q/G}(x; p_{T,j}) = \frac{p_{Q/G, \text{forward}}(x; p_{T,j})}{p_{Q/G, \text{central}}(x; p_{T,j})} \quad (5.8)$$

970 where q/g tagging variable x is calculated in each jet p_T bin for quark and gluon jets,
 971 respectively. By default the re-weighting factor derived from truth-labelled quark-jets is
 972 implemented for both types of jets, whereas the re-weighting factor derived from truth-
 973 labelled gluon-jets is used as an alternative to evaluate the systematic uncertainty from
 974 the re-weighting procedure, known as MC non-closure systematic uncertainty for the
 975 calibration.

976 The distributions of N_{trk} in extracted pure quark- and gluon-jets and truth-labelled
 977 MC before re-weighting as shown in Figure 5.27. After the re-weighting the distributions
 978 of N_{trk} are shown in Figure 5.28. The non-closure is at few percent level and is taken
 979 as MC non-closure systematic uncertainty.

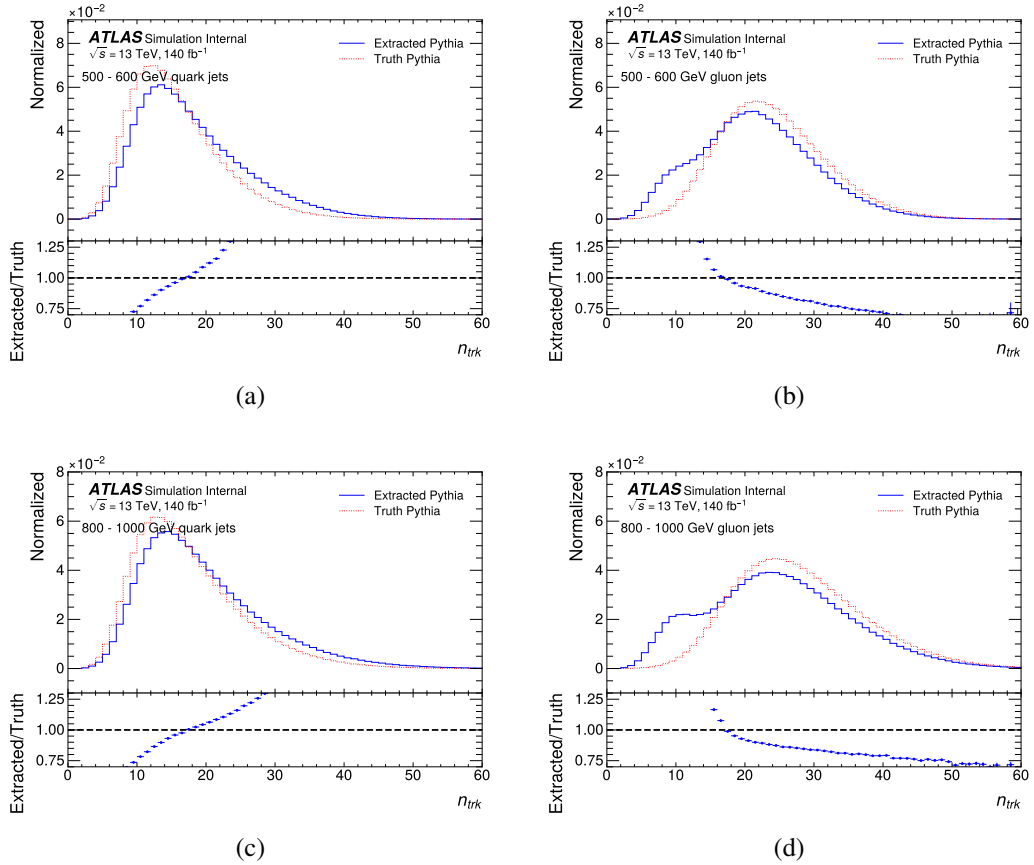


Figure 5.27 Before re-weighting: the N_{trk} distributions of quark-jet (a) (c) and gluon-jet in (b) (d) from PYTHIA 8 sample. Dashed and solid-line show the N_{trk} distributions in the truth MC and extracted MC, respectively. Bottom panels show the ratio of the extracted MC to the truth MC.

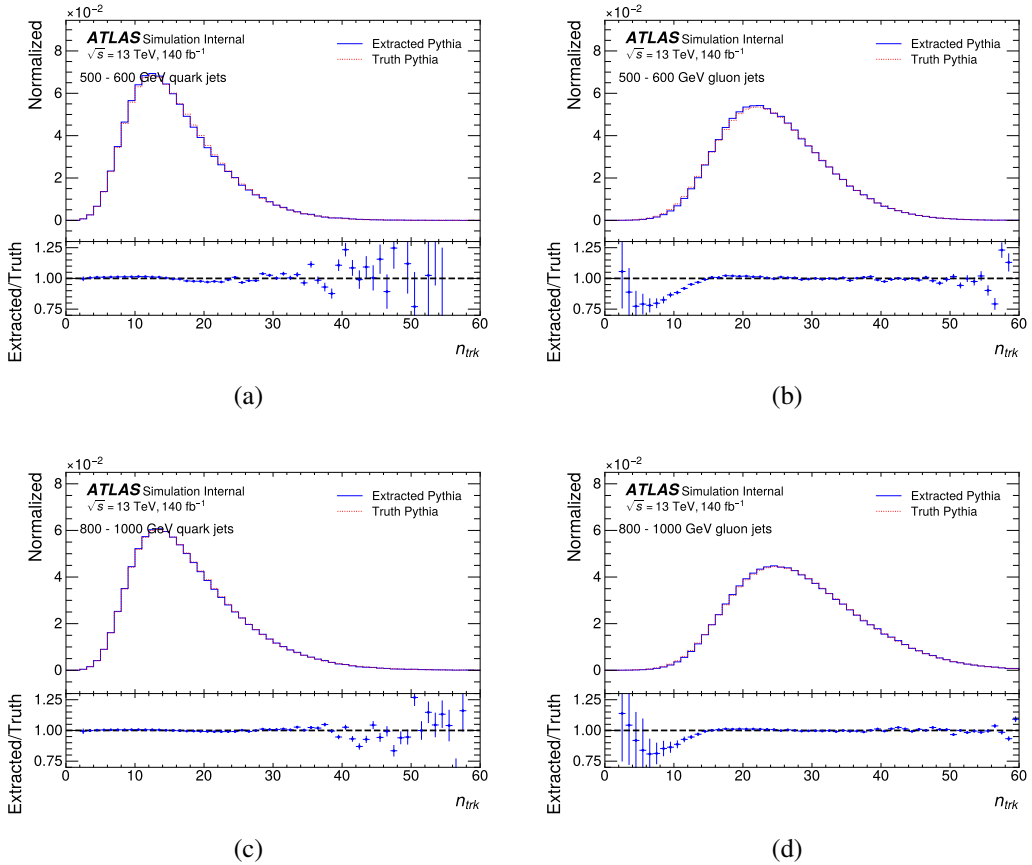


Figure 5.28 After re-weighting with quark factor: the N_{trk} distributions of quark-jet (a) (c) and gluon-jet in (b) (d) from PYTHIA 8 sample. Dashed and solid-line show the N_{trk} distributions in the truth MC and extracted MC, respectively. Bottom panels show the ratio of the extracted MC to the truth MC.

980 5.5.1 Closure test for BDT tagger

Similar to the distribution of N_{trk} , the distributions of BDT score for truth labelled-jets exhibit systematic disparities in forward and central regions. Therefore, the same re-weighting procedure as described is performed for BDT tagger as well. The MC non-closure test is thus conducted by comparing the distributions of BDT score for extracted and truth quark- and gluon-jets, separately, as shown in Figure 5.29. The distributions of BDT before and after re-weighting are shown in Figure 5.30 and Figure 5.31. The non-closure is about few percent level and taken as one systematic uncertainty.

The calibration of quark/gluon jets taggers

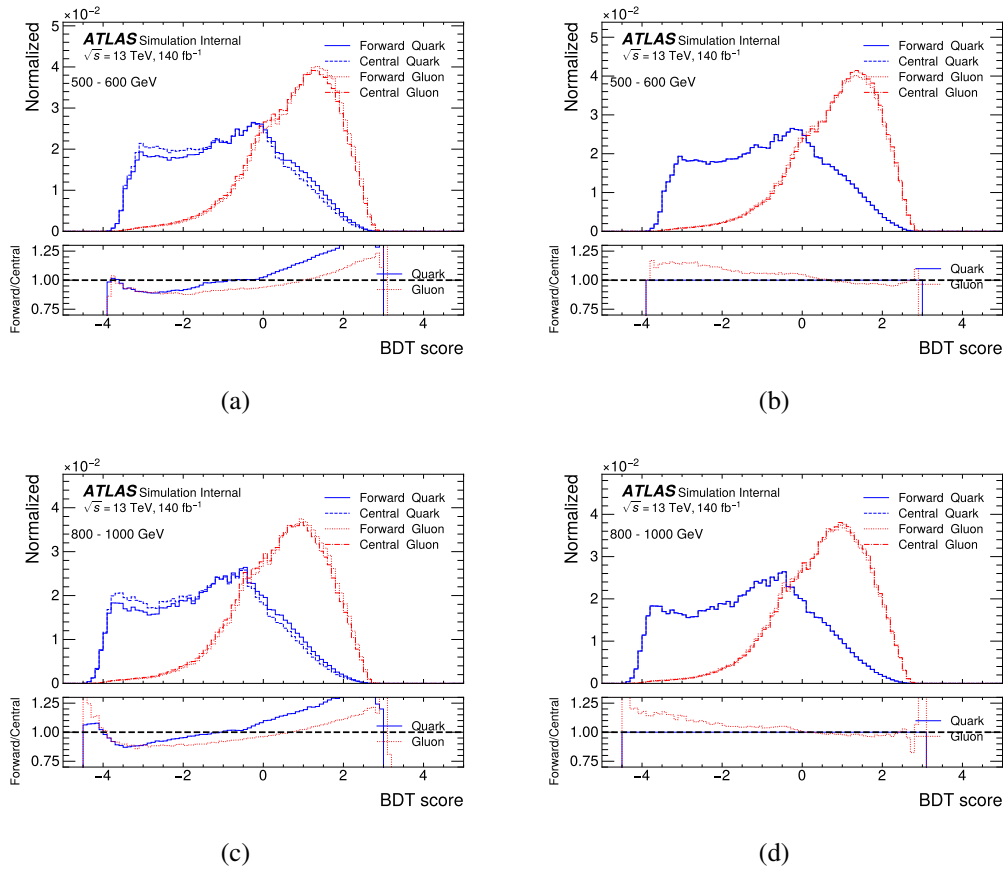


Figure 5.29 The distribution of BDT score for jets before (a) (c) and after (b) (d) re-weighting.

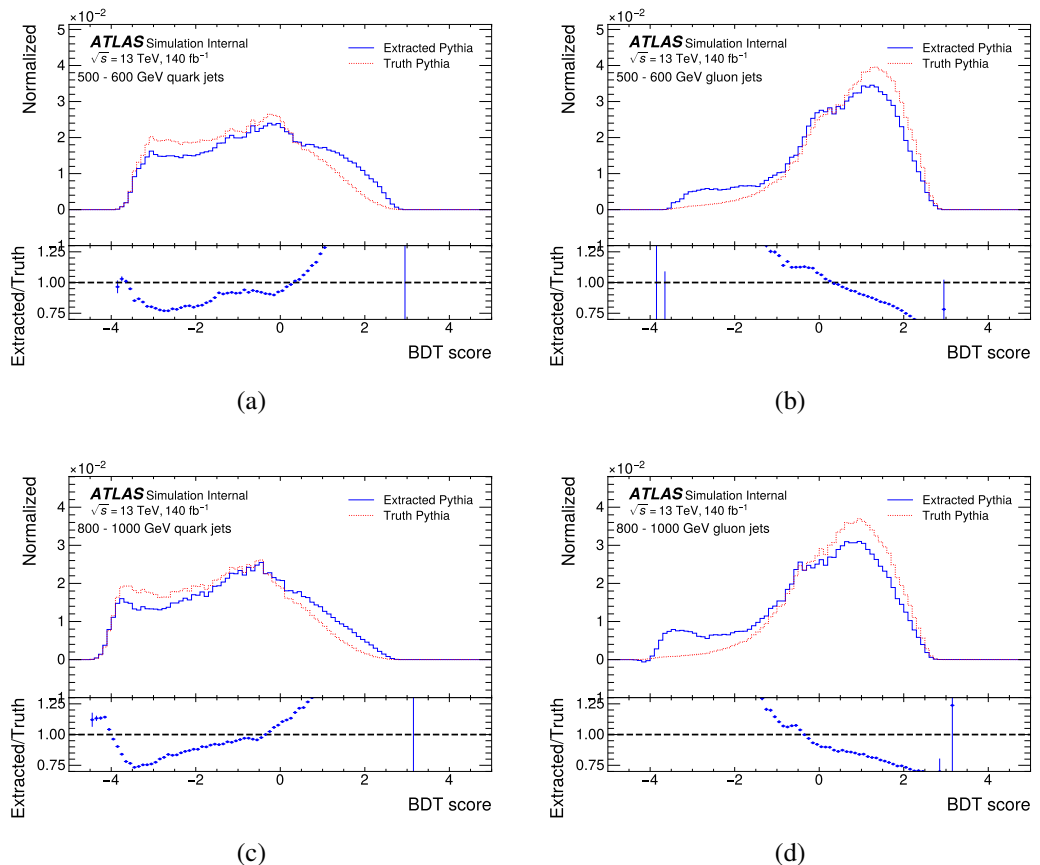


Figure 5.30 Before re-weighting: the MC-closure for quark-jet in (a) (c) and for gluon-jet in (b) (d) in BDT distributions from PYTHIA 8 sample. Dashed and solid-line histograms show the BDT distributions in the truth MC and extracted MC, respectively. Bottom panels show the ratio of the extracted MC to the truth MC.

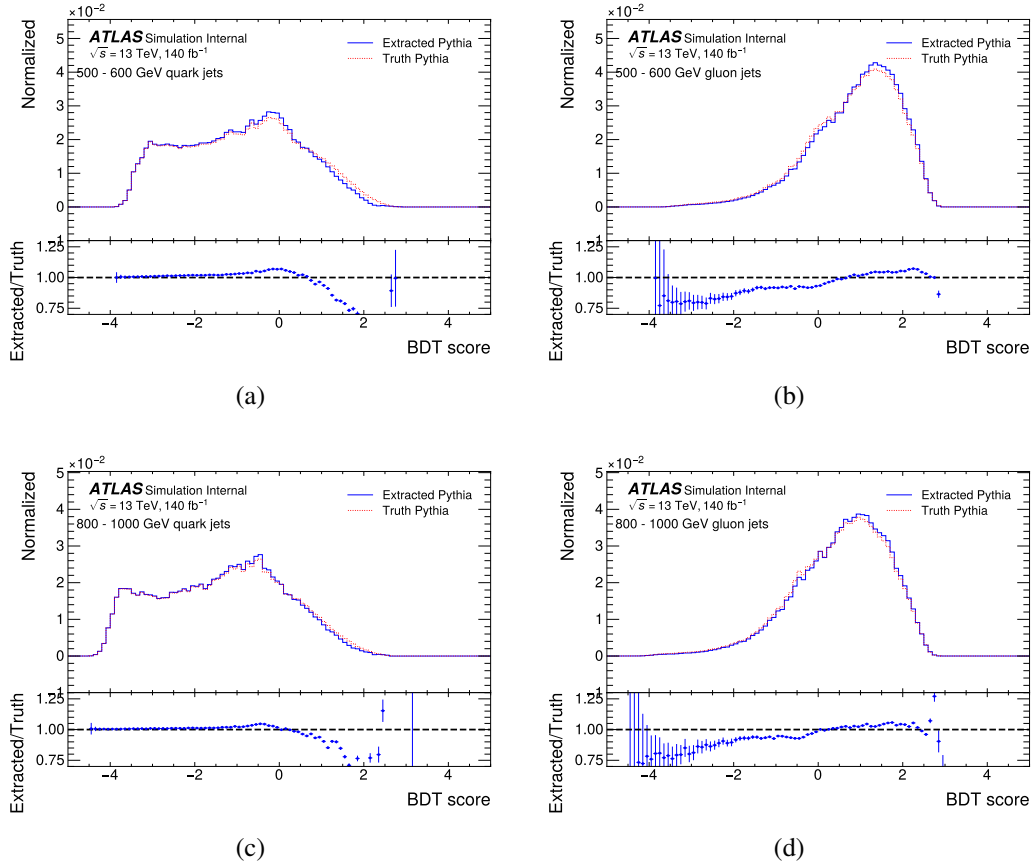


Figure 5.31 After re-weighting: the MC-closure for quark-jet in (a) (c) and for gluon-jet in (b) (d) in BDT distributions from PYTHIA 8 sample. Dashed and solid-line histograms show the BDT distributions in the truth MC and extracted MC, respectively. Bottom panels show the ratio of the extracted MC to the truth MC.

988 **5.5.2 Summary for the MC Closure test**

989 After applied the re-weighting factor to the jet tagging variables N_{trk} and BDT, the
 990 distributions of extracted quark-and gluon-jets converge with those of truth jets. The
 991 residual discrepancy, which has only few percent level to the total events is taken into
 992 account as MC non-closure systematic uncertainty. No obvious dependency on jet η is
 993 observed from the distributions of jet tagging variables.

994 **5.6 Scale factor**

995 The calibration of the q/g tagging variables is performed by applying binned scale
 996 factor (SF) in the simulation for each quark- and gluon-jet, respectively. The scale factor
 997 is obtained from distributions of the variables in quark- and gluon-jets from MC in order
 998 to match the shape of the simulation to that of the data.

999 The tagger working points (WP) are established for fixed quark-jets efficiency in
 1000 the nominal MC sample, for both taggers. At a given working point, the efficiencies for
 1001 quark- and gluon-jets are defined as follows:

$$\epsilon_{Q/G}(x^{WP}) = \int_{x < x^{WP}} p_{Q/G}(x) dx. \quad (5.9)$$

1002 Rejection factors corresponding to quark- and gluon-jets can also be given as:

$$\xi_{Q/G}(x^{WP}) = 1 / \int_{x > x^{WP}} p_{Q/G}(x) dx = 1 / (1 - \epsilon_{Q/G}(x^{WP})). \quad (5.10)$$

1003 Discrepancies observed between the quark-jet tagging efficiencies and gluon-jet re-
 1004 jections obtained from data and the corresponding values anticipated from the MC sim-
 1005 ulations are quantified using data-to-MC scale factors (SF). These factors are computed
 1006 separately for each q/g tagger in various p_T bins, at a fixed WP. The SF is defined using
 1007 Equation 5.9 and 5.10 for quark- and gluon-jets, respectively :

$$\text{SF}_Q(x^{WP}) = \frac{\epsilon_Q^{\text{Data}}(x^{WP})}{\epsilon_Q^{\text{MC}}(x^{WP})}. \quad (5.11)$$

$$\text{SF}_G(x^{WP}) = \frac{\xi_G^{\text{Data}}(x^{WP})}{\xi_G^{\text{MC}}(x^{WP})}. \quad (5.12)$$

1008 where $\varepsilon_{Q/G}^{\text{Data}}(x^{WP})$ and $\varepsilon_{Q/G}^{\text{MC}}(x^{WP})$ are $\varepsilon_{Q/G}(x^{WP})$ in data and MC, respectively. Same defi-
1009 nitions apply to $\xi_{Q/G}(x^{WP})$. The WPs corresponding to fixed quark-jets tagging efficien-
1010 cies of 50%, 60%, 70%, and 80% have been examined, revealing analogous trends in the
1011 characteristics of SFs.

1012 Figure 5.32 to 5.35 show the distribution of all jet tagging variables in quark- and
1013 gluon-jets after matrix method extraction in all different MC samples and data in given
1014 p_T range.

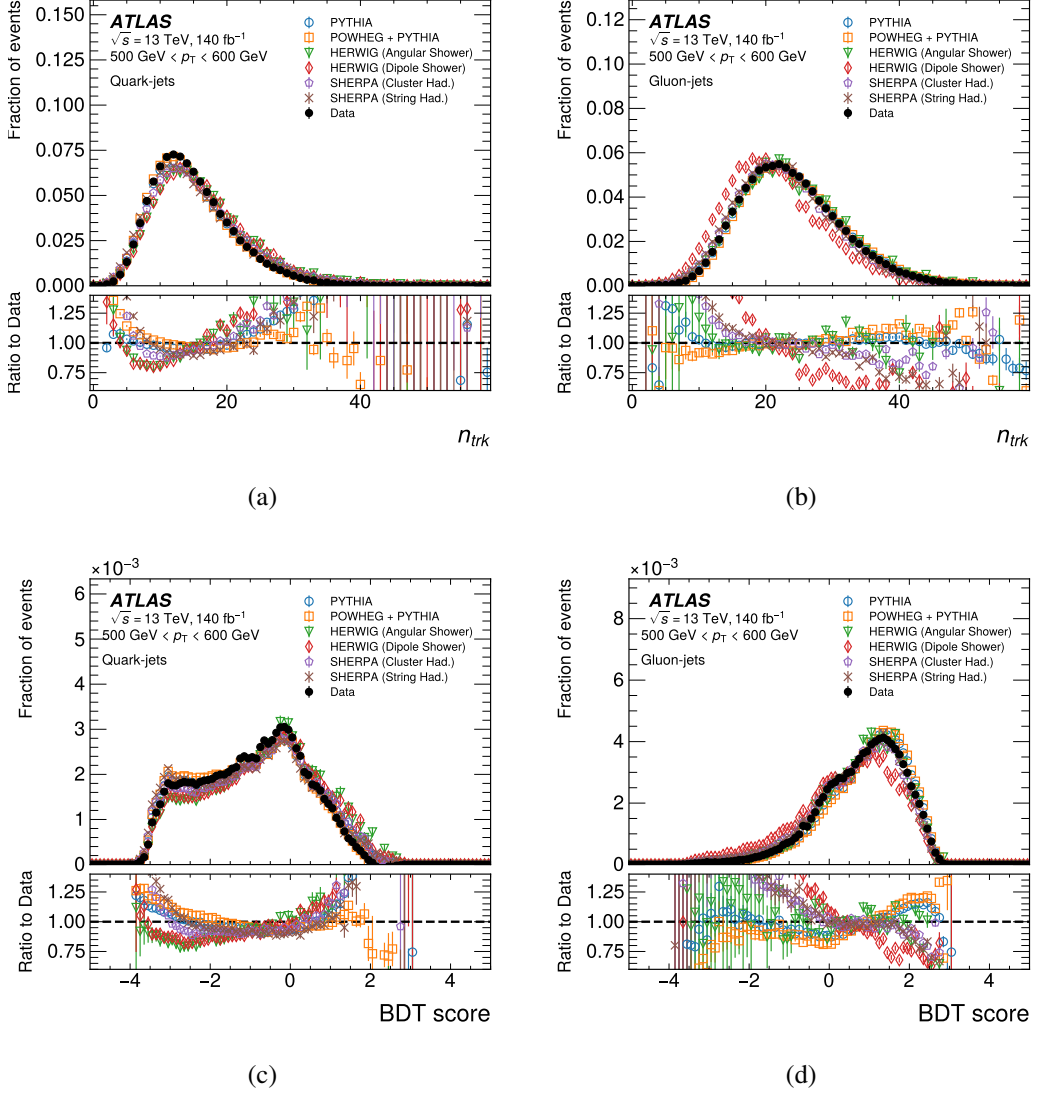


Figure 5.32 The distributions of N_{trk} (a,b) and BDT score (c,d) for quark-jets (left) and gluon-jets (right) using different generators (open symbols) and data (closed symbol) are shown in the upper panels. The lower panels show the ratio of each MC distribution and the data. The vertical error bars show the statistical uncertainty.

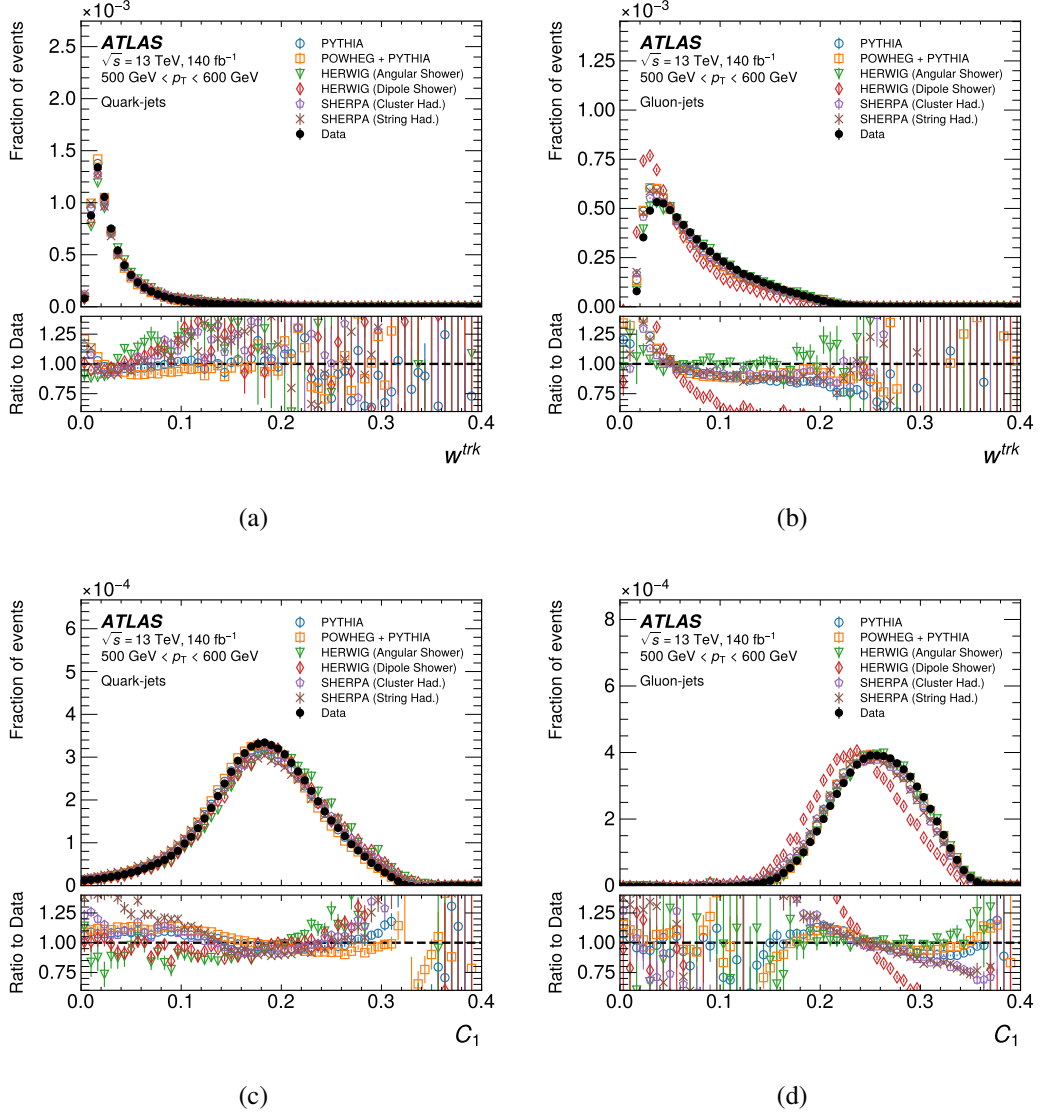


Figure 5.33 The distributions of W_{trk} (a,b) and C_1 (c,d) for quark-jets (left) and gluon-jets (right) using different generators (open symbols) and data (closed symbol) are shown in the upper panels. The lower panels show the ratio of each MC distribution and the data. The vertical error bars show the statistical uncertainty.

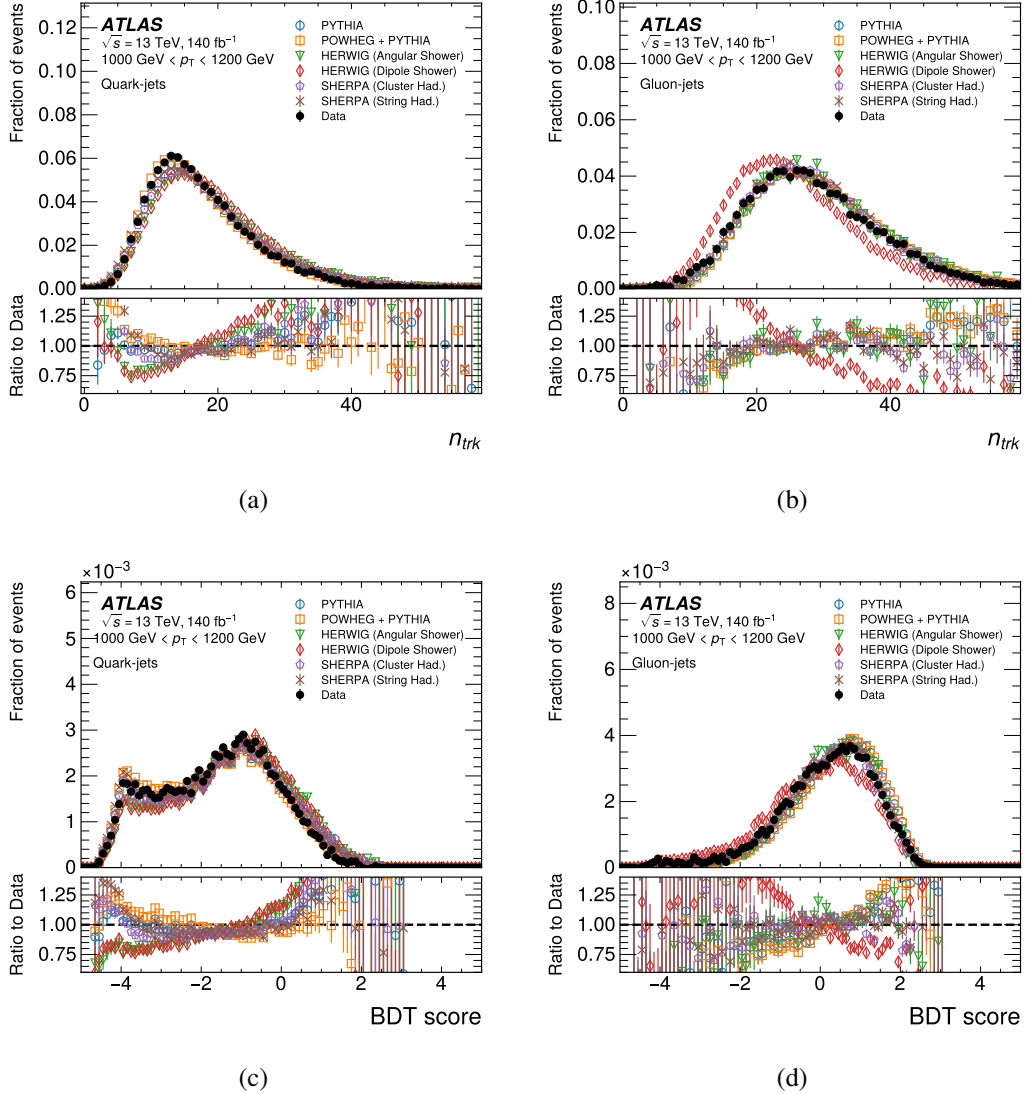


Figure 5.34 The distributions of N_{trk} (a,b) and BDT score (c,d) for quark-jets (left) and gluon-jets (right) using different generators (open symbols) and data (closed symbol) are shown in the upper panels. The lower panels show the ratio of each MC distribution and the data. The vertical error bars show the statistical uncertainty.

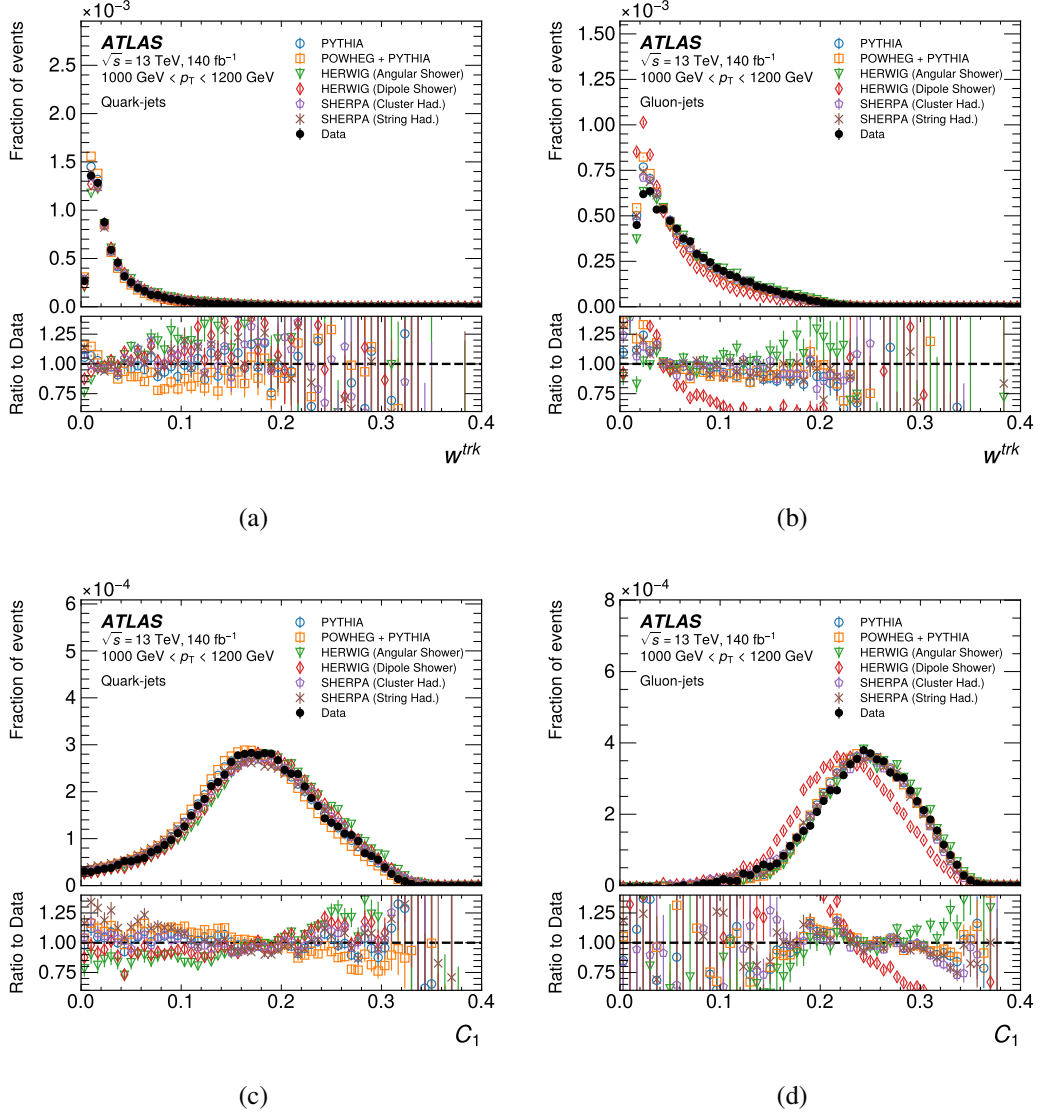


Figure 5.35 The distributions of W_{trk} (a,b) and C_1 (c,d) for quark-jets (left) and gluon-jets (right) using different generators (open symbols) and data (closed symbol) are shown in the upper panels. The lower panels show the ratio of each MC distribution and the data. The vertical error bars show the statistical uncertainty.

1015 Cut values corresponding to the 50% WP are summarised in Table 5.4 for the N_{trk} -
 1016 only tagger and Table 5.5 for the BDT-tagger. Figure 5.36 shows the gluon-jets efficiency
 1017 of both N_{trk} -only tagger and the BDT-tagger as a function of jet p_{T} , for the MC and data,
 1018 at four WPs.

1019 Both the N_{trk} -only and BDT-taggers demonstrate commendable performance on
 1020 data, with high quark signal efficiency across all p_{T} range. Notably, at the 50% work-
 1021 ing point, the N_{trk} -only tagger achieves approximately 90% rejection of gluon-jets, while
 1022 the BDT tagger surpasses this performance by rejecting around 93% of gluon-jets. The
 1023 BDT-tagger outperforms the N_{trk} -only tagger by exhibiting superior gluon-jets rejection
 1024 rates at the identical WP. This disparity in performance arises from the inclusion of a
 1025 more comprehensive set of jet substructure variables in the BDT approach. The discrep-
 1026 arity between the level of gluon-jet rejection observed in data and that predicted by the
 1027 MC samples increases as the jet p_{T} increases. This phenomenon is closely tied to the
 1028 dissimilarity between the modelling of gluons and their actual behaviour in data.

p_{T} [GeV]	500 - 600	600 - 800	800 - 1000	1000 - 1200	1200 - 1500	1500 - 2000
WP						
0.5	15.0	16.0	17.0	18.0	18.0	19.0
0.6	17.0	18.0	19.0	20.0	20.0	21.0
0.7	19.0	20.0	21.0	22.0	23.0	24.0
0.8	22.0	23.0	24.0	26.0	27.0	28.0

Table 5.4 Cut values of N_{trk} at different working point in each of jet p_{T} range

p_{T} [GeV]	500 - 600	600 - 800	800 - 1000	1000 - 1200	1200 - 1500	1500 - 2000
WP						
0.5	-0.8	-1.0	-1.2	-1.4	-1.6	-1.8
0.6	-0.4	-0.6	-0.8	-1.0	-1.2	-1.4
0.7	0.0	-0.2	-0.4	-0.6	-0.8	-1.0
0.8	0.4	0.2	0.0	-0.2	-0.3	-0.6

Table 5.5 Cut values of BDT at different working point in each of jet p_{T} range

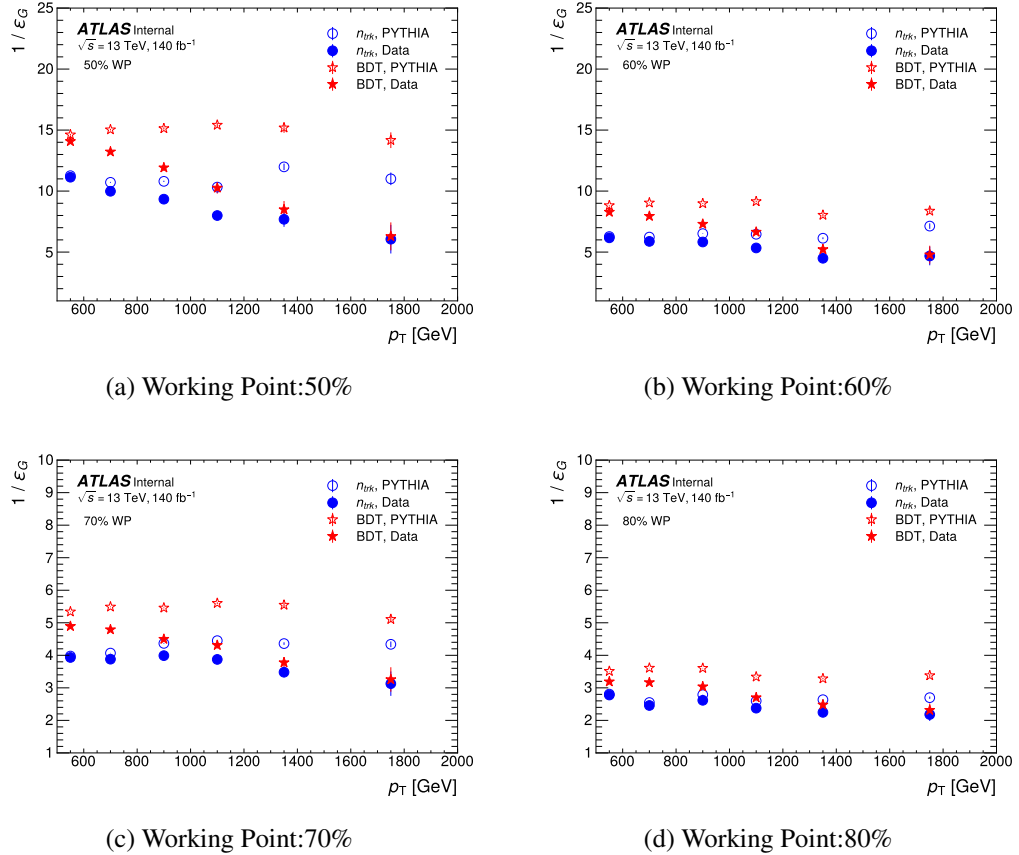


Figure 5.36 Inverse of the gluon-jet efficiency of N_{trk} (circles) and BDT (stars) as a function of jet p_T at the each WP in data (closed symbols) and the PYTHIA (open symbols) MC. The vertical error bars show the statistical uncertainty.

1029 **5.7 Systematic uncertainties**

1030 In this study, different types of systematic uncertainty are taken into account. The
1031 distribution of N_{trk} and BDT for truth-labelled quark-/gluon-jets are given by the MC
1032 simulation samples, therefore, theoretical uncertainties originate from aspects encom-
1033 passing the modelling of the MC simulation, such as choices involving parton showering,
1034 hadronisation, matrix element, PDFs, scale variations, and Splitting-Kernel effects. Fur-
1035 thermore, experimental uncertainties such as JES and JER, tracking reconstruction effi-
1036 ciencies are meticulously incorporated. The potential impact of methodological choices,
1037 including N_{trk} or BDT re-weighting, as well as the non-closure behaviour of MC simula-
1038 tions, is propagated to the resultant SFs.

1039 The nominal result in this analysis is provided using PYTHIA 8 MC samples, all
1040 other MC samples are considered as alternative samples to study corresponding system-
1041 atic uncertainty.

1042 **5.7.1 Parton shower modelling uncertainty**

1043 The different chose of algorithmic or parametric in the modelling of the parton
1044 shower could result in different SF result. This systematic uncertainty is estimated by
1045 comparing the SFs extracted from two MC samples with the same ME and hadronisation
1046 but different types of showers: HERWIG Angular-ordered and HERWIG Dipole samples.
1047 The corresponding fractions of quarks and gluons present in these two MC samples, are
1048 presented in Figure 5.37. The difference of extracted SFs between these two samples is
1049 less than 10% for quark signal efficiency and around 20% for gluon rejection efficiency.
1050 While the influence on quark scale factors is negligible, it takes on a dominant role in the
1051 context of gluon scale factors.

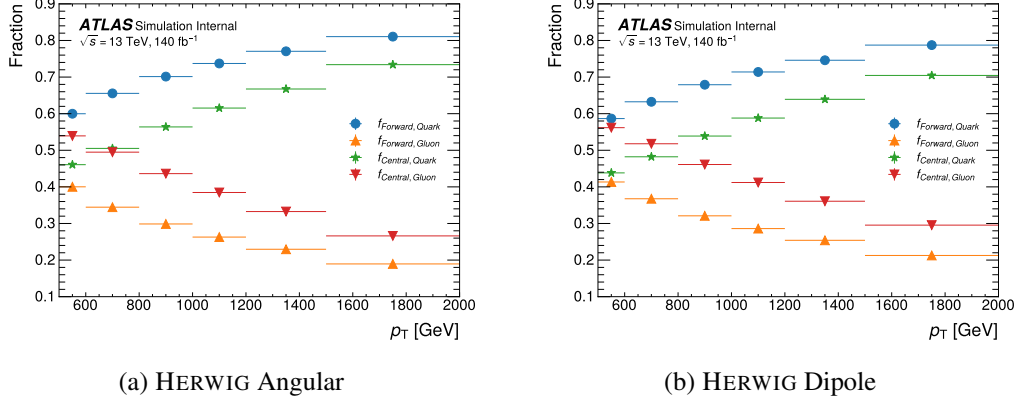


Figure 5.37 Fractions of quark- gluon-jets of HERWIG angular (a) and HERWIG dipole (b) samples.

1052 5.7.2 Hadronisation modelling uncertainty

1053 The uncertainty from hadronisation modelling is given by the difference between
 1054 the extracted SFs from the SHERPA MC samples with cluster-based hadronisation mod-
 1055 elling and string-based hadronisation modelling, separately. The corresponding fractions
 1056 of quarks and gluons present in these two MC samples are presented in Figure 5.38. The
 1057 uncertainty on the SFs range from 1% to 8% for both jet types.

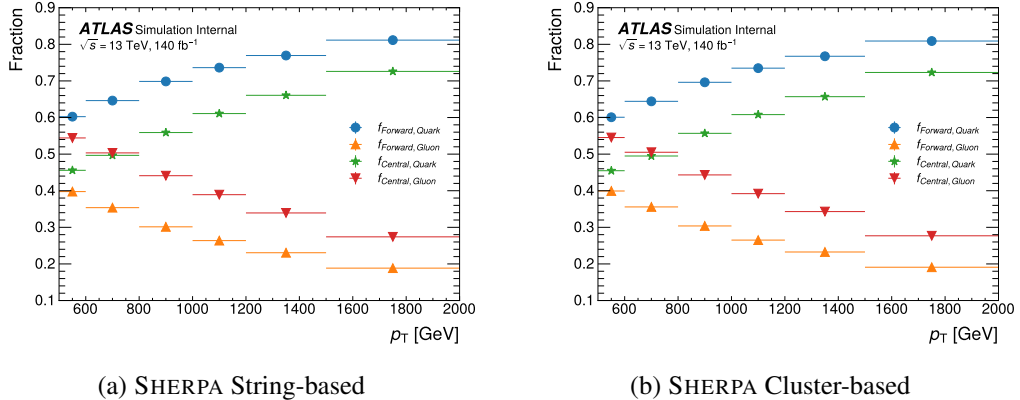


Figure 5.38 Fractions of quark- and gluon-jets in each SHERPA sample.

1058 5.7.3 Matrix element uncertainty

1059 The uncertainty introduced by different types of ME in the MC samples is taken
 1060 from the differences in the extracted SFs in two MC samples with different ME : POWHEG and
 1061 PYTHIA . The corresponding fractions of quarks and gluons present in the POWHEG sam-
 1062 ples are presented in Figure 5.39.

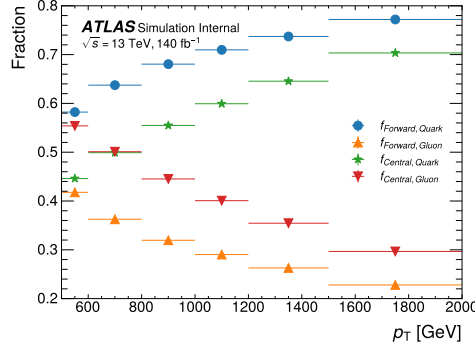


Figure 5.39 Fractions of quark jets and gluon jets in POWHEG samples.

1063 5.7.4 PDF uncertainty

1064 The uncertainty from the PDF set is evaluated using LHAPDF package which pro-
 1065 vides the PDF internal variations for each PDF set, a NNPDF2.3 set is chosen to eval-
 1066 uate the various weights which depend on the momentum fraction. The PDF uncertainty
 1067 is given by changing the nominal PDF weight to the systematic variation, then compare
 1068 the SFs extracted from each of variations. The PDF uncertainty is around 5% - 7% level
 1069 and almost negligible compared to others.

1070 5.7.5 Scale variation uncertainty

1071 The variation of the renormalisation (μ_R) and factorisation (μ_F) scales in QCD is
 1072 used to evaluate the uncertainty caused by missing higher order corrections. The nominal
 1073 PYTHIA sample is used for such estimation. In total there are 7 scale variations (μ_R, μ_F)
 1074 in (2,2), (2,1), (1,1), (1,2), (1,0.5), (0.5,1), (0.5,0.5) studied in this analysis. The scale
 1075 uncertainty is given by taking the maximum shift of the envelope with respect to the
 1076 nominal one at each working points. The total scale uncertainty is around 4% - 7%.

1077 **5.8 Splitting-Kernel variation uncertainty**

1078 All formulations of shower processes are constructed on the fundamental founda-
1079 tion of the universal behavior exhibited by singular infrared (soft and/or collinear) lim-
1080 its within QCD. Nonetheless, when one ventures beyond these limits into the physical
1081 phase space where these kernels are employed as approximations, there are in principle
1082 infinitely many different radiation functions to choose from, sharing the same singular
1083 terms but having different non-singular ones. The Splitting-Kernel variations are vari-
1084 ations of the non singular part of the splitting functions, for initial-state radiation and
1085 final-state radiation. Such uncertainty is less than 1%.

1086 **5.9 Tracking uncertainty**

1087 he number of associated tracks is the most important input for both taggers, with
1088 tracking-related systematics exerting an impact on the measurement of SFs. he uncer-
1089 tainty associated with reconstructed tracks is partitioned into two components: the un-
1090 certainty pertaining to track reconstruction efficiency and the MC fake rate [?]. Both
1091 sources of uncertainty are factored in to recalibrate the count of tracks associated with
1092 jets.

1093 The track reconstruction efficiency uncertainty originates from material-related un-
1094 certainties, which constitutes the prevailing source, as well as from considerations related
1095 to the physics model. These uncertainties are estimated through a comparison of track
1096 efficiency across samples that encompass diverse detector modelling configurations. On
1097 the other hand, the MC fake rate is determined by contrasting the trends in a specific
1098 aspect of track multiplicity as a function of the average number of interactions per bunch
1099 crossing between empirical data and the MC simulation. The disparity in final SFs be-
1100 tween the nominal value and the outcome of the systematic variation contributes to the
1101 tracking systematic uncertainty. This uncertainty spans a range of approximately 1% to
1102 8%.

1103 **5.10 JES /JER uncertainty**

1104 The uncertainties associated with JES stem from the process of calibrating the trans-
1105 verse momentum balance between jets located in the central and forward regions, while
1106 also accommodating uncertainties linked to single-particle and test beam measurements.

1107 The JER uncertainties encompass the disparities between data and the MC. For each
 1108 JES/JER variation, a corresponding SF is derived, and the difference between the nom-
 1109 inal value and the variation is computed to determine the systematic uncertainty. The
 1110 cumulative JES/JER uncertainty amounts to approximately 0.2%.

1111 **5.10.1 N_{trk} / BDT re-weighting**

1112 The quark-enriched and gluon-enriched regions are defined by comparing the η of
 1113 leading and subleading jets, introduces to an η dependency from track reconstruction
 1114 process. A re-weighting factor defined by Equation 5.8 is applied on N_{trk} and BDT
 1115 taggers for each event to reduce the impact from different track multiplicity in different
 1116 η range. The re-weighting factors acquired from truth-labelled gluon jets are regarded
 1117 as an alternative source of contribution to the systematic uncertainty. It's worth noting
 1118 that the differences arising from the re-weighting procedure remain comparatively minor
 1119 (about 0.1% - 0.5%) in comparison to other sources of uncertainty.

1120 The distributions of N_{trk} and BDT for extracted quark and gluon-jets after re-weighting
 1121 with quark factor have been shown in the previous chapter. The truth distribution of
 1122 quark/gluon in forward/central jets using gluon factors are shown in Figure 5.40 for
 1123 N_{trk} and Figure 5.41 for BDT, respectively. Figure 5.42, Figure 5.43 shows the distribu-
 1124 tions of extracted quark and gluon-jets after reweighting with gluon factor.

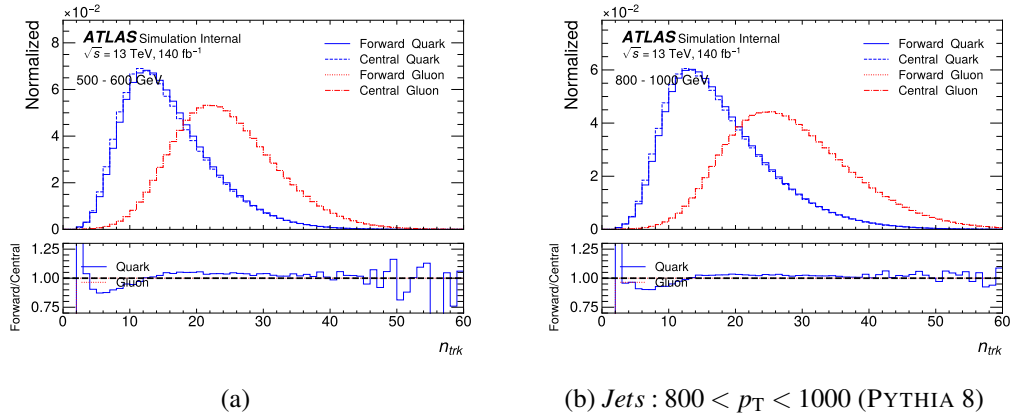


Figure 5.40 The distribution of N_{trk} for jets between 500-600 GeV (a) and 800-1000 GeV (b) after N_{trk} re-weighting using gluon factor.

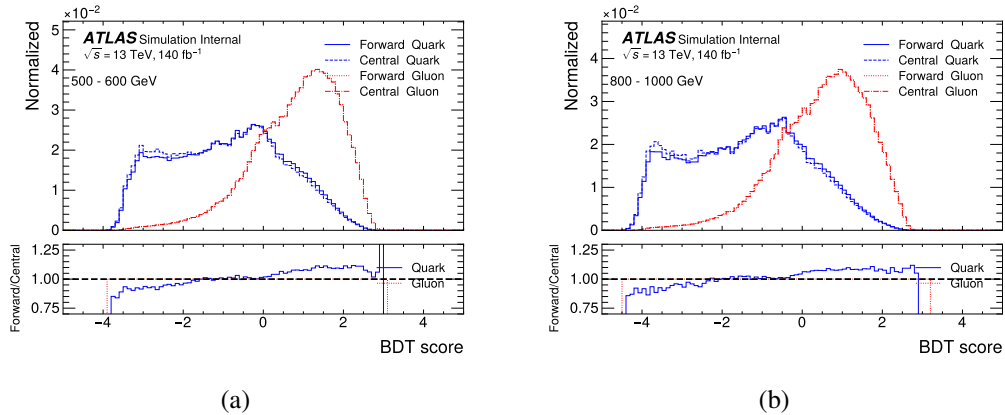


Figure 5.41 The distribution of BDT for jets between 500-600 GeV (a) and 800-1000 GeV (b) after re-weighting using gluon factor.

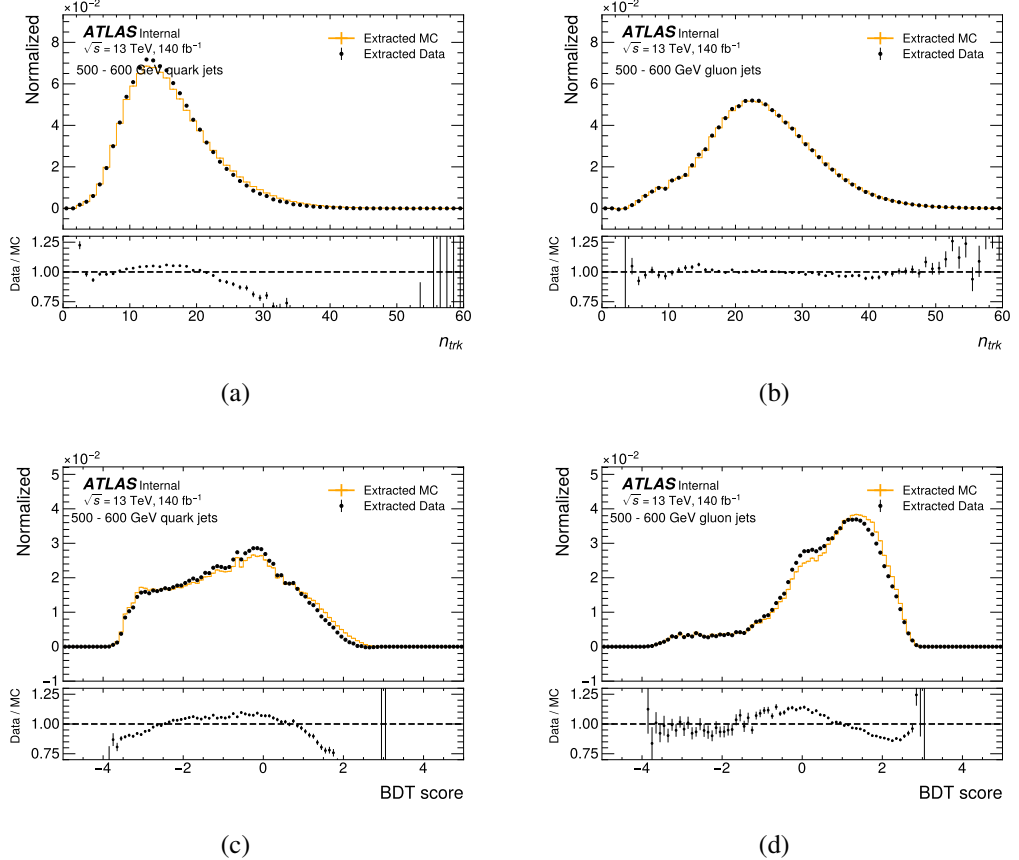


Figure 5.42 The n_{trk} (top) and BDT (bottom) distributions extracted by the matrix method from the data and MC of pure quark-jets (a) (c) and gluon-jets ?? (d) by PYTHIA 8. extracted by the matrix method from the data and MC. The gluon factor is applied. Solid-line histograms show the distributions of quark or gluon-jets defined by the jet parton flavour label in the MC. A bottom panel in each figure shows the ratio of the extracted data to the extracted MC by the matrix method.

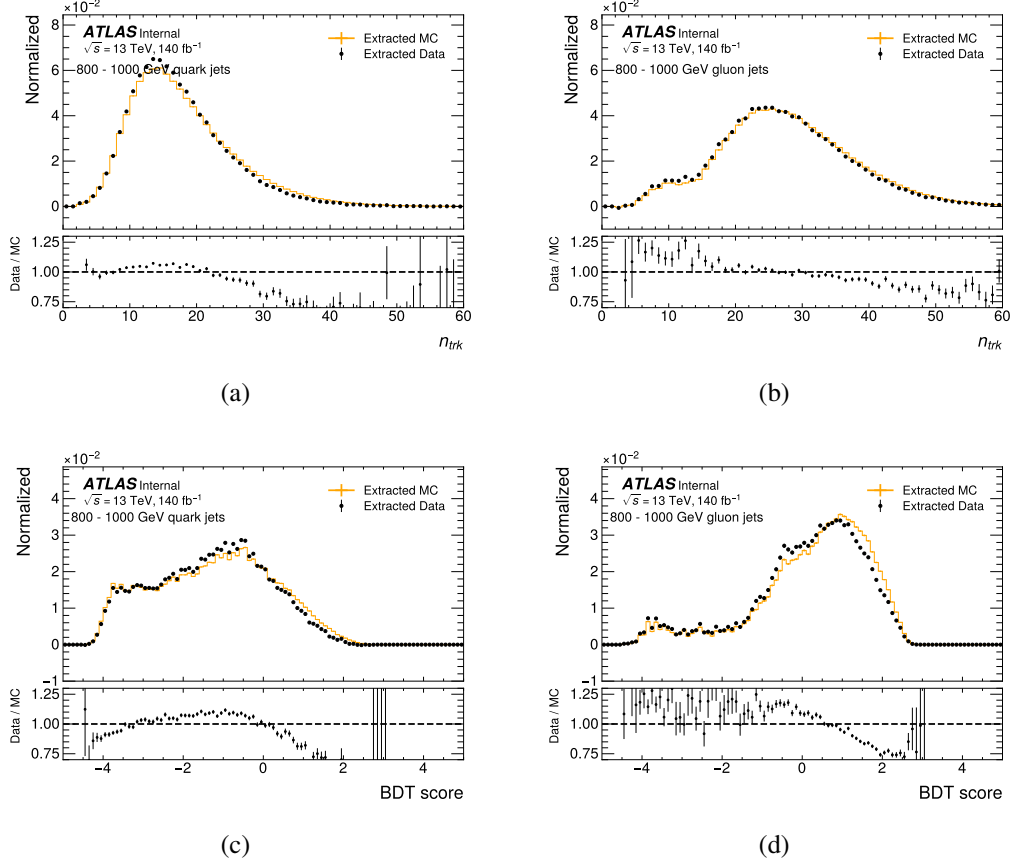


Figure 5.43 The N_{trk} (top) and BDT (bottom) distributions extracted by the matrix method from the data and MC of pure quark-jets (a) (c) and gluon-jets (b) (d) by PYTHIA 8. extracted by the matrix method from the data and MC. The gluon factor is applied. Solid-line histograms show the distributions of quark or gluon-jets defined by the jet parton flavour label in the MC. A bottom panel in each figure shows the ratio of the extracted data to the extracted MC by the matrix method.

5.10.2 The MC non-closure

As described in Section 5.5, the MC closure test is conducted using MC samples wherein each jet is assigned a truth label. After re-weighting, the distributions of N_{trk} and BDT obtained through the matrix method exhibit consistency with the truth-labelled ones for quark- and gluon-jets, respectively. The remaining difference for both taggers is only 1% level.

5.10.3 Statistical uncertainty

The estimation of statistical uncertainty involves a stepwise process. It commences by varying the input data/MC distributions bin-by-bin, using Poisson/Gaussian distributions wherein the number of data events within each bin serves as the central value. These variations of the input histograms yield templates, subsequently employed as inputs for the template variations technique. This procedure is iterated 5000 times, with the standard deviation of these uncertainties of all toys taken is used to derive the statistical uncertainty of the SFs. This uncertainty is around 0.1%.

The distributions of SFs are shown in 5.44 for N_{trk} and 5.45 for the BDT.

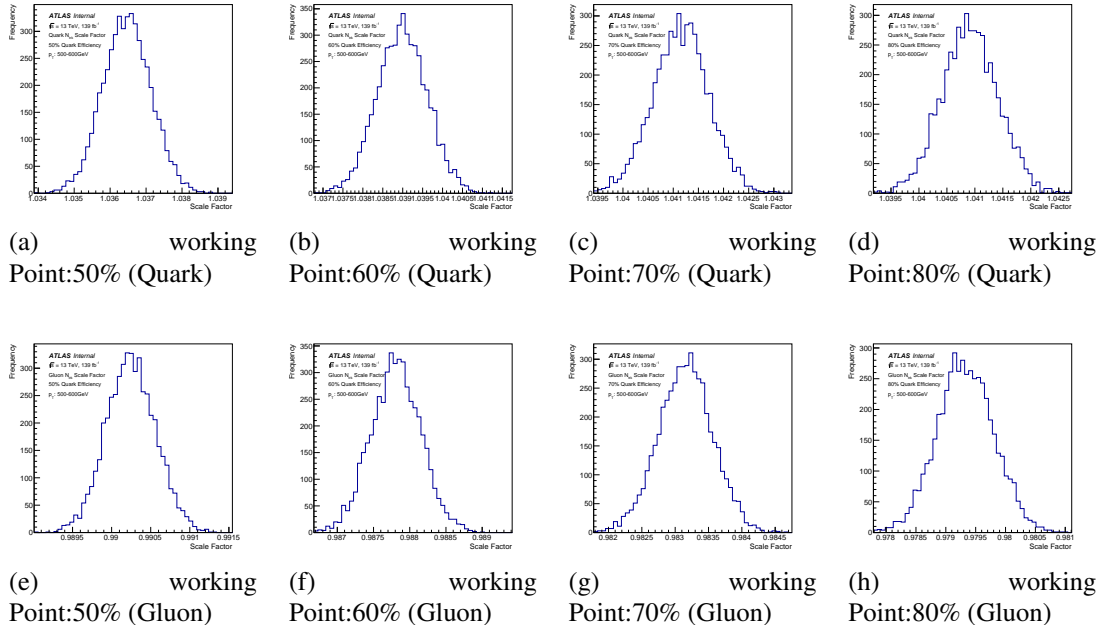


Figure 5.44 The distribution of SF by varying the input data distributions bin-by-bin using a Poisson distribution with the number of data events in each bin as the central value for 5000 times for working point of N_{trk} in jet p_T range 500-600 GeV.

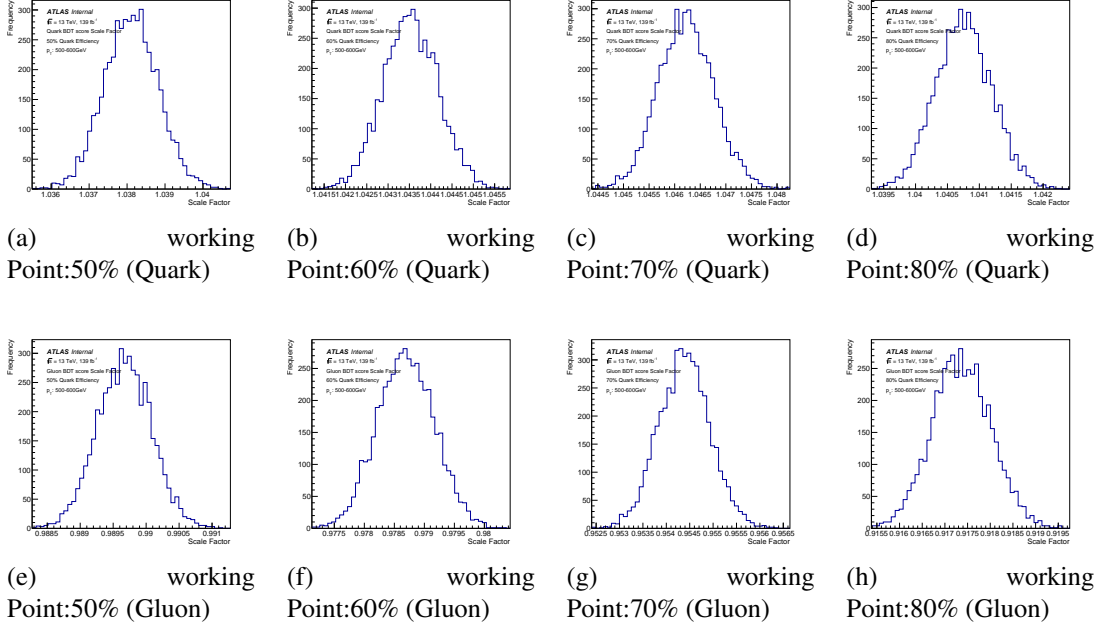


Figure 5.45 The distribution of SF by varying the input data distributions bin-by-bin using a Poisson distribution with the number of data events in each bin as the central value for 5000 times for working point of BDT in jet p_T range 500-600 GeV.

1139 5.11 Results

1140 Overall, both the N_{trk} -only tagger and the BDT-tagger exhibit commendable performance,
 1141 and can effectively distinguish quark-jet from gluon-jet with high efficiency. The
 1142 SFs for both quark- and gluon-jet fall within the range of approximately 0.9 to 1, indicating
 1143 a reasonable agreement. The systematic uncertainty for quark-jet SFs hovers around
 1144 10%, while for gluon-jet SFs it's approximately 20%. Detailed of each uncertainty are
 1145 shown in Section 5.7. The BDT-tagger showcases a slightly superior performance compared
 1146 to the N_{trk} only tagger, i.e. higher gluon-jet rejection at the same WP.

1147 The uncertainties of SF for each source of WP are estimated in each jet p_T range
 1148 are given from Table 5.6 to Table 5.13 for quark-jets. Table 5.14 to Table 5.21 show the
 1149 uncertainties of SF at each WP for gluon-jets. All systematics are ordered from largest to
 1150 smallest in p_T range 500 - 600 GeV. the systematic uncertainties associated with quark-
 1151 jet scale factors tend to be smaller than those linked to gluon-jet scale factors. Notably,

¹¹⁵² for both quark- and gluon-jets, these uncertainties are primarily governed by the source
¹¹⁵³ of uncertainty stemming from parton showering.

Table 5.6 The quark scale factor (nominal) and the difference between the nominal and systematic variation results for 50% quark tag efficiency from $N_{\text{trk}}\text{tagger}$

	500-600	600-800	800-1000	1000-1200	1200-1500	1500-2000
nominal	1.02	1.04	1.04	1.03	1.02	1.01
scale variation	0.09	0.1	0.12	0.11	0.13	0.12
pdf weight	0.09	0.11	0.12	0.13	0.13	0.11
hadronization	0.09	0.07	0.06	0.05	0.04	0.04
tracking	0.08	0.07	0.06	0.05	0.05	0.04
matrix element	0.05	0.06	0.06	0.05	0.05	0.04
parton shower	0.02	0.03	0.05	0.06	0.07	0.08
MC nonclosure	0.02	0.04	0.04	0.03	0.02	0.01
splitting kernel	0.01	0.01	0.01	0.01	0.01	0.01
JES/JER	0.01	0.01	0.01	0.01	0.01	0.01
gluon reweight	0.01	0.01	0.01	0.01	0.01	0.01
Statistical	0.01	0.01	0.01	0.01	0.01	0.02
Total Uncertainty	0.19	0.19	0.21	0.21	0.22	0.19

Table 5.7 The quark scale factor (nominal) and the difference between the nominal and systematic variation results for 60% quark tag efficiency from $N_{\text{trk}}\text{tagger}$

	500-600	600-800	800-1000	1000-1200	1200-1500	1500-2000
nominal	1.03	1.04	1.04	1.03	1.01	1.01
pdf weight	0.09	0.1	0.12	0.12	0.12	0.1
tracking	0.08	0.07	0.06	0.05	0.05	0.04
scale variation	0.07	0.08	0.1	0.09	0.1	0.09
hadronization	0.06	0.05	0.04	0.04	0.03	0.03
matrix element	0.05	0.05	0.05	0.05	0.05	0.04
MC nonclosure	0.02	0.04	0.04	0.03	0.02	0.02
parton shower	0.02	0.03	0.03	0.04	0.06	0.08
splitting kernel	0.01	0.01	0.01	0.02	0.01	0.01
JES/JER	0.01	0.01	0.01	0.01	0.01	0.01
gluon reweight	0.01	0.01	0.01	0.01	0.01	0.01
Statistical	0.01	0.01	0.01	0.01	0.01	0.01
Total Uncertainty	0.16	0.17	0.18	0.18	0.18	0.17

The calibration of quark/gluon jets taggers

Table 5.8 The quark scale factor (nominal) and the difference between the nominal and systematic variation results for 70% quark tag efficiency from N_{trk} tagger

	500-600	600-800	800-1000	1000-1200	1200-1500	1500-2000
nominal	1.03	1.04	1.04	1.03	1.02	1.0
pdf weight	0.08	0.09	0.11	0.11	0.11	0.08
tracking	0.07	0.06	0.05	0.05	0.04	0.03
scale variation	0.06	0.06	0.07	0.07	0.07	0.06
hadronization	0.05	0.04	0.04	0.03	0.03	0.02
matrix element	0.04	0.05	0.04	0.04	0.04	0.03
MC nonclosure	0.03	0.04	0.04	0.04	0.02	0.01
parton shower	0.02	0.02	0.02	0.03	0.04	0.05
splitting kernel	0.01	0.01	0.01	0.02	0.02	0.01
JES/JER	0.01	0.01	0.01	0.01	0.01	0.01
gluon reweight	0.01	0.01	0.01	0.01	0.01	0.01
Statistical	0.01	0.01	0.01	0.01	0.01	0.01
Total Uncertainty	0.14	0.14	0.16	0.16	0.15	0.13

Table 5.9 The quark scale factor (nominal) and the difference between the nominal and systematic variation results for 80% quark tag efficiency from N_{trk} tagger

	500-600	600-800	800-1000	1000-1200	1200-1500	1500-2000
nominal	1.03	1.03	1.03	1.02	1.01	1.0
tracking	0.06	0.05	0.05	0.04	0.03	0.02
pdf weight	0.06	0.07	0.09	0.09	0.08	0.06
scale variation	0.03	0.04	0.05	0.04	0.04	0.05
MC nonclosure	0.03	0.04	0.04	0.03	0.02	0.01
hadronization	0.03	0.02	0.02	0.02	0.02	0.02
matrix element	0.03	0.04	0.03	0.03	0.03	0.02
parton shower	0.01	0.01	0.02	0.01	0.02	0.03
splitting kernel	0.01	0.01	0.01	0.02	0.02	0.01
JES/JER	0.01	0.01	0.01	0.01	0.01	0.01
gluon reweight	0.01	0.01	0.01	0.01	0.01	0.01
Statistical	0.01	0.01	0.01	0.01	0.01	0.01
Total Uncertainty	0.11	0.11	0.13	0.12	0.11	0.1

The calibration of quark/gluon jets taggers

Table 5.10 The quark scale factor (nominal) and the difference between the nominal and systematic variation results for 50% quark tag efficiency from BDT tagger

	500-600	600-800	800-1000	1000-1200	1200-1500	1500-2000
nominal	1.01	1.02	1.03	1.02	1.01	1.0
pdf weight	0.09	0.1	0.12	0.13	0.12	0.1
scale variation	0.09	0.1	0.12	0.12	0.13	0.1
hadronization	0.07	0.06	0.06	0.06	0.04	0.04
matrix element	0.05	0.06	0.06	0.05	0.05	0.04
tracking	0.05	0.05	0.05	0.04	0.04	0.04
MC nonclosure	0.01	0.01	0.02	0.01	0.01	0.01
parton shower	0.01	0.01	0.03	0.04	0.05	0.07
splitting kernel	0.01	0.01	0.01	0.01	0.02	0.01
gluon reweight	0.01	0.01	0.01	0.01	0.01	0.01
JES/JER	0.01	0.01	0.01	0.01	0.01	0.01
Statistical	0.01	0.01	0.01	0.01	0.01	0.02
Total Uncertainty	0.17	0.18	0.2	0.2	0.2	0.18

Table 5.11 The quark scale factor (nominal) and the difference between the nominal and systematic variation results for 60% quark tag efficiency from BDT tagger

	500-600	600-800	800-1000	1000-1200	1200-1500	1500-2000
nominal	1.02	1.03	1.04	1.03	1.02	1.01
pdf weight	0.09	0.1	0.11	0.12	0.12	0.1
scale variation	0.07	0.08	0.1	0.1	0.11	0.08
hadronization	0.06	0.05	0.05	0.05	0.03	0.04
tracking	0.05	0.05	0.05	0.04	0.04	0.04
matrix element	0.05	0.05	0.05	0.05	0.04	0.03
splitting kernel	0.01	0.01	0.01	0.01	0.02	0.01
gluon reweight	0.01	0.01	0.01	0.01	0.01	0.01
MC nonclosure	0.01	0.02	0.02	0.02	0.01	0.01
JES/JER	0.01	0.01	0.01	0.01	0.01	0.01
Statistical	0.01	0.01	0.01	0.01	0.01	0.01
parton shower	0.01	0.01	0.03	0.03	0.05	0.06
Total Uncertainty	0.15	0.16	0.18	0.18	0.18	0.15

The calibration of quark/gluon jets taggers

Table 5.12 The quark scale factor (nominal) and the difference between the nominal and systematic variation results for 70% quark tag efficiency from BDT tagger

	500-600	600-800	800-1000	1000-1200	1200-1500	1500-2000
nominal	1.03	1.04	1.04	1.03	1.02	1.02
pdf weight	0.08	0.09	0.1	0.11	0.1	0.08
scale variation	0.06	0.06	0.08	0.08	0.08	0.06
tracking	0.06	0.05	0.05	0.05	0.04	0.04
hadronization	0.05	0.04	0.04	0.04	0.03	0.03
matrix element	0.04	0.04	0.04	0.04	0.03	0.02
splitting kernel	0.01	0.01	0.01	0.02	0.01	0.01
parton shower	0.01	0.01	0.02	0.03	0.04	0.04
gluon reweight	0.01	0.01	0.01	0.01	0.01	0.01
JES/JER	0.01	0.01	0.01	0.01	0.01	0.01
MC nonclosure	0.01	0.02	0.03	0.02	0.01	0.01
Statistical	0.01	0.01	0.01	0.01	0.01	0.01
Total Uncertainty	0.13	0.13	0.15	0.15	0.15	0.12

Table 5.13 The quark scale factor (nominal) and the difference between the nominal and systematic variation results for 80% quark tag efficiency from BDT tagger

	500-600	600-800	800-1000	1000-1200	1200-1500	1500-2000
nominal	1.03	1.04	1.04	1.03	1.02	1.01
pdf weight	0.07	0.07	0.08	0.09	0.08	0.06
tracking	0.06	0.05	0.05	0.04	0.03	0.03
scale variation	0.04	0.05	0.06	0.06	0.05	0.05
hadronization	0.04	0.03	0.03	0.02	0.02	0.02
matrix element	0.03	0.04	0.03	0.03	0.02	0.02
splitting kernel	0.01	0.01	0.02	0.02	0.02	0.01
parton shower	0.01	0.01	0.02	0.02	0.02	0.03
gluon reweight	0.01	0.01	0.01	0.01	0.01	0.01
JES/JER	0.01	0.01	0.01	0.01	0.01	0.01
MC nonclosure	0.01	0.01	0.02	0.02	0.01	0.01
Statistical	0.01	0.01	0.01	0.01	0.01	0.01
Total Uncertainty	0.11	0.11	0.12	0.12	0.11	0.1

The calibration of quark/gluon jets taggers

Table 5.14 The gluon scale factor (nominal) and the difference between the nominal and systematic variation results for 50% gluon tag efficiency from N_{trk} tagger

	500-600	600-800	800-1000	1000-1200	1200-1500	1500-2000
nominal	0.99	0.98	0.98	0.96	0.94	0.92
parton shower	0.1	0.11	0.12	0.13	0.11	0.14
pdf weight	0.04	0.05	0.05	0.06	0.06	0.05
splitting kernel	0.02	0.01	0.01	0.01	0.01	0.01
tracking	0.01	0.02	0.02	0.02	0.02	0.01
hadronization	0.01	0.01	0.01	0.01	0.01	0.01
scale variation	0.01	0.01	0.01	0.01	0.01	0.01
MC nonclosure	0.01	0.01	0.02	0.04	0.06	0.07
matrix element	0.01	0.01	0.02	0.03	0.04	0.07
JES/JER	0.01	0.01	0.01	0.01	0.01	0.01
Statistical	0.01	0.01	0.01	0.01	0.01	0.02
gluon reweight	0.01	0.01	0.01	0.01	0.01	0.01
Total Uncertainty	0.11	0.12	0.13	0.15	0.15	0.18

Table 5.15 The gluon scale factor (nominal) and the difference between the nominal and systematic variation results for 60% gluon tag efficiency from N_{trk} tagger

	500-600	600-800	800-1000	1000-1200	1200-1500	1500-2000
nominal	0.99	0.98	0.97	0.95	0.92	0.91
parton shower	0.15	0.17	0.17	0.17	0.17	0.21
pdf weight	0.05	0.06	0.06	0.07	0.07	0.06
splitting kernel	0.03	0.01	0.01	0.01	0.01	0.02
scale variation	0.02	0.03	0.02	0.02	0.02	0.03
tracking	0.02	0.02	0.02	0.02	0.02	0.01
hadronization	0.01	0.01	0.01	0.01	0.01	0.01
MC nonclosure	0.01	0.02	0.02	0.04	0.07	0.08
matrix element	0.01	0.01	0.02	0.03	0.05	0.08
JES/JER	0.01	0.01	0.01	0.01	0.01	0.01
Statistical	0.01	0.01	0.01	0.01	0.01	0.03
gluon reweight	0.01	0.01	0.01	0.01	0.01	0.01
Total Uncertainty	0.17	0.18	0.18	0.2	0.2	0.25

The calibration of quark/gluon jets taggers

Table 5.16 The gluon scale factor (nominal) and the difference between the nominal and systematic variation results for 70% gluon tag efficiency from N_{trk} tagger

	500-600	600-800	800-1000	1000-1200	1200-1500	1500-2000
nominal	0.99	0.97	0.96	0.94	0.91	0.87
parton shower	0.21	0.22	0.23	0.24	0.25	0.31
pdf weight	0.06	0.06	0.07	0.08	0.08	0.07
splitting kernel	0.04	0.01	0.01	0.01	0.01	0.01
scale variation	0.04	0.04	0.03	0.04	0.03	0.04
tracking	0.02	0.02	0.02	0.02	0.01	0.01
hadronization	0.01	0.01	0.01	0.01	0.01	0.01
MC nonclosure	0.01	0.02	0.03	0.05	0.08	0.12
matrix element	0.01	0.01	0.02	0.03	0.06	0.09
JES/JER	0.01	0.01	0.01	0.01	0.01	0.01
gluon reweight	0.01	0.01	0.01	0.01	0.01	0.01
Statistical	0.01	0.01	0.01	0.01	0.01	0.03
Total Uncertainty	0.23	0.24	0.24	0.26	0.28	0.35

Table 5.17 The gluon scale factor (nominal) and the difference between the nominal and systematic variation results for 80% gluon tag efficiency from N_{trk} tagger

	500-600	600-800	800-1000	1000-1200	1200-1500	1500-2000
nominal	0.98	0.97	0.95	0.93	0.89	0.85
parton shower	0.32	0.31	0.33	0.37	0.37	0.45
scale variation	0.07	0.07	0.05	0.07	0.07	0.05
splitting kernel	0.07	0.02	0.02	0.03	0.01	0.02
pdf weight	0.06	0.07	0.07	0.09	0.09	0.08
tracking	0.01	0.01	0.01	0.01	0.01	0.01
MC nonclosure	0.01	0.03	0.04	0.06	0.1	0.15
matrix element	0.01	0.01	0.02	0.04	0.07	0.11
hadronization	0.01	0.01	0.01	0.01	0.01	0.01
JES/JER	0.01	0.01	0.01	0.01	0.01	0.01
gluon reweight	0.01	0.01	0.01	0.01	0.01	0.01
Statistical	0.01	0.01	0.01	0.01	0.01	0.03
Total Uncertainty	0.34	0.33	0.34	0.39	0.41	0.49

The calibration of quark/gluon jets taggers

Table 5.18 The gluon scale factor (nominal) and the difference between the nominal and systematic variation results for 50% gluon tag efficiency from BDT tagger

	500-600	600-800	800-1000	1000-1200	1200-1500	1500-2000
nominal	1.0	0.99	0.98	0.96	0.94	0.92
parton shower	0.09	0.08	0.1	0.1	0.1	0.13
pdf weight	0.04	0.04	0.05	0.05	0.06	0.04
splitting kernel	0.03	0.02	0.02	0.02	0.01	0.02
scale variation	0.01	0.01	0.01	0.01	0.01	0.03
MC nonclosure	0.01	0.02	0.03	0.05	0.06	0.09
hadronization	0.01	0.01	0.01	0.01	0.01	0.01
tracking	0.01	0.01	0.01	0.01	0.01	0.01
matrix element	0.01	0.01	0.02	0.02	0.04	0.07
gluon reweight	0.01	0.01	0.01	0.01	0.01	0.01
JES/JER	0.01	0.01	0.01	0.01	0.01	0.01
Statistical	0.01	0.01	0.01	0.01	0.01	0.02
Total Uncertainty	0.11	0.1	0.11	0.13	0.14	0.18

Table 5.19 The gluon scale factor (nominal) and the difference between the nominal and systematic variation results for 60% gluon tag efficiency from BDT tagger

	500-600	600-800	800-1000	1000-1200	1200-1500	1500-2000
nominal	0.99	0.98	0.97	0.95	0.93	0.91
parton shower	0.11	0.12	0.13	0.13	0.14	0.17
pdf weight	0.05	0.05	0.05	0.06	0.06	0.06
splitting kernel	0.05	0.03	0.03	0.03	0.01	0.04
MC nonclosure	0.02	0.03	0.04	0.06	0.08	0.1
scale variation	0.02	0.02	0.02	0.02	0.02	0.05
hadronization	0.01	0.01	0.01	0.01	0.02	0.01
tracking	0.01	0.01	0.01	0.01	0.01	0.01
matrix element	0.01	0.01	0.02	0.03	0.04	0.08
gluon reweight	0.01	0.01	0.01	0.01	0.01	0.01
JES/JER	0.01	0.01	0.01	0.01	0.01	0.01
Statistical	0.01	0.01	0.01	0.01	0.01	0.02
Total Uncertainty	0.13	0.14	0.15	0.16	0.18	0.23

The calibration of quark/gluon jets taggers

Table 5.20 The gluon scale factor (nominal) and the difference between the nominal and systematic variation results for 70% gluon tag efficiency from BDT tagger

	500-600	600-800	800-1000	1000-1200	1200-1500	1500-2000
nominal	0.98	0.97	0.95	0.93	0.89	0.86
parton shower	0.15	0.15	0.17	0.17	0.17	0.21
splitting kernel	0.07	0.05	0.05	0.04	0.03	0.05
pdf weight	0.05	0.06	0.06	0.07	0.07	0.06
MC nonclosure	0.05	0.05	0.07	0.09	0.12	0.15
scale variation	0.03	0.04	0.03	0.04	0.04	0.07
hadronization	0.02	0.01	0.01	0.01	0.01	0.01
tracking	0.01	0.01	0.01	0.01	0.01	0.01
matrix element	0.01	0.01	0.02	0.03	0.05	0.08
JES/JER	0.01	0.01	0.01	0.01	0.01	0.01
gluon reweight	0.01	0.01	0.01	0.01	0.01	0.01
Statistical	0.01	0.01	0.01	0.01	0.01	0.02
Total Uncertainty	0.18	0.18	0.2	0.21	0.23	0.29

Table 5.21 The gluon scale factor (nominal) and the difference between the nominal and systematic variation results for 80% gluon tag efficiency from BDT tagger

	500-600	600-800	800-1000	1000-1200	1200-1500	1500-2000
nominal	0.96	0.95	0.93	0.9	0.85	0.81
parton shower	0.19	0.18	0.21	0.2	0.22	0.28
splitting kernel	0.09	0.07	0.06	0.06	0.05	0.07
MC nonclosure	0.08	0.09	0.1	0.12	0.17	0.21
pdf weight	0.06	0.06	0.07	0.08	0.08	0.06
scale variation	0.05	0.05	0.05	0.05	0.07	0.08
hadronization	0.02	0.01	0.01	0.01	0.01	0.01
tracking	0.01	0.01	0.01	0.01	0.01	0.01
matrix element	0.01	0.01	0.02	0.03	0.06	0.09
JES/JER	0.01	0.01	0.01	0.01	0.01	0.01
Statistical	0.01	0.01	0.01	0.01	0.01	0.03
gluon reweight	0.01	0.01	0.01	0.01	0.01	0.02
Total Uncertainty	0.23	0.23	0.25	0.26	0.31	0.38

1154 Figure 5.46 to Figure 5.49 show the leading uncertainties with SFs for both tagger.
1155 The SFs for quark-jets and gluon-jets corresponding to the 50% quark-jets efficiency
1156 working point (WP) fall within the range of 0.92 to 1.02, while being subject to an ag-
1157 gregate systematic uncertainty of approximately 20%. Among the various sources of
1158 systematic uncertainty, theoretical modelling emerges as the dominant factor contribut-
1159 ing to the total uncertainty.

1160 To ascertain the robustness of the findings, tests are conducted to assess the stabili-
1161 ty of results across different regions of jet $|\eta|$. The SF measurements are recomputed
1162 through the normalization of jet $|\eta|$ in the quark-/gluon-enriched subsamples. The al-
1163 ternate results obtained in this manner are determined to be consistent with the nominal
1164 outcome, falling within the full range of reported uncertainties.

1165 Given the variations in the usage of different MC samples, a MC-to-MC SF is com-
1166 puted. This involves employing each alternative MC sample while treating the PYTHIA MC
1167 samples as pseudodata. This approach accommodates discrepancies arising from mod-
1168 elling difference between the PYTHIA and alternative MC samples. The MC-to-MC SFs
1169 for both jet taggers at each WP are shown in Figure 5.50 to Figure 5.53. Notably, there
1170 exists a large difference in gluon modelling between the HERWIG Dipole parton shower
1171 MC and the PYTHIA MC. This discrepancy is reflected in the relatively significant MC-
1172 to-MC SF, indicating substantial differences between these models.

The calibration of quark/gluon jets taggers

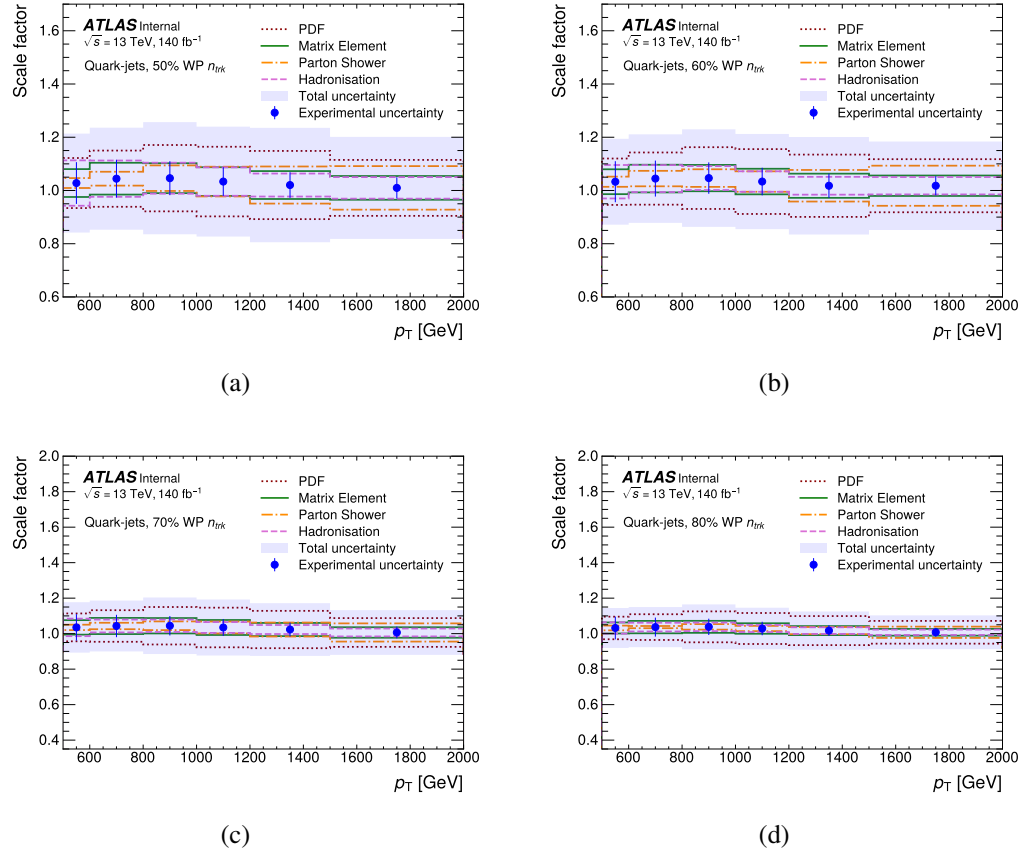


Figure 5.46 The SF with total and leading systematic uncertainty on the jet tagging variable N_{trk} obtained by PYTHIA 8 MCs as a function of jet p_T for quark-jets at each WP.

The calibration of quark/gluon jets taggers

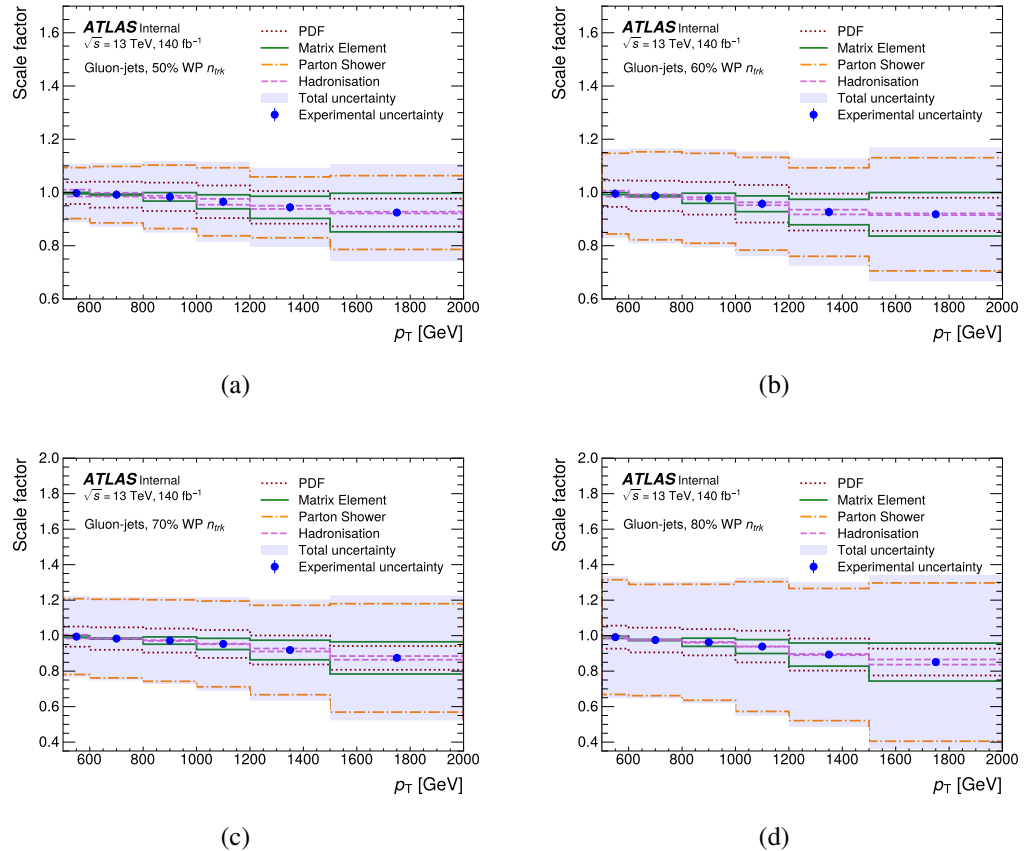


Figure 5.47 The SF with total and leading systematic uncertainty on the jet tagging variable N_{trk} obtained by PYTHIA 8 MCs as a function of jet p_T for gluon-jets at each WP.

The calibration of quark/gluon jets taggers

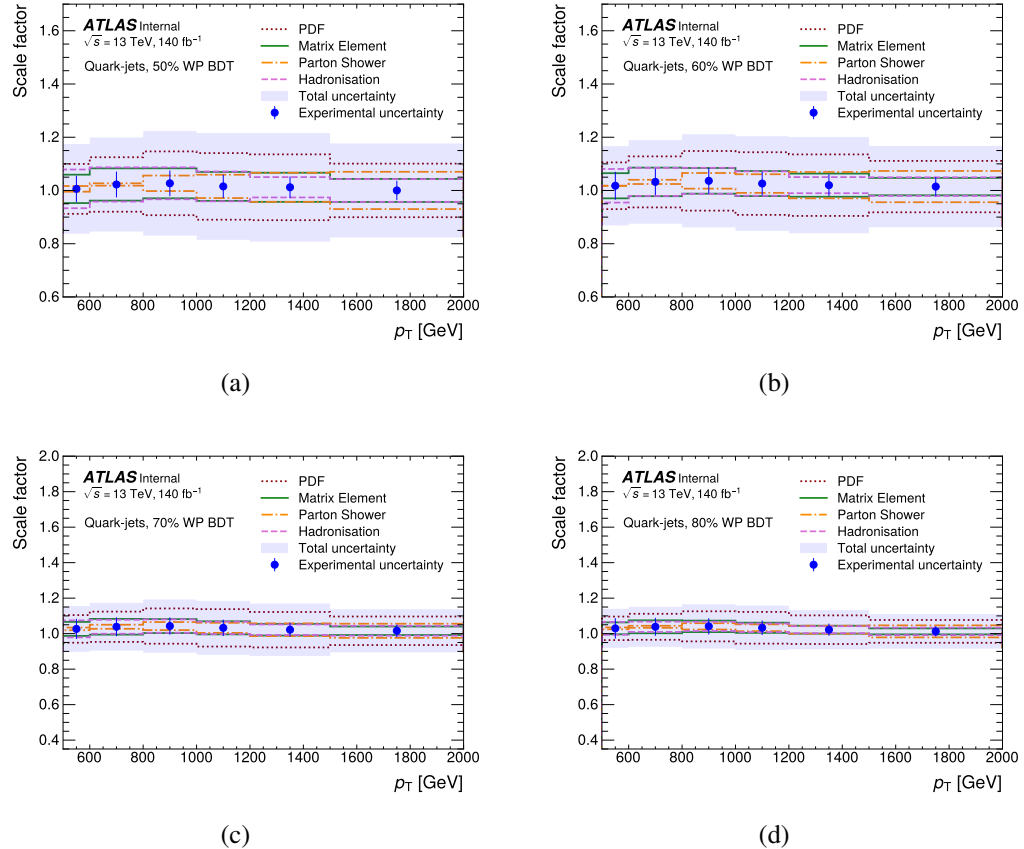


Figure 5.48 The SF with total and leading systematic uncertainty on the jet tagging variable BDT obtained by PYTHIA 8 MCs as a function of jet p_T for quark-jets at each WP.

The calibration of quark/gluon jets taggers

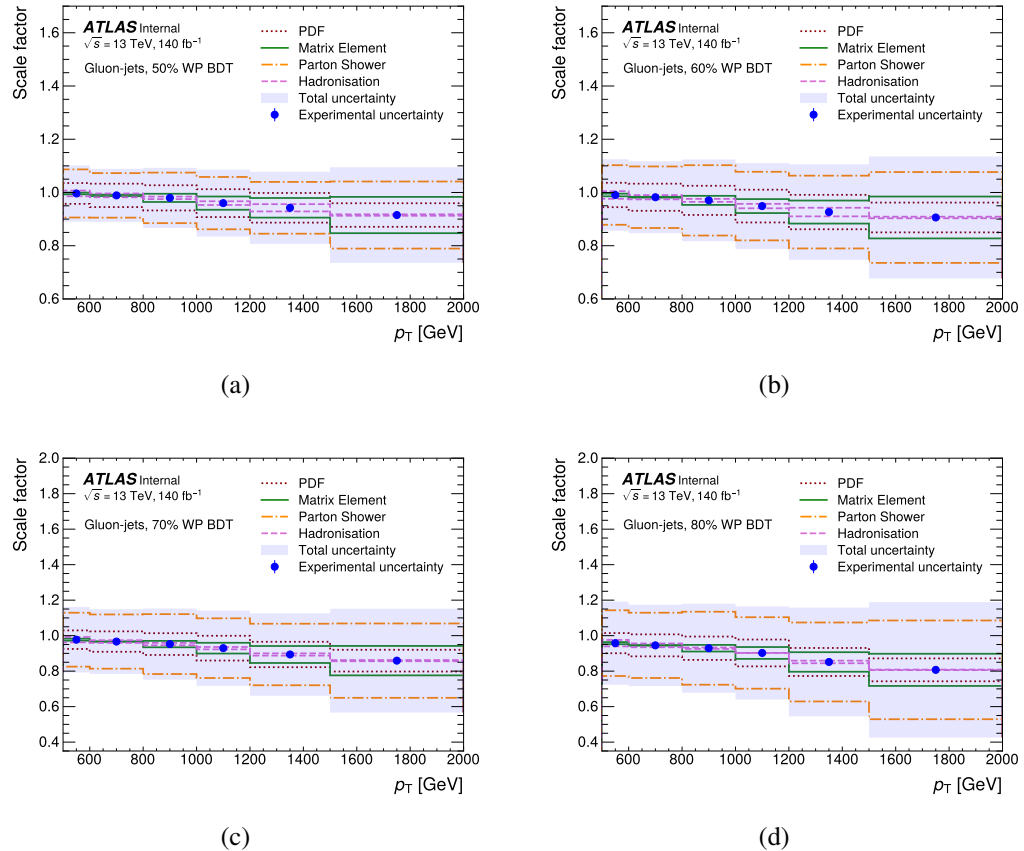


Figure 5.49 The SF with total and leading systematic uncertainty on the jet tagging variable BDT obtained by PYTHIA 8 MCs as a function of jet p_T for gluon-jets at each WP.

The calibration of quark/gluon jets taggers

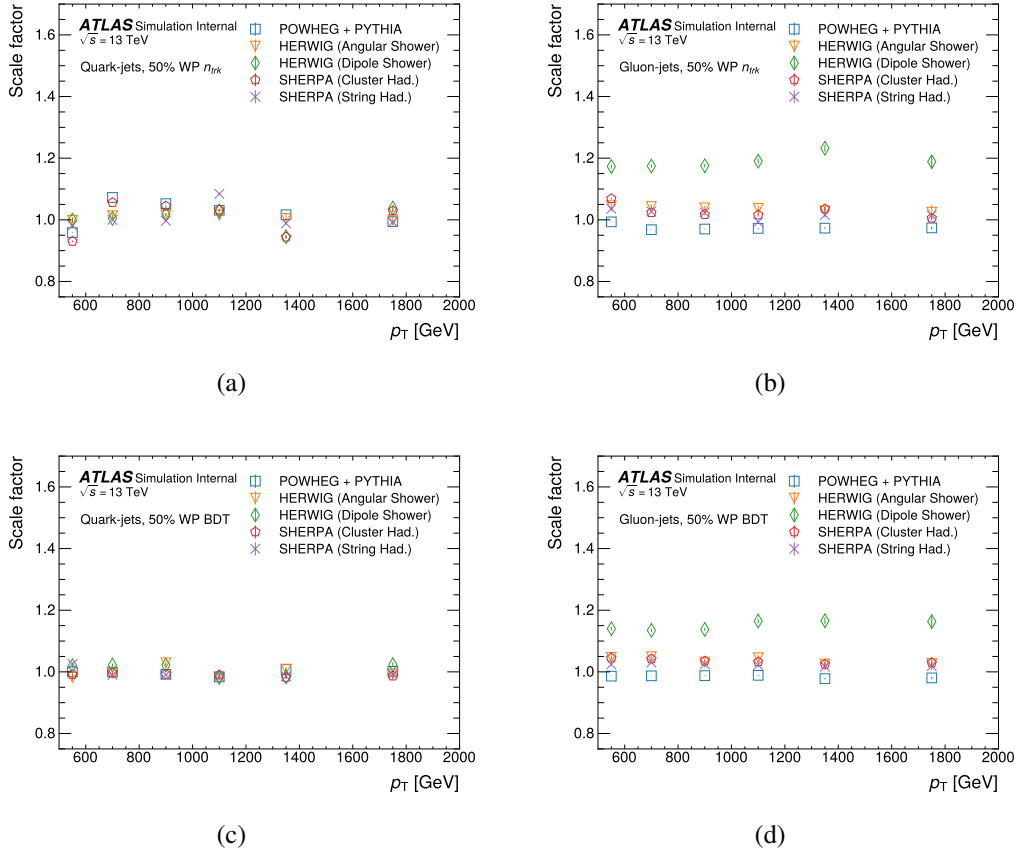


Figure 5.50 The MC-to-MC SF of the N_{trk} , (a) and (b), and BDT, (c) and (d), as a function of jet p_T for quark-jets (left) and gluon-jets (right) at the 50% WP. The vertical error bars show the statistical uncertainty.

The calibration of quark/gluon jets taggers

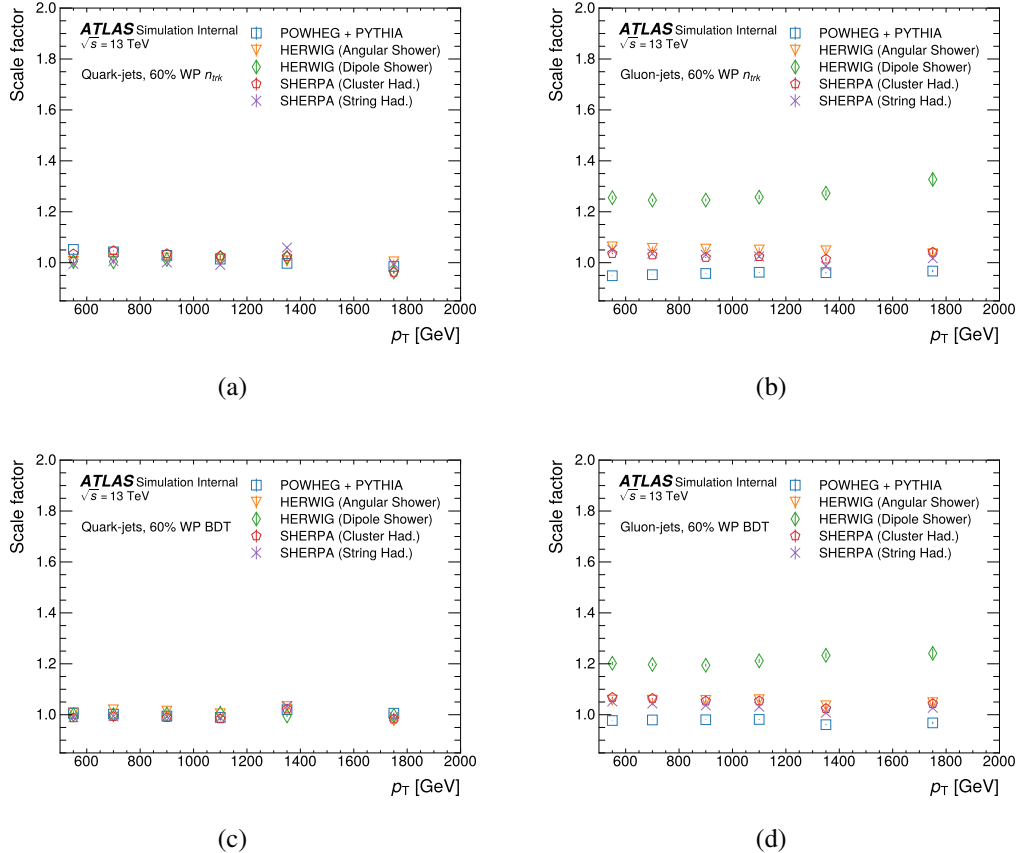


Figure 5.51 The MC-to-MC SF of the N_{trk} , (a) and (b), and BDT, (c) and (d), as a function of jet p_T for quark-jets (left) and gluon-jets (right) at the 60% WP. The vertical error bars show the statistical uncertainty.

The calibration of quark/gluon jets taggers

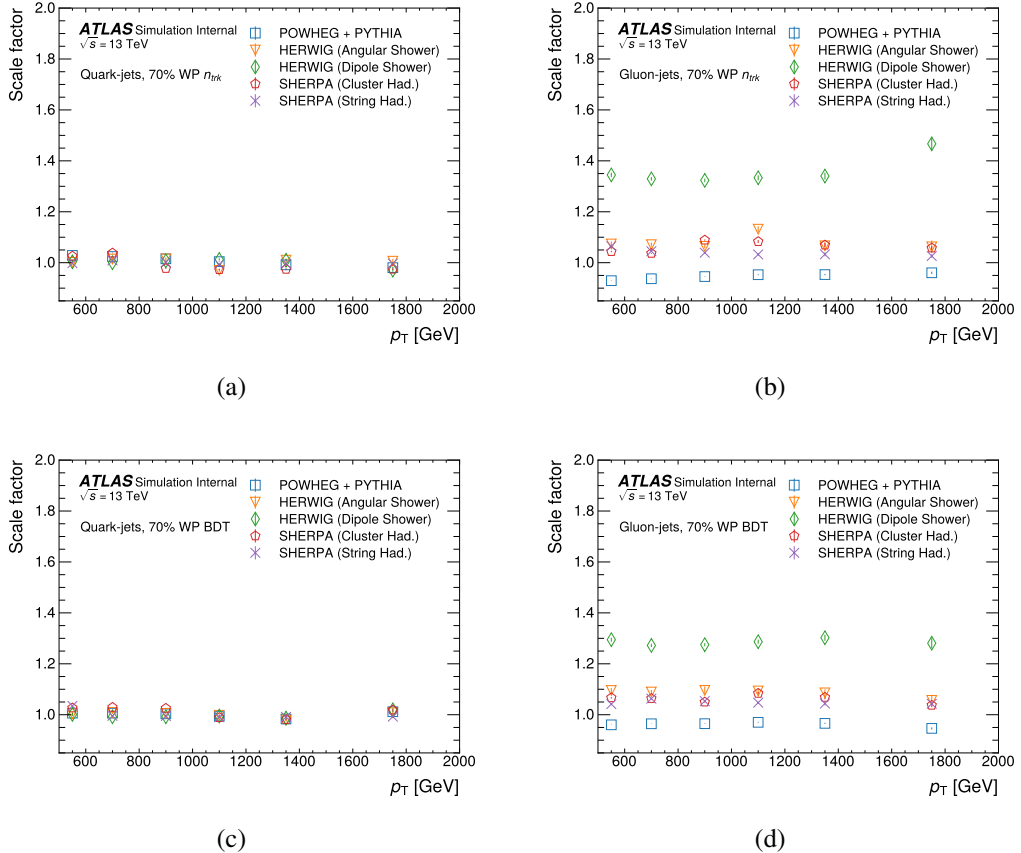


Figure 5.52 The MC-to-MC SF of the N_{trk} , (a) and (b), and BDT, (c) and (d), as a function of jet p_T for quark-jets (left) and gluon-jets (right) at the 70% WP. The vertical error bars show the statistical uncertainty.

The calibration of quark/gluon jets taggers

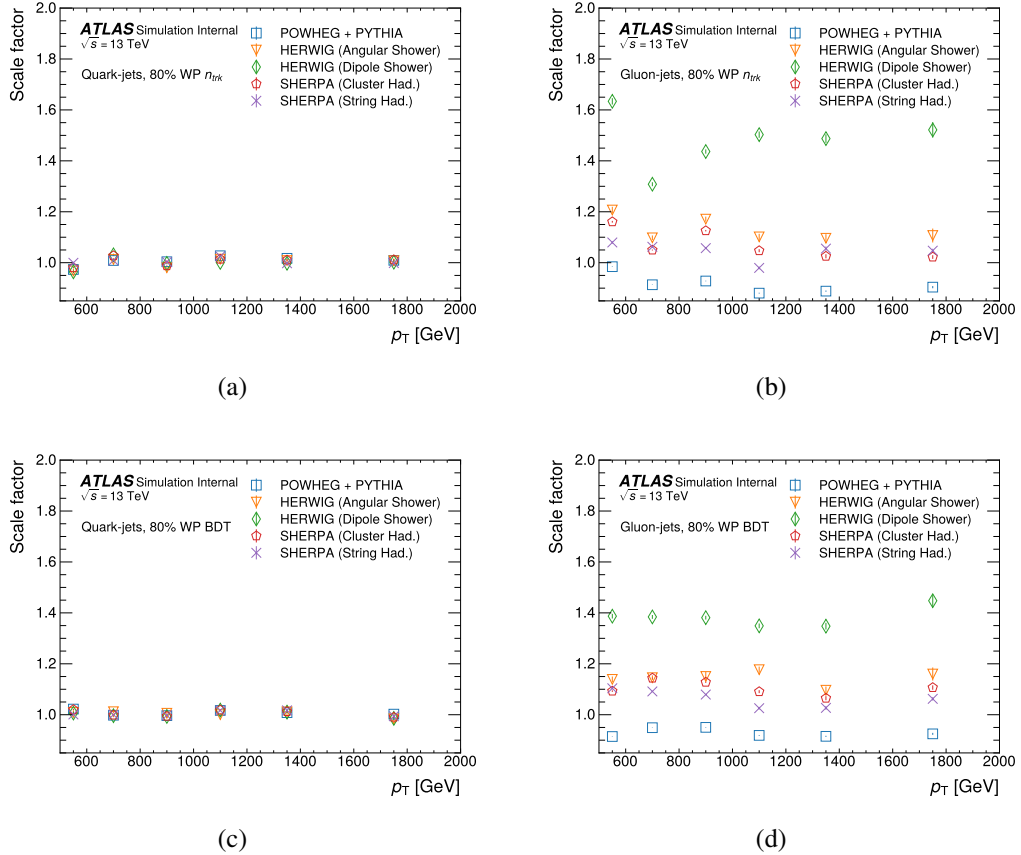


Figure 5.53 The MC-to-MC SF of the N_{trk} , (a) and (b), and BDT, (c) and (d), as a function of jet p_T for quark-jets (left) and gluon-jets (right) at the 80% WP. The vertical error bars show the statistical uncertainty.

1173 **5.12 Conclusions**

1174 The analysis focuses on evaluating the performance of jet taggers for quark- and
1175 gluon-jets using a dataset of 140 fb^{-1} obtained from pp collisions at a centre-of-mass en-
1176 ergy of $\sqrt{s} = 13 \text{ TeV}$, gathered by the ATLAS detector at the LHC. This study leverages
1177 the extensive dataset recorded between 2015 and 2018 to extend the taggers' applicabil-
1178 ity to high-energy jets. Two distinct jet tagging methods are explored: a tagger centred
1179 on the charged-particle jet constituent multiplicity (N_{trk}), and a BDT-based tagger, which
1180 integrates various individual jet substructure observables.

1181 The matrix method is adopted to estimate the distribution shapes of the tagging
1182 variables for quark- and gluon-jets. This entails combining information from samples
1183 enriched with quark- and gluon-jets, acquired from a selection of dijet events charac-
1184 terized by jet p_{T} ranging from 500 GeV to 2 TeV. The considered variables exhibit a
1185 satisfactory agreement with the MC simulations, with discrepancies relative to data mea-
1186 surements being less than 25% across various defined regions.

1187 The BDT-tagger demonstrates superior performance over the N_{trk} -only tagger in
1188 distinguishing quark-jets from gluon-jets within the jet p_{T} range of 500 GeV to 1200
1189 GeV. Above this range, the performance of the two taggers becomes comparable.

1190 The evaluation of tagger performance differences between data and MC samples
1191 is facilitated through the data-to-MC SFs. These factors are measured across varying
1192 jet- p_{T} intervals, exhibiting a range from 0.92 to 1.02, with a cumulative uncertainty of
1193 approximately 20%. The primary contributor to this uncertainty stems from divergent
1194 modelling choices within MC simulations, constituting approximately 18% for both tag-
1195 gers. To account for variations between different MC generators, MC-to-MC SFs are
1196 also presented, ranging from 0.9 to 1.1 for the majority of MC samples.

1197 The q/g taggers developed in this study and the associated measurement of their SFs
1198 hold relevance for various analyses. These applications encompass SM measurements
1199 that rely on accurate jet origin identification, as well as BSM physics searches that can
1200 capitalize on heightened sensitivity to the presence of new particles.

1201 6 Search for new phenomena in dijet events

1202 As described in Section 2, the heavy resonance predicted by many BSM play a key role
1203 in understanding many fundamental phenomena. The narrow heavy resonance which
1204 decays into two gluons final state at the LHC, appears to be two hadronic jets in the
1205 detector. Produced by the QCD processes, the dijet events have a smoothly falling dis-
1206 tribution of the invariant mass m_{jj} , whereas two jets appear to be a resonance in the
1207 m_{jj} spectrum. As a result, searches for dijet resonance are one of the flagship exotics
1208 analyses in ATLAS.

1209 Besides, on the assumption that the resonant sample can be classified according to
1210 the type of parton that initiated the jets, the sensitivity of searches for new resonance
1211 can be improved by identifying the types of partons through which the potentially new
1212 particle interact. One of simplest examples of such tagging is gluon-tagging one or more
1213 of the jets. The jet tagging procedure based on the number of charged tracks with trans-
1214 verse momentum p_T above 500 GeV is described in Section 5. The m_{jj} spectrum of
1215 background is estimated from the data, which is used for the search in three categories:
1216 inclusive, single-gluon, and double-gluon tagged dijet systems. The inclusive m_{jj} spec-
1217 trum is thus considered as control region for quark/gluon studies.

1218 This chapter describes searches for new heavy particles decay in dijet final state
1219 as originating from gluons or quarks, a technique of quark/gluon tagging is employed
1220 to enhance the sensitivity to the results. The search performed uses full Run 2 data
1221 at $\sqrt{s} = 13$ TeV, with higher integrated luminosity compared to previous one (Run 1),
1222 significantly improvements in the understanding of systematic uncertainties are expected.
1223 On the other hand, cross section upper limits will be set if no significantly resonances
1224 are observed.

1225 The simplified procedures in this analysis is performed as following:

- 1226 • Search for high-mass resonances in the untagged (inclusive), single-gluon tagged,
1227 and two-gluon tagged categories with dijet events.
- 1228 • If significant resonances are found, claim something interesting, else the upper
1229 limits are set.
- 1230 • Model independent upper-limits are set on resonance cross sections in inclusive,
1231 single-gluon tagged, and two-gluon tagged categories.

- 1232 • For the specific resonance model, set lower limits on the relevant scales in inclu-
 1233 sive, single-gluon tagged, and two-gluon tagged categories. dijet systems.

1234 **6.1 Monte Carlo models**

1235 . This section outlines benchmark models for both background from the QCD and
 1236 for new physics signals that encapsulated in the models chosen: H' , Strings, and QBH.
 1237 Full Run 2 data are used to produce EXOT2 skimmed samples used in this analysis.

1238 **6.1.1 QCD background**

1239 QCD processes from the MC are simulated at LO and NLO in SM perturbative
 1240 theory. Due to the large range in cross section of QCD sample, the samples are thus
 1241 sliced based on the leading jet p_T , to obtain comparable statistical precision across the
 1242 jet p_T range of interest.

1243 **6.1.2 H'**

1244 This analysis performs a model-independent search for two-gluon resonances at
 1245 high m_{jj} spectrum, as the CCD background is dominated by valence quark scattering,
 1246 gluon tagging in this case could be effective.

1247 The simulated SU(3) singlet scalar that decay via PYTHIA 8 with the A14 set of
 1248 tuned parameters is used in this analysis¹. The HiggsBSM:gg2H2, where set the singlet
 1249 scalar as H2 particle and has Particle Data Group ID 35. Such H2 particle is set to
 1250 decay to gluons and has a narrow resonances width of 0.1 GeV as the physical width is
 1251 model-dependent but constrained by the detector resolution.

1252 The benchmark signals used vary in their underlying physics motivation, but also
 1253 in the resulting shape of the signal m_{jj} distribution. The peaks of signal shape are set for
 1254 various mass points as shown in Figure 6.54, the distributions are normalized to unity
 1255 and thus the differences in peak amplitudes are not the changes in cross section.

¹See <https://its.cern.ch/jira/browse/ATLMCPROD-6155>.

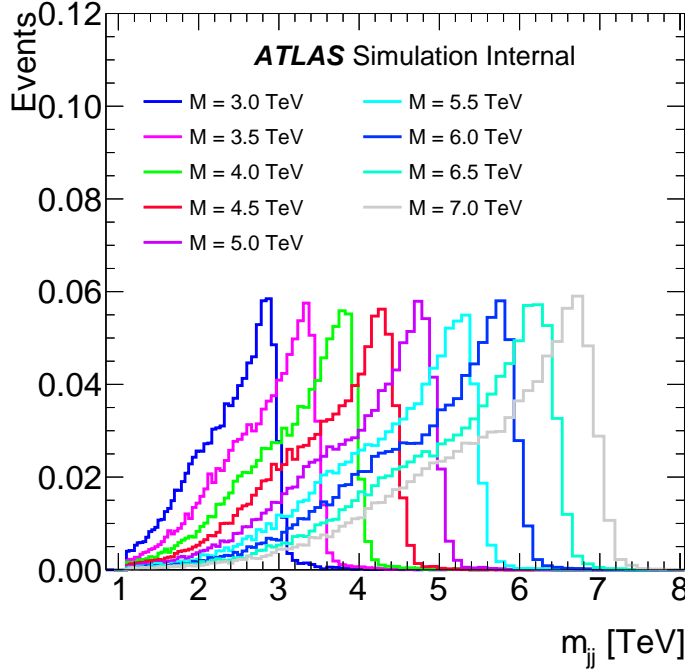


Figure 6.54 Signal shapes for the H' signal at different mass points.

6.1.3 Strings

As the SM has lots of well known problems such as the quadratically divergent corrections to the Higgs self-energy, supersymmetry theory offers a solution to it by fine-tuning the cancellation. The superstring theory, additionl to the supersymmetry, can perform as a framework that unify theories from SM at TeV-scale to quantum gravity at Planck-scale .

The fundamental string scale is chosen to be within TeV scale, dontes as string mass-scale M_s . The string resonances could happen at masses $m_n = \sqrt{n}M_s$, for $n = 1, 2, 3, \dots$, where the resonance consist of the Regge excitations of quark, gluon, as well as the colour singlet that lives on the QCD stack of branes. In total, five string scales M_s range from 7.0 TeV to 9.0 TeV, in steps of 0.5 TeV are generated for string-resonance samples. The lower limits of mass M_{\min} provided in the generator are shown in Table 6.22, together with the resulting cross section of the string samples.

As the string resonances have long Breit-Wigner tails, the PDFs at low- x (low mass) can significantly enhance the tail. In this study, the low-mass tail is truncated since only narrow-resonance structure in m_{jj} spectrum is interesting to this analysis. In the range $7.0 \leq M_s \leq 8.0$ TeV, the truncation is done at the minimum value in the differential cross

M_s [TeV]	M_{\min} [TeV]	Cross section [fb]
7.0	6.06	7.09E+0
7.5	6.60	1.86E+0
8.0	7.14	4.56E-1
8.5	7.60	1.00E-1
9.0	8.05	1.99E-2

Table 6.22 MC string-resonance samples with string scale M_s , minimum mass M_{\min} , and cross section.

section on the lower-mass side of the M_s peak, results in around 95% of the area under the Breit-Wigner curve. In the range $7.0 \leq M_s \leq 8.0$ TeV, the truncation is done at a lower-mass point that covers 95% of the area under the Breit-Wigner curve.

The distribution of signal peak at different mass points is shown in Figure 6.55, the distributions are normalized to unity and thus the differences in peak amplitudes are not the changes in cross section.

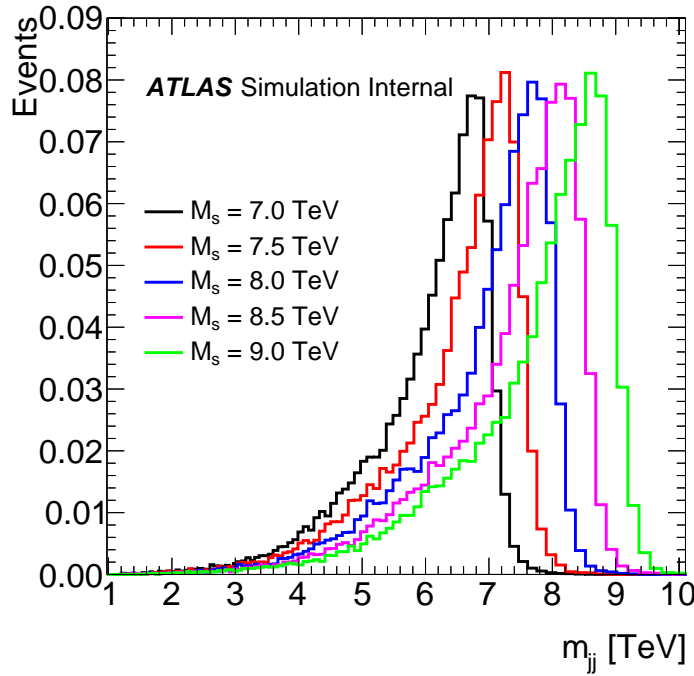


Figure 6.55 Signal shapes for the String signal.

There are five possible $2 \rightarrow 2$ subprocesses from string resonances are simulated.

1280 with the cross section for each subprocess vary as a function of M_s shown in Table 6.23.
 1281 The dominate subprocess across the M_s values is considered to be $gq \rightarrow gq$, which con-
 1282 tributes around 81-87% of the total cross section. The rest of subprocesses: $qq \rightarrow qq$,
 1283 $\bar{q}\bar{q} \rightarrow \bar{q}\bar{q}$, and $q\bar{q} \rightarrow q\bar{q}$ are model dependent and thus do not included in this analysis.

Subprocess	M_s [TeV]				
	7.0	7.5	8.0	8.5	9.0
$gg \rightarrow gg$	11.4%	9.5%	8.2%	7.2%	5.1%
$gg \rightarrow q\bar{q}$	0.3%	0.3%	0.2%	0.2%	0.2%
$gq \rightarrow gq$	81.4%	83.1%	84.6%	85.5%	87.6%
$g\bar{q} \rightarrow g\bar{q}$	0.7%	0.6%	0.5%	0.5%	0.5%
$q\bar{q} \rightarrow gg$	6.3%	6.5%	6.5%	6.5%	6.7%

Table 6.23 String-resonance subprocesses and their relative contributions to the total cross section at each string scales M_s . The statistics are based on samples of 66000 events.

1284 For generating string samples, the MC event generator STRINGS 1.00 [?] with in-
 1285 terfaced to PYTHIA 8.240 for parton shower modelling is used, together with the A14
 1286 tune. The CTEQ6L1 [?] PDF set at the LO is used for the parton shower and the hard-
 1287 scattering process. The decaying processes is simulated using the EvtGen 1.6.0 program.

1288 The effect from pile-up is simulated by overlaying the MC inelastic pp events gen-
 1289 erated with PYTHIA 8.186 with a PDF set of NNPDF2.3 at LO and the A3 tune over the
 1290 original hard-scattering events.

1291 6.1.4 Quantum Black Holes

1292 In our study, we employ the QBH model for the purpose of comparing limits with
 1293 the previous iteration of the analysis. The feasibility of producing QBHs at the LHC is
 1294 contingent upon the presence of sufficiently large extra dimensions within the universe.
 1295 This model posits that the energy scale of quantum gravity M_D , at which QBHs are gen-
 1296 erated, diminishes as the number of these large extra dimensions, denoted as n , increases.
 1297 Consequently, a larger n permits lower mass scales at which QBHs can be formed.

1298 Two-body isotropic final state is expected by the QBH decay at the LHC, where
 1299 the M_D energy threshold could be reached. Therefore the quantum gravitational effects
 1300 can be probed by searches on m_{jj} spectrum. To simulate events involving quantum black
 1301 holes with $n = 6$, we utilize the BlackMax [?] Monte Carlo (MC) generator. This MC

Search for new phenomena in dijet events

¹³⁰² generator facilitates the simulation of QBH events within the $n = 6$ framework..

1303 6.2 Events selections

1304 The MC and data events are divided into three categories to perform the search:
 1305 the untagged dijet invariant mass spectrum, one-gluon tagged spectrum, and two-gluon
 1306 tagged spectrum. The evidence of BSM resonances would appear as peaks in the m_{jj}
 1307 spectrum formed by two highest p_T jets in the events. A series of specific cuts is applied
 1308 to improved the sensitivity of the searches.

1309 6.2.1 Observables and Kinematic Variables

1310 The predominant source of dijet events in the SM is two-to-two scattering though
 1311 the QCD processes. This search exams two key properties of the QCD background:

- 1312 • The background at high m_{jj} appears as a smooth and continuously falling spec-
 1313 trum.
- 1314 • The background at high energy strongly peaks in the forward region as a result
 1315 of Rutherford t - and u -channel poles in the cross sections for certain scattering
 1316 processes [?].

1317 Resonances of interest have $\cos \theta$ distributions in the detector, which in contrast to
 1318 Rutherford scattering, are either isotropic or have polynomial behaviour in $\cos \theta$ ², thus
 1319 a angular distribution appears. This search therefore defines a y^* to indicate the angle
 1320 separation of the jets in the selected events:

$$y^* = (y_1 - y_2)/2 \quad (6.1)$$

1321 to improve the sensitivity to higher energies where new phenomena are expected. The
 1322 variables y_1, y_2 represent the rapidity of the leading and subleading jet. The value of the
 1323 y^* cut on events is optimized for each signal as discussed in Section .6.4.1.

1324 In this analysis, jets are reconstructed with the anti- k_t algorithm with a radius pa-
 1325 rameter $R = 0.4$, as implemented in the FASTJET package [?]. The EMTopo jets, recon-
 1326 structed from topological clusters via procedures described in Section .4.1, are used. The
 1327 standard *Loose* cut is applied to jet quality as well as jet cleaning. The summarized jet
 1328 criteria are shown in Table 6.24.

²See Ref. [?] p15 for a summary.

Parameter / Observable	Requirement
Algorithm	anti- k_t
R-parameter	0.4
Input Constituent	EMTopo
p_T	>150 GeV
$ \eta $	<2.1

Table 6.24 Jet selection criteria used in this analysis.

6.2.2 Baseline selection

The triggers used in this analysis is HLT_j420. Besides, two single-jet trigger HLT_j225_gsc420_boffperf_split is also used as the unprescaled trigger for full Run 2 data. Both triggers have the threshold of $p_T > 420$ GeV of the jets, while the GSC is applied to the HLT_j225_gsc420_boffperf_split to the trigger turn-on improvement. A turn-on based on the m_{jj} spectrum is found to be much powerful than the cut requirement of the leading jet p_T , where the m_{jj} cut imposes a soft cut on the leading and subleading jet, respectively. More details are shown in Section 6.4.2.

The baseline event selection is applied for all categories. The GRL and various flags that indicate the status of detector when taking data are provided by the ATLAS Data Quality (DQ) group, are applied to ensure the data integrity. Primary vertex requirement is also included to ensure good quality jets. The

- All jets with $p_T > 150$ GeV pass *Loose* cleaning cuts
- Passes the lowest unprescaled single-jet trigger: HLT_j420
- Jet multiplicity ≥ 2
- Leading jet $p_T > 380$ GeV and subbeading jet $p_T > 150$ GeV
- Leading jet $|\eta| < 2.1$ and subbeading jet $|\eta| < 2.1$
- $|\Delta\phi|$ between two jets: $|\Delta\phi| > 1.0$
- $m_{jj} > 1100$ GeV

Additional kinematic criteria are applied according to the distributions of signals, in order to optimize the search potential, are then discussed in Section 6.4.1.

1350 6.3 Quark-Gluon Sample Selection

1351 . The sensitivity of the search on the resonant is expected to increase by distin-
 1352 guishing the type of parton that initiated the jets. The parton types of dijet events as a
 1353 function of m_{jj} from the MC with a PYTHIA8.186 at LO NNPDF2.3 PDFs is shown in
 1354 Figure 6.56, suggesting that the search for new resonance can be improved by tagging
 1355 quark and gluon jets.

1356 In this section we present the search for new particles using the full Run 2 $\sqrt{s} =$
 1357 13 TeV dataset with quark and gluon tagging method.

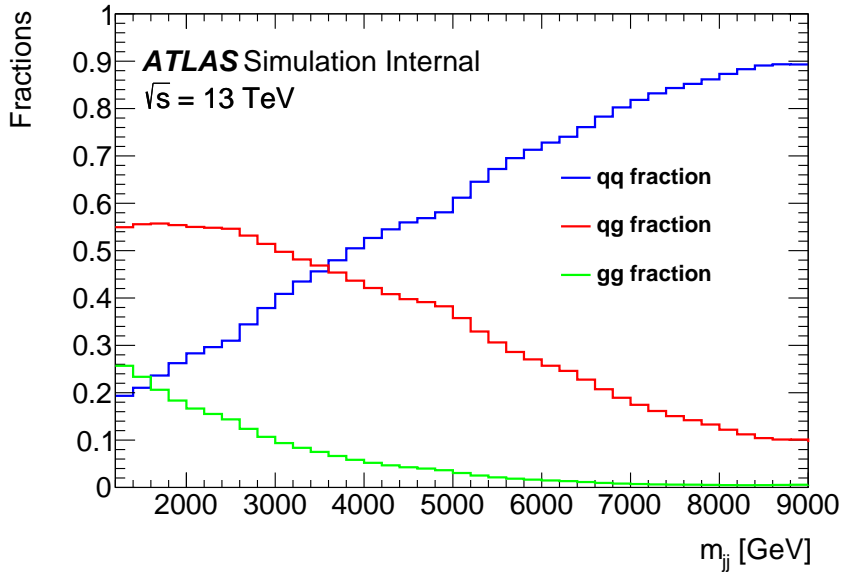


Figure 6.56 The fraction of dijet events that are initiated by quark-quark events (blue), quark-gluon events (green) and gluon-gluon events (red) in simulated data.

1358 Previous study in ATLAS has shown that the jets can be tagged quark or gluon
 1359 jets based on the number of charged tracks associated with the jets with p_T above 500
 1360 MeV. Samples with enhanced fractions of quark or gluon initiated jets can be created by
 1361 using a selection based on the charged-particle constituent multiplicity N_{trk} . As shown in
 1362 Figure 6.57, where PYTHIA 8 generator is used for MC to ensure a good agreement with
 1363 the distribution of N_{trk} in data within the ID acceptance $|\eta| < 2.1$.

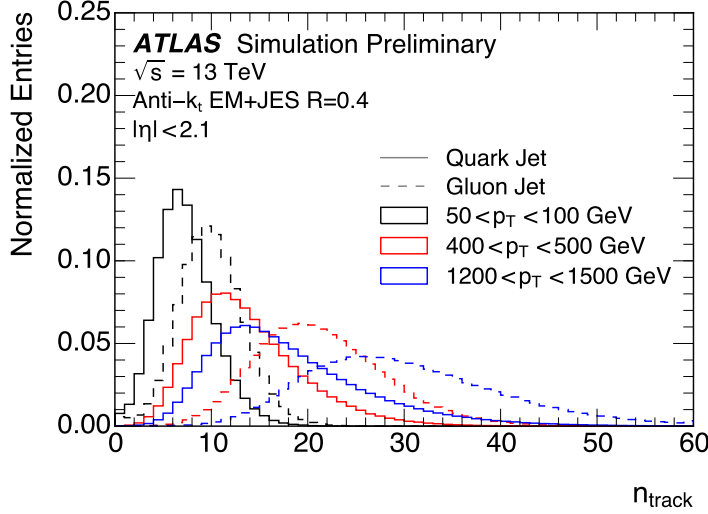


Figure 6.57 Distribution of the jet reconstructed track multiplicity (N_{trk}) in different p_T ranges with the PYTHIA 8 MC samples and processes with a full simulation of the ATLAS detector. Tracks are required to have $p_T > 500 \text{ MeV}$ and pass quality criteria described in Ref. [?].

1364 **6.3.1 Expected Signal Significance**

1365 The shape of m_{jj} from QCD is complex and rapidly changing according to the frac-
 1366 tions of events that originate from quark-quark, quark-gluon and gluon-gluon scattering.
 1367 The QCD background is presented in Section 6.1.1. The MC simulated signals and back-
 1368 ground is thus used for estimating the expected signal significance.

1369 **6.3.1.1 Resonances that decay to quark-quark**

1370 The statistical significance associated with signals decaying into quark-antiquark pairs
 1371 is assessed using Z' models using

$$S = N_S \sum_i \frac{f_{qq,i} \epsilon_{qQ}^2 + f_{qg,i} \epsilon_{qQ} \epsilon_{gQ} + f_{gg,i} \epsilon_{gQ}^2}{\sqrt{B_{qq,i} \epsilon_{qQ}^2 + B_{qg,i} \epsilon_{qQ} \epsilon_{gQ} + B_{gg,i} \epsilon_{gQ}^2}} \quad (6.2)$$

1372 where N_S is the number of signal events, $f_{qq,i}$ is fraction of signal events that result in the
 1373 two highest jets that were initiated by quarks in bin i ($f_{qg,i}$ are quark-gluon jets, and $f_{gg,i}$
 1374 is two gluon jets), ϵ_{qQ} is the efficiency of a quark initiated jet passing the quark selection
 1375 criteria, ϵ_{gQ} is the efficiency of a gluon initiated jet passing the quark selection criteria,
 1376 and $B_{xx,i}$ is the expected number of background events with quark-quark, quark-gluon or
 1377 gluon-gluon initiated jets.

1378 The statistical significance is computed for Z' particles mass values within the range
 1379 of 1500 to 4000 GeV, and for quark-jet selection efficiencies ranging from 30% to 90%.
 1380 The obtained significance values are presented in Figure 6.58. The depicted results il-
 1381 lustrate a trend of diminishing significance when any quark-selection criteria is imposed
 1382 on the data. This decline in significance can be attributed to the dominant presence of
 1383 quark-quark events within the data, where the selection process concurrently diminishes
 1384 both background and signal contributions to a comparable extent.

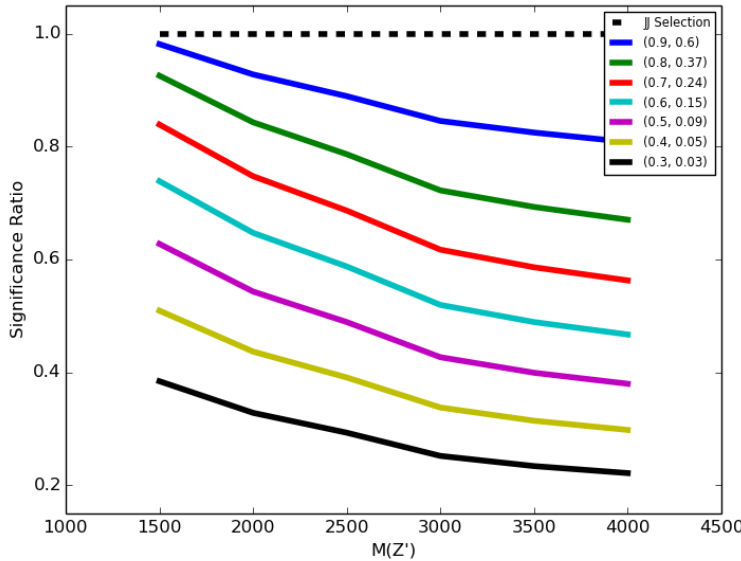


Figure 6.58 The significance for observing a Z' with masses from 1500 to 4000 GeV for ϵ_{qQ} ranging from 90 to 30% compared to the significance calculated with no quark selection applied. The key gives pairs of efficiencies ($\epsilon_{qQ}, \epsilon_{gQ}$).

1385 6.3.1.2 Signals that decay to gluon-gluon

1386 The significance for signals that decay to a gluon-gluon pair are using H' models,
 1387 estimated by:

$$S = N_S \sum_i \frac{f_{qq,i} \epsilon_{qG}^2 + f_{qg,i} \epsilon_{qG} \epsilon_{gG} + f_{gg,i} \epsilon_{gG}^2}{\sqrt{B_{qq,i} \epsilon_{qG}^2 + B_{qg,i} \epsilon_{qG} \epsilon_{gG} + B_{gg,i} \epsilon_{gG}^2}} \quad (6.3)$$

1388 where ϵ_{qG} is the efficiency of a quark initiated jet passing the gluon selection criteria, ϵ_{gG}
 1389 is the efficiency of a gluon initiated jet passing the gluon selection criteria.

1390 The computation of significance involves the utilization of simulated H' signals,
 1391 with masses ranging from 2000 to 7000 GeV. The efficiencies of gluon tagged are varied

across from 60% to 90%. The resulting significances, depicted as functions of H' masses, are presented in Figure 6.59. The observed trend reveals a gradual increase in significance, with values ascending from approximately 1.2 at 2 TeV to around 1.6 at 7 TeV. Notably, the most substantial enhancements occur at a gluon efficiency of 75%.

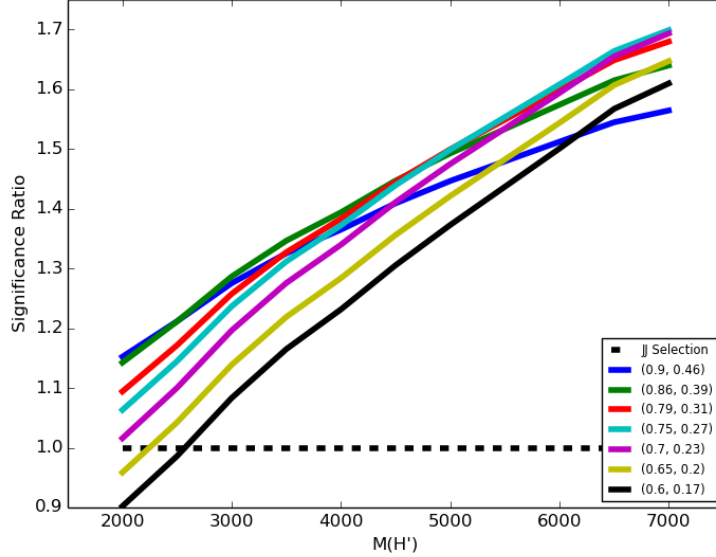


Figure 6.59 The significance for observing a H' with masses from 2000 to 7000 GeV for ϵ_{gG} ranging from 90 to 60% compared to the significance calculated with no gluon selection applied. The key gives pairs of efficiencies ($\epsilon_{gG}, \epsilon_{qG}$).

6.3.1.3 Signals that decay to quark-gluon

Calculating the significance for signals involving quark-gluon decays, such as string decays, poses increased complexity due to the potential overlap in the selection criteria between decaying jets that satisfy both quark and gluon criteria. In this context, it becomes imperative to establish distinct efficiencies exclusively tailored for quark- and gluon-jets. Thus the efficiencies are needed to be defined exclusively for quark- and gluon-jets.

The efficiencies for quark-jets are defined as:

- ϵ_{qQ} The efficiency that a quark-jet is identified only as a quark-jet.
- ϵ_{qQG} The efficiency that a quark-jet is identified as a quark- and a gluon-jet.
- ϵ_{qG} The efficiency that a quark-jet is identified only as a gluon-jet.

¹⁴⁰⁷ where $\epsilon_{qQ} + \epsilon_{qQG} + \epsilon_{qG} = 1$.

¹⁴⁰⁸ Another set of efficiencies that is measured for gluon-jets are:

¹⁴⁰⁹ • ϵ_{gQ} The efficiency that a gluon-jet is identified only as a quark-jet.

¹⁴¹⁰ • ϵ_{gQG} The efficiency that a gluon-jet is identified as a quark- and a gluon-jet.

¹⁴¹¹ • ϵ_{gG} The efficiency that a gluon-jet is identified only as a gluon-jet.

The probability of truth pairs of quark-quark (p_{qq}), quark-gluon (p_{qg}) and gluon-gluon (p_{gg}) events that passing the quark-gluon tagging selection criteria are given by:

$$p_{qq} = 2\epsilon_{qQ}\epsilon_{qG} + \epsilon_{qQG}(\epsilon_{qQ} + \epsilon_{qG}) + \epsilon_{qQG}\epsilon_{qQG} \quad (6.4)$$

$$p_{gg} = 2\epsilon_{gQ}\epsilon_{gG} + \epsilon_{gQG}(\epsilon_{gQ} + \epsilon_{gG}) + \epsilon_{gQG}\epsilon_{gQG} \quad (6.5)$$

$$p_{qg} = \epsilon_{qQ}\epsilon_{gG} + \epsilon_{gQ}\epsilon_{qG} + \epsilon_{qQG}(\epsilon_{gQ} + \epsilon_{gG}) + \epsilon_{gQG}(\epsilon_{qQ} + \epsilon_{qG}) + \epsilon_{gQG}\epsilon_{gQG} \quad (6.6)$$

¹⁴¹² the related significance is then defined as:

$$S = N_S \sum_i \frac{f_{qq,i}p_{qq} + f_{qg,i}p_{qg} + f_{gg,i}p_{gg}}{\sqrt{B_{qq,i}p_{qq} + B_{qg,i}p_{qg} + B_{gg,i}p_{gg}}}. \quad (6.7)$$

¹⁴¹³ No obvious benefit is observed after applied a quark selection with selection ef-
¹⁴¹⁴ ficiencies from 30 to 100%. A small but significant improvement is obtained in sig-
¹⁴¹⁵ nificance by applying a gluon selection to one of the two leading jets. The resulting
¹⁴¹⁶ significances are in Fig. 6.60 where an increase of 25% in significance at masses above
¹⁴¹⁷ 5 TeV is obtained, with the largest increases happening over 70% gluon efficiency.

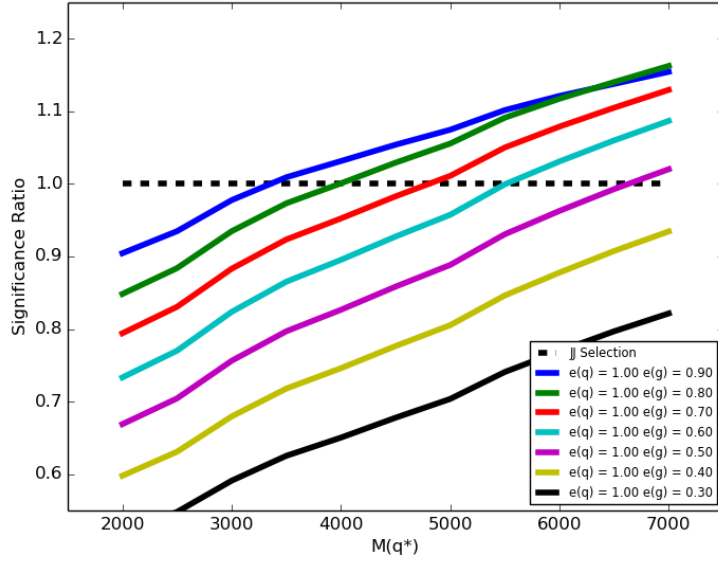


Figure 6.60 The significance for observing a q^* with masses from 2000 to 7000 GeV for ϵ_{gG} ranging from 30 to 90% compared to the significance calculated with no gluon selection applied. The key gives pairs of efficiencies (ϵ_{gG} , ϵ_{qG}).

6.3.2 Selection Criteria

The selection criteria for an quark-enriched jet sample was chosen so that 60% quark-initiated purity is achieved in each jet p_T bin. However, discontinuities in the m_{jj} spectrum would occur when such criteria is applied to the high mass ($p_T > 5000$ GeV), leads to difficulties presented in resonance search.

A selection criteria is thus built as a linear function of the $\ln(p_T)$, results in a smooth m_{jj} distribution. A jet is tagged as being more likely to be quark-initiated if N_{trk} is less than the threshold n_q and more likely to be gluon-initiated if N_{trk} is greater than the threshold n_g :

$$N_{\text{trk}} \leq n_q \text{ quark-initiated sample} \quad (6.8)$$

$$N_{\text{trk}} \geq n_g \text{ gluon-initiated sample}$$

where

$$n_{q(g)} = c_{q(g)} + m_{q(g)} \ln(p_T) \quad (6.9)$$

parameters $m_{q(g)}$ and $c_{q(g)}$ are constants obtained from the MC samples, these are founded

1425 by finding the value of N_{trk} that corresponds to a given efficiency for truth quark and gluon
 1426 jets in p_T bins, and chosen to defined suitable subsamples, the p_T here is in units of GeV.

1427 For each p_T bin, the number of tracks N_{trk} that closest to the given selection effi-
 1428 ciency is found. Because the N_{trk} is an integer number of track thus does not correspond
 1429 exactly to the selection efficiency, a linear interpolation is carried out between the given
 1430 efficiencies of the selected bin and the closest bin of it, to correct the fractional number
 1431 of tracks that corresponds to the selection efficiency, the corresponding uncertainty is
 1432 evaluated as binomial distribution.

1433 The jet p_T bin edges are divided into 480, 500, 520, 540, 560, 580, 600, 625, 650,
 1434 700, 750, 800, 900, 1000, 1400, 1600, 1800, 2000, 2500, 3000, 3500, 4000, 5000, 6000
 1435 GeV. An example of the cumulative distribution of N_{trk} for truth quark- and gluon-jets at
 1436 the p_T range of 800 - 900 GeV is shown in Figure 6.61.

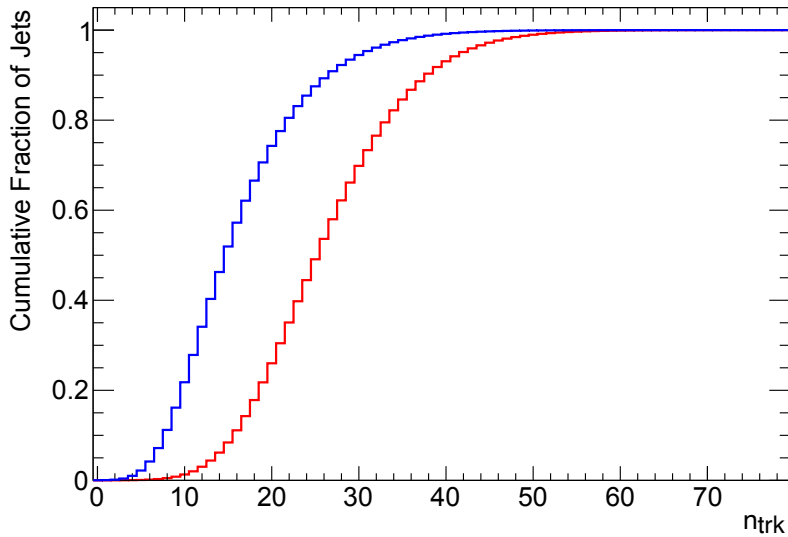


Figure 6.61 The cumulative distribution of N_{trk} for truth quark- (blue) and gluon- (red)jets satisfying $800 < p_T < 900$ GeV.

1437 The coefficients for Equation 6.9 are determined for quark and gluon selection ef-
 1438 ficiencies ranging from 65% to 95% in increments of 5%. The plot showcasing the N_{trk}
 1439 values corresponding to selection efficiencies of 70%, 75%, and 80% is depicted in Fig-
 1440 ure 6.62, along with the optimal fit employing Equation 6.9. The constants' values for
 1441 both quark and gluon selections are summarized in Tables 6.25 and 6.26. For a selec-
 1442 tion efficiency of 75%, the fitting yields a χ^2 of 33.5 (quark selection) and 2.6 (gluon
 1443 selection) for 21 degrees of freedom.

Notably, the N_{trk} value that satisfies the selection efficiency attains a plateau above 4000 GeV, suggesting the potential presence of a saturation effect. To validate these findings, the data is subjected to an alternative fit function. An alternative fit function is derived as a cross check:

$$n_{q(g)} = c + m \ln(p_T) + n \sqrt{\ln(p_T)}. \quad (6.10)$$

which improve the χ^2 of the fit in a selection efficiency of 75% from 33.5 to 25.1 in quark-selection, and from 2.6 to 1.6 in gluon-selection. Figure 6.63 shows the alternative fit for quark and gluon selections. The values of the constants for both quark and gluon selections are summarised in Tables 6.27 and 6.28.

The values of the constants for both quark and gluon selections are summarised in Tables 6.25 and 6.26.

Truth- q selection efficiency	Truth- g selection efficiency	c	m
0.95	0.732	-27.568	8.789
0.90	0.563	-21.518	7.269
0.85	0.447	-17.646	6.304
0.80	0.350	-14.956	5.610
0.75	0.278	-12.600	5.022
0.70	0.221	-10.691	4.536
0.65	0.174	-8.990	4.105

Table 6.25 Values of constants m and c from Equation. 6.9 such that $N_{\text{trk}} \leq n_q$ for truth quark jets for a range of efficiencies from 65 to 95%.

1453

Truth- g selection efficiency	Truth- q selection efficiency	c	m
0.95	0.586	-7.541	3.233
0.90	0.456	-8.980	3.779
0.85	0.377	-10.419	4.230
0.80	0.320	-11.964	4.659
0.75	0.274	-13.376	5.047
0.70	0.234	-14.937	5.446
0.65	0.202	-16.466	5.834

Table 6.26 Values of constants m and c from Equation 6.9 such that $N_{\text{trk}} \geq n_g$ for truth quark jets for a range of efficiencies from 65 to 95%.

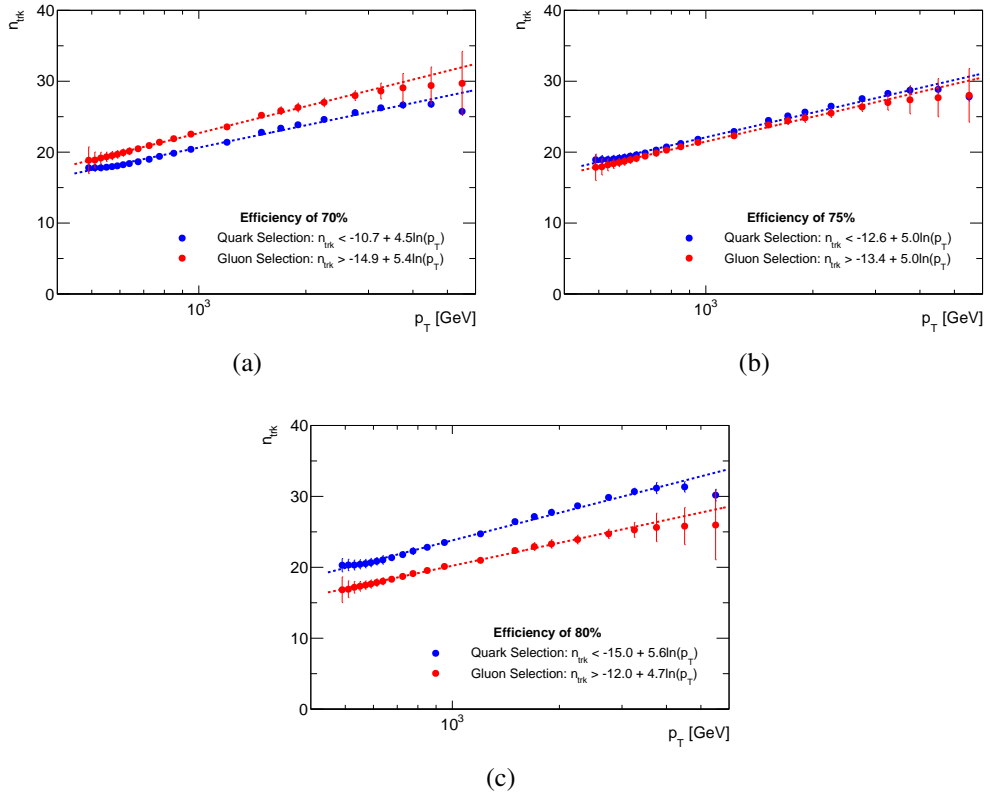


Figure 6.62 The values of N_{trk} for (a) 70%, (b) 75% and (c) 80% quark (blue) and gluon (red) selection efficiencies in each p_T bin along with the best fit to Equation 6.9.

Search for new phenomena in dijet events

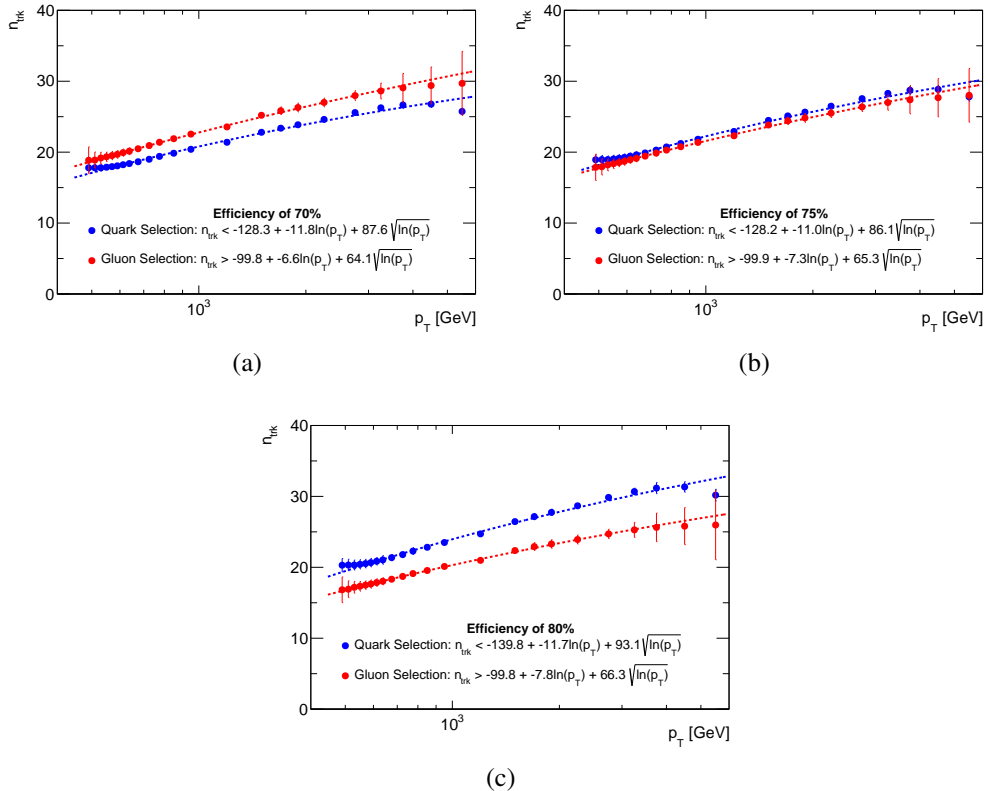


Figure 6.63 The values of N_{trk} for (a) 70%, (b) 75% and (c) 80% quark (blue) and gluon (red) selection efficiencies in each p_T bin along with the best fit to Equation 6.10.

Search for new phenomena in dijet events

Truth- q selection efficiency	Truth- g selection efficiency	c	m	n
0.80	0.350	-139.822	-11.714	93.100
0.75	0.278	-128.174	-11.001	86.141
0.70	0.221	-128.255	-11.755	87.604

Table 6.27 Values of constants m and c from Equation 6.10 such that $N_{\text{trk}} \leq n_q$ for truth quark jets for a range of efficiencies from 70 to 80%.

Truth- g selection efficiency	Truth- q selection efficiency	c	m	n
0.80	0.320	-99.796	-7.839	66.301
0.75	0.274	-99.949	-7.271	65.347
0.70	0.234	-99.774	-6.640	64.077

Table 6.28 Values of constants m and c from Equation 6.10 such that $N_{\text{trk}} \geq n_g$ for truth quark jets for a range of efficiencies from 70 to 80%.

6.3.2.1 Signal Selection Efficiencies

The H' signal described in section 6.1.2 is required to pass the selection criteria for a single jet gluon selection efficiency of 75% given in Table 6.29. The selection efficiency for the H' sample is expected to be 56.3% (0.75^2 as both jets are required to be 75%). In actual process, the ratio of H' events that decay to two gluons ranges from 51.9% for a 2 TeV signal to 57.4% for a 7 TeV signal.

The effective fraction of H' events decaying into two gluons is slightly below 100%, due to factors like gluon splitting and other showering effects. This fraction varies from 91.3% to 95.4%. The discrepancy between the actual efficiency and the expected efficiency (56.3% of the truth efficiency) is depicted in Figure 6.64. The average difference across selection criteria is approximately 3.3%.

Since there is minimal distinction between the two selection criteria, the simpler choice outlined in Equation 6.9 will be adopted.

H' Mass (GeV)	Selection efficiency(%)		
	Equation 6.9	Equation. 6.10 ($\sqrt{}$ term)	Truth
2000	51.9	51.8	91.3
2500	53.2	53.0	91.7
3000	54.9	54.6	92.3
3500	55.3	55.1	93.4
4000	56.4	56.2	93.4
4500	56.7	56.7	94.1
5000	56.2	56.4	94.3
5500	57.2	57.5	94.9
6000	57.4	57.8	95.1
6500	57.4	58.3	95.5
7000	57.4	58.1	95.4

Table 6.29 The signal selection efficiency for a fully simulated H' decaying to two gluons with requiring two jets to pass the 75% single jet criteria given in Equation 6.9 with constants from Table 6.26 and the criteria given in Equation 6.10 with constants from Table 6.28. The expected double tagged gluon efficiency is 56.3%.

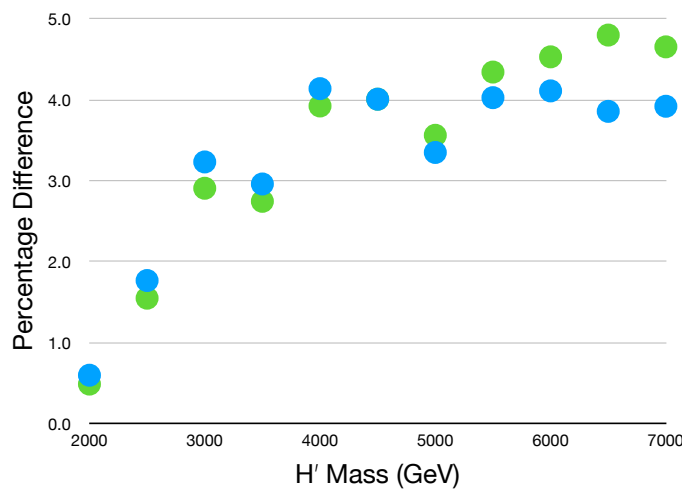


Figure 6.64 The difference between the expected signal selection efficiency of 56.3% for a single jet selection efficiency of 75% for H' using Equation 6.9 (Blue) and Equation 6.10 (Green)

6.4 Signal Optimisation

6.4.1 y^* Cut Optimisation

In QCD, t -channel in 2-to-2 scattering is the dominant process. Thus the dijet production from the QCD is proportional to $(1 - \cos \theta^*)^{-2}$. However the distribution of $\cos \theta^*$ is supposed to be flat for H' signal, which means the y^* of H' signal will peak at 0 while that of QCD background will minimize at 0.

The significance is defined as:

$$S = \sqrt{\sum_i 2 \left[(S_i + B_i) \cdot \ln \left(1 + \frac{S_i}{B_i} \right) - S_i \right]} \quad (6.11)$$

where S_i (B_i) is the number of signal (background) events in bin i . The calculation of such significance only include the bins where signal samples have 95% of the area under the distribution, not include the entire m_{jj} distribution.

For some signal samples where S_i is small ($S_i \ll 10^{-5}$) thus the logarithm functions do not have enough precision in equation 6.11. An approximation is introduced as follows:

$$S = \sqrt{\sum_i 2 \sum_{n=1}^6 \frac{(-S_i)^{n+1}}{n(n+1)B_i^n}} \quad (6.12)$$

which is accurate up to 10 decimal places around $\frac{S_i}{B_i} = 10^{-5}$ and even more precise for smaller $\frac{S_i}{B_i}$.

The significance of H' signal as a function of the value of the y^* is shown in Figure. 6.65. The peaks of significance in all tagging categories are around 0.6, therefore an optimal y^* cut for the H' search is set to $|y^*| < 0.6$. The exact values of y^* cut that correspond to the peak significance value for the H' signal at each mass point are shown in Table 6.30 with the ranges in y^* cut around the peak that gives a significance ≥ 0.99 .

For String signal, there is also a dependence on $\cos \theta^*$, leads the y^* will peak at 0 too. Figure. 6.66 shows the significance of String signal as a function of y^* cut. The maximum significance in all tagging categories are around 0.8, therefore an optimal y^* cut for the String search is set to $|y^*| < 0.8$. The exact values of y^* cut that correspond to the peak significance value for the String signal at each mass point are shown in Table. 6.31 with the ranges in y^* cut around the peak that gives a significance ≥ 0.99 .

Figure. 6.67 shows the significance of Graviton signal as a function of y^* cut. The

Search for new phenomena in dijet events

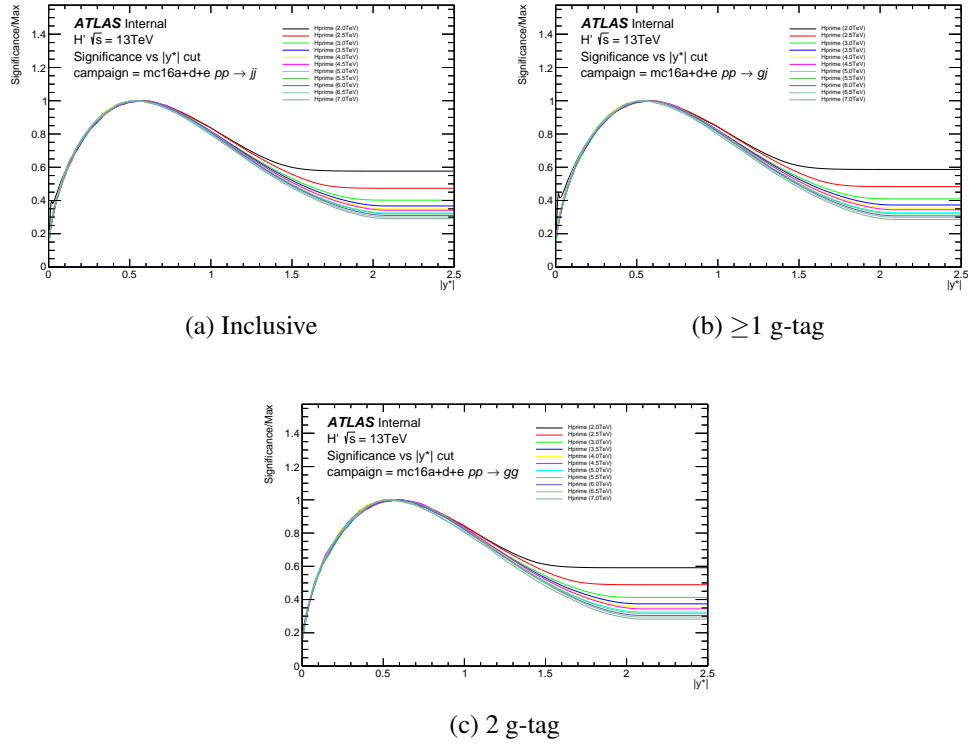


Figure 6.65 H' significance as a function y^* cut in the case of (a) Inclusive, (b) ≥ 1 g-tag, (c) 2 g-tag.

H' Mass (TeV)	Optimal Selection			Peak Width
	Inclusive	≥ 1 g tag	≥ 2 g tag	
2.0	0.57	0.57	0.57	0.50–0.65
2.5	0.58	0.59	0.62	0.50–0.67
3.0	0.59	0.59	0.59	0.50–0.66
3.5	0.56	0.56	0.60	0.49–0.65
4.0	0.58	0.58	0.58	0.47–0.65
4.5	0.55	0.57	0.57	0.35–0.68
5.0	0.55	0.56	0.57	0.47–0.66
5.5	0.55	0.55	0.57	0.46–0.66
6.0	0.60	0.60	0.60	0.52–0.66
6.5	0.55	0.55	0.54	0.47–0.64
7.0	0.56	0.56	0.51	0.35–0.61

Table 6.30 $|y^*|$ selection leading to the maximum significance value calculated using Equation 6.11.

Search for new phenomena in dijet events

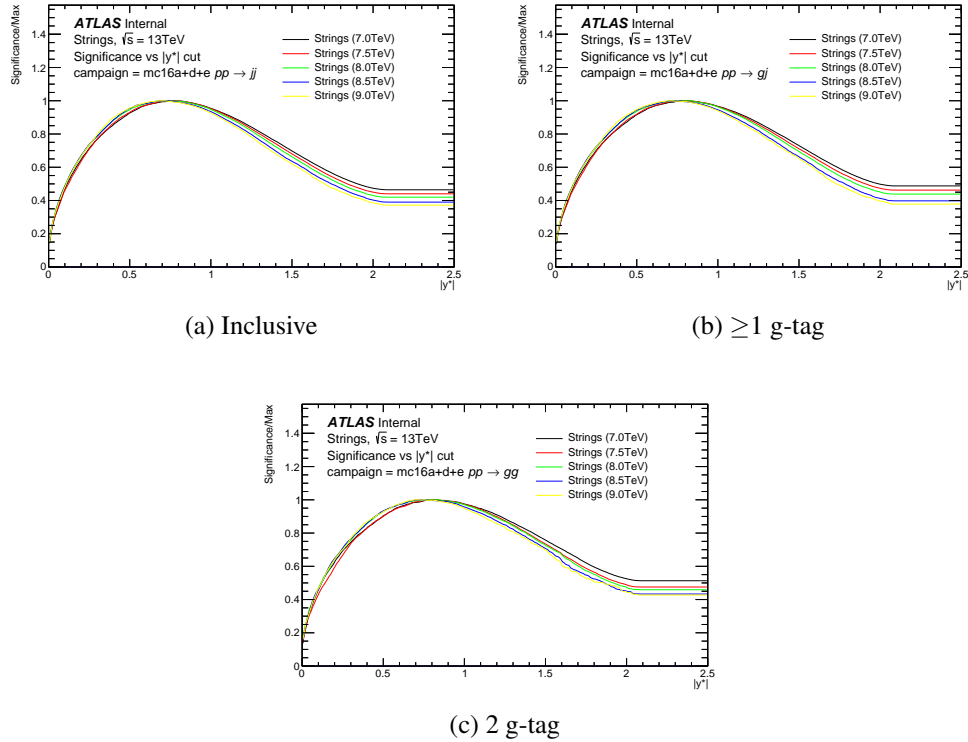


Figure 6.66 String significance as a function y^* cut in the case of (a) Inclusive, (b) ≥ 1 g-tag, (c) 2 g-tag.

String Mass (TeV)	Optimal Selection			Peak Width
	Inclusive	≥ 1 g tag	≥ 2 g tag	
7.0	0.78	0.82	0.81	0.70–0.91
7.5	0.77	0.77	0.83	0.68–0.91
8.0	0.72	0.76	0.84	0.66–0.90
8.5	0.74	0.74	0.74	0.65–0.85
9.0	0.71	0.71	0.71	0.62–0.84

Table 6.31 $|y^*|$ selection leading to the maximum significance value calculated using Equation 6.11.

significance peaks at about 0.6, so the optimal cut for the Graviton search is $|y^*| < 0.6$. Table 6.32 shows the y^* cut corresponding to the peak significance value for Graviton at each mass point, and the range in y^* cut around the peak that gives a significance ≥ 0.99 .

Figure 6.68 shows the significance of QBH signal as a function of y^* cut. The maximum significance is at about 0.9, so the optimal cut for the QBH search is $|y^*| < 0.9$.

Search for new phenomena in dijet events

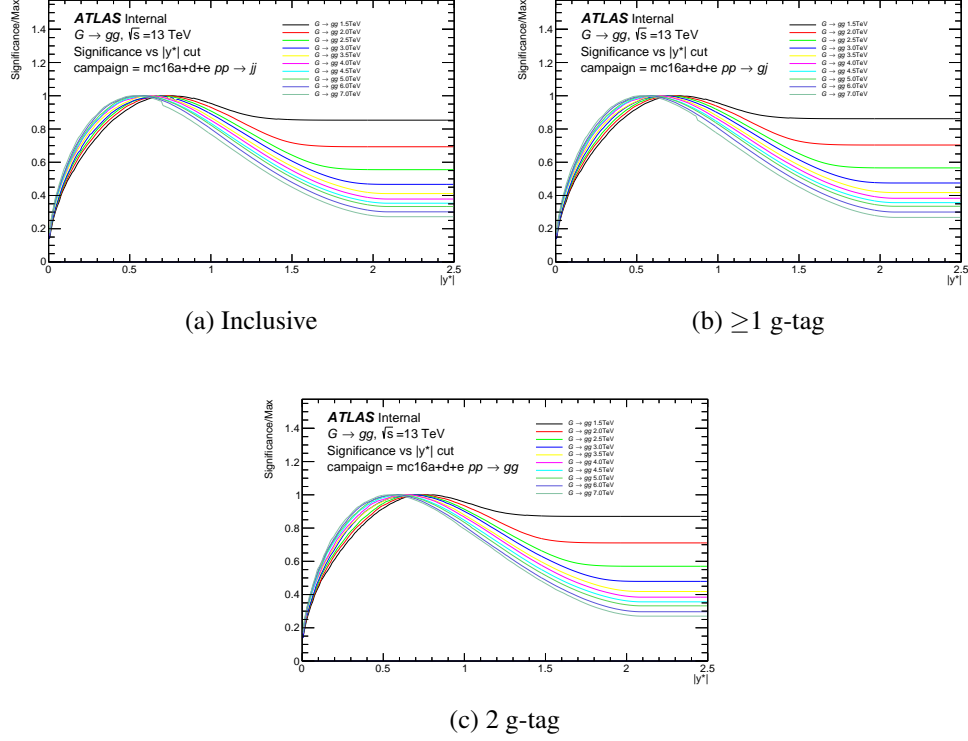


Figure 6.67 Graviton significance as a function y^* cut in the case of (a) Inclusive, (b) ≥ 1 g-tag, (c) 2 g-tag.

Graviton Mass (TeV)	Optimal Selection			Peak Width
	Inclusive	≥ 1 g tag	2 g tag	
1.5	0.77	0.77	0.78	0.65–0.87
2.0	0.71	0.74	0.72	0.65–0.83
2.5	0.67	0.69	0.70	0.61–0.80
3.0	0.66	0.66	0.66	0.60–0.77
3.5	0.64	0.65	0.65	0.57–0.73
4.0	0.63	0.64	0.64	0.55–0.73
4.5	0.59	0.59	0.59	0.53–0.69
5.0	0.59	0.59	0.59	0.50–0.69
6.0	0.57	0.57	0.60	0.49–0.66
7.0	0.53	0.53	0.56	0.47–0.63

Table 6.32 $|y^*|$ selection leading to the maximum significance value calculated using Equation 6.11.

1499 Table 6.33 shows the y^* cut corresponding to the peak significance value for the QBH at each mass point, and the range in y^* cut around the peak that gives a significance ≥ 0.99

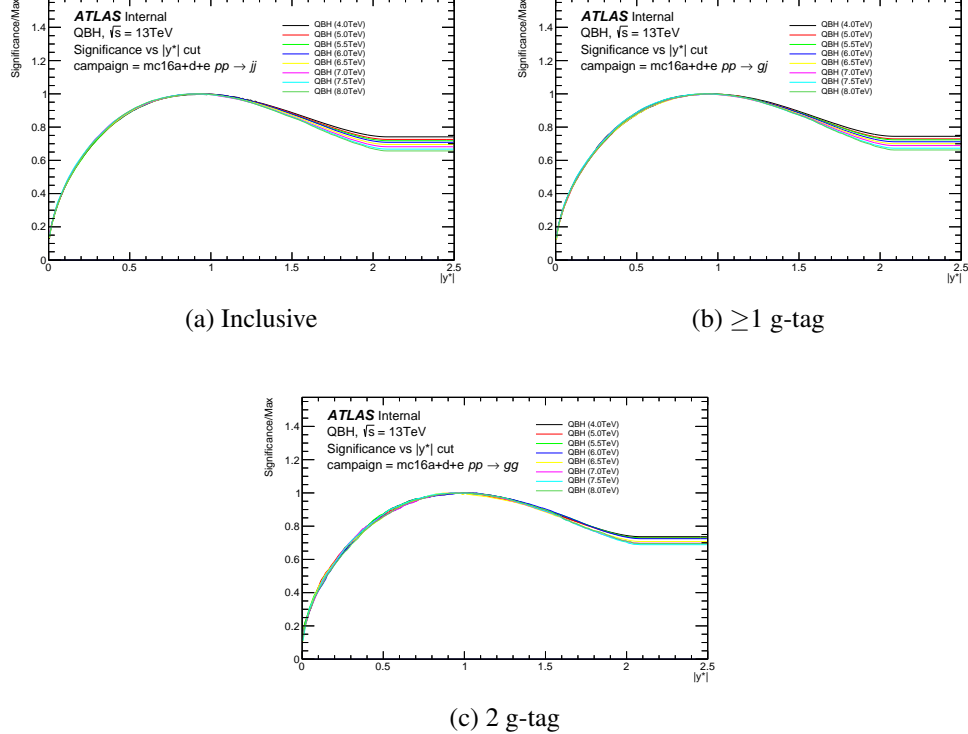


Figure 6.68 QBH significance as a function y^* cut in the case of (a) Inclusive, (b) ≥ 1 g-tag, (c) 2 g-tag.

1500

QBH Mass (TeV)	Optimal Selection			Peak Width
	Inclusive	≥ 1 g tag	2 g tag	
4.0	0.92	0.95	1.01	0.81–1.11
5.0	0.95	0.95	0.95	0.81–1.09
5.5	0.94	0.96	0.94	0.81–1.09
6.0	0.92	0.96	1.01	0.81–1.09
6.5	0.91	0.91	0.93	0.81–1.06
7.0	0.93	0.97	0.94	0.82–1.07
7.5	0.92	0.94	0.93	0.79–1.08
8.0	0.92	0.96	0.99	0.82–1.09

Table 6.33 $|y^*|$ selection leading to the maximum significance value calculated using Equation 6.11.

 1501 **6.4.2 Dijet Mass Turn-on**

1502 The m_{jj} turn-on is investigated by comparing events collected with the highest
 1503 p_T trigger threshold with one with a lower p_T threshold using data. The efficiency of the
 1504 HLT_j420 trigger is calculated by comparing to the following triggers in each data taking
 1505 period: 2015 HLT_j360, 2016 HLT_j380, 2017 and 2018 HLT_mu50. The muon trigger
 1506 2017 and 2018 are included as HLT_j420 is the only unprescaled jet trigger available.
 1507 The full Run 2 dataset is included for comparison as the HLT_mu50 is available for all
 1508 running periods. Events where the efficiency of trigger less than 99.5% will be removed
 1509 by a mass cut.

1510 The efficiencies as a function of m_{jj} are shown in Figure. 6.69 for $|y^*| < 0.6$ and
 1511 Figure. 6.70 for $|y^*| < 0.8$ in two gluon-tag categories for both triggers. The results are
 1512 summarised in Table. 6.34 for the different data-taking periods. The m_{jj} mass cut is
 1513 chosen to be slightly above the value of the plateau ($\geq 99.5\%$), so a cut of 1100 GeV for
 1514 $|y^*| < 0.6$ is applied. For $|y^*| < 0.8$, a cut of 1200 is applied to samples with either one
 1515 or two gluon tags.

Data Taking Period	Mass turn on $ y^* < 0.6$		Mass turn on $ y^* < 0.8$	
	≥ 1 g-tag (GeV)	≥ 2 g-tag (GeV)	≥ 1 g-tag (GeV)	≥ 2 g-tag (GeV)
2015	1040	1030	1160	1160
2016	1030	1030	1160	1170
2017	990	1000	1110	1120
2018	1000	1010	1110	1120
Run 2	1020	1030	1120	1120

Table 6.34 The m_{jj} value of the start of the plateau ($\geq 99.5\%$) for each period of data taking.

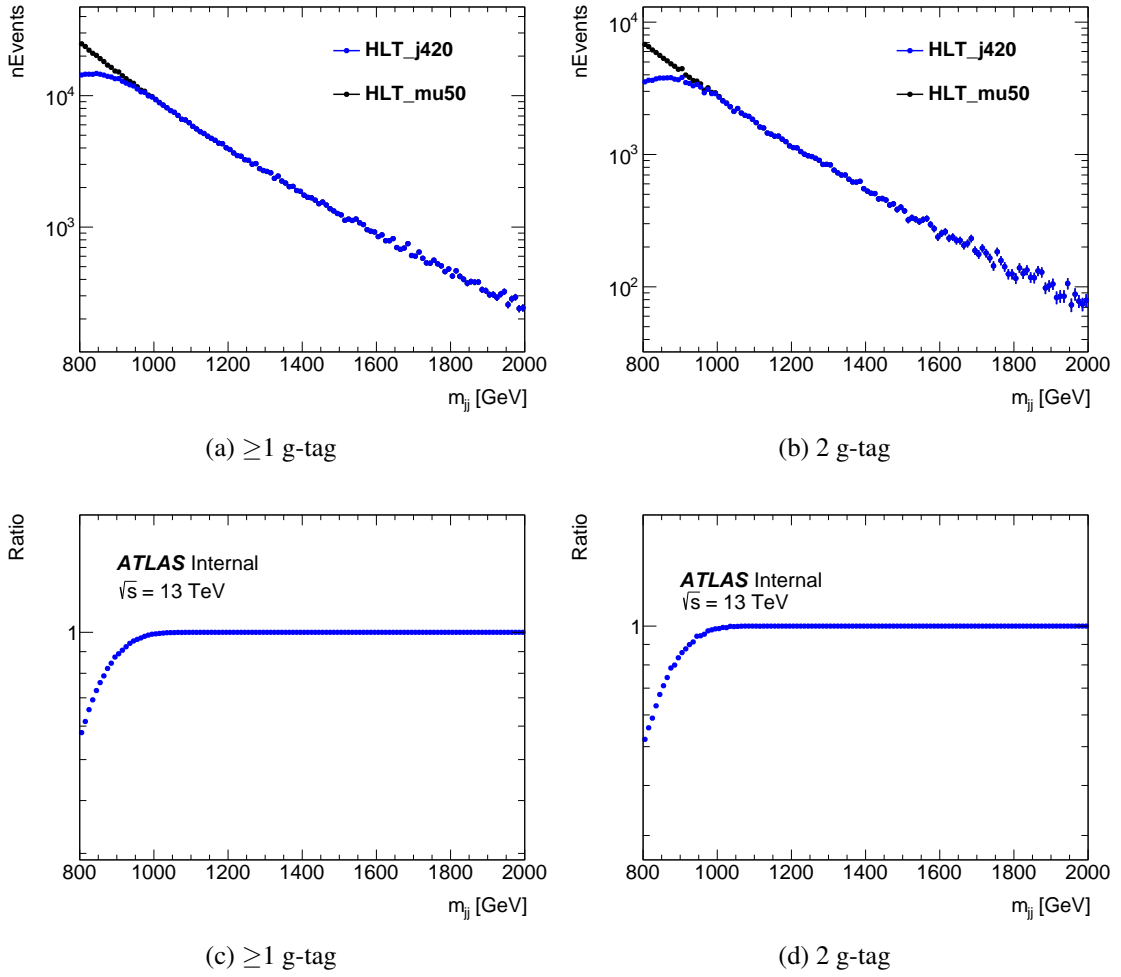


Figure 6.69 Eiciencies as a function of m_{jj} for $|y^*| < 0.6$ using HLT_j420 compared with HLT_mu50 in the case of comparison of mass spectra with (a) ≥ 1 g-tag, (b) 2 g-tag and the ratio between the two (c) ≥ 1 g-tag and (d) 2 g-tag.

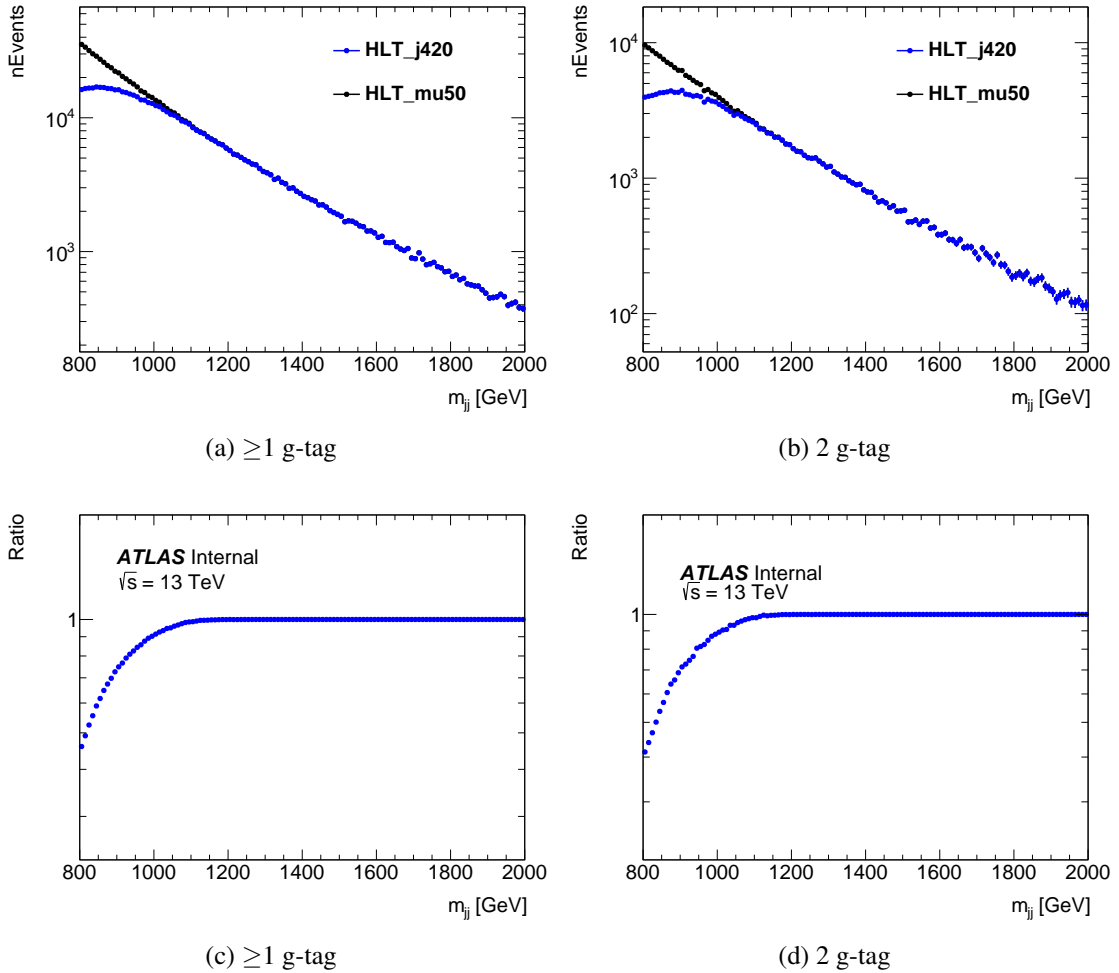


Figure 6.70 Eiciencies as a function of m_{jj} for $|y^*| < 0.8$ using HLT_j420 compared with HLT_mu50 in the case of comparison of mass spectra with (a) ≥ 1 g-tag, (b) 2 g-tag and the ratio between the two (c) ≥ 1 g-tag and (d) 2 g-tag.

1516 **6.4.3 Optimised Selection**

1517 In addition to the baseline selection described in Section 6.2.2, optimized cuts are
 1518 applied to different tagging regions to improve the search potential with good tracking
 1519 efficiency.

1520 The following additional cuts are applied for the the inclusive samples.

- 1521 • $|y^*| < 0.8$
- 1522 • $m_{jj} > 1200 \text{ GeV}$

1523 The following additional cuts are for quark-gluon tagging.

- 1524 • $|\eta| < 2.1$ (both jets) for track acceptance
- 1525 • ≥ 1 gluon tagged (75% working point)
- 1526 • 2 gluons tagged (75% working point)

1527 where the 75% gluon selection criteria is applied as: $N_{\text{trk}} > -7.3 + 4.2 \ln(p_T)$, with jet
 1528 p_T in GeV.

1529 The acceptance times efficiency as a function of signal masses in inclusive, signal-
 1530 gluon and double-gluon tagged regions for different benchmark signal models are shown
 1531 in Figure 6.71.

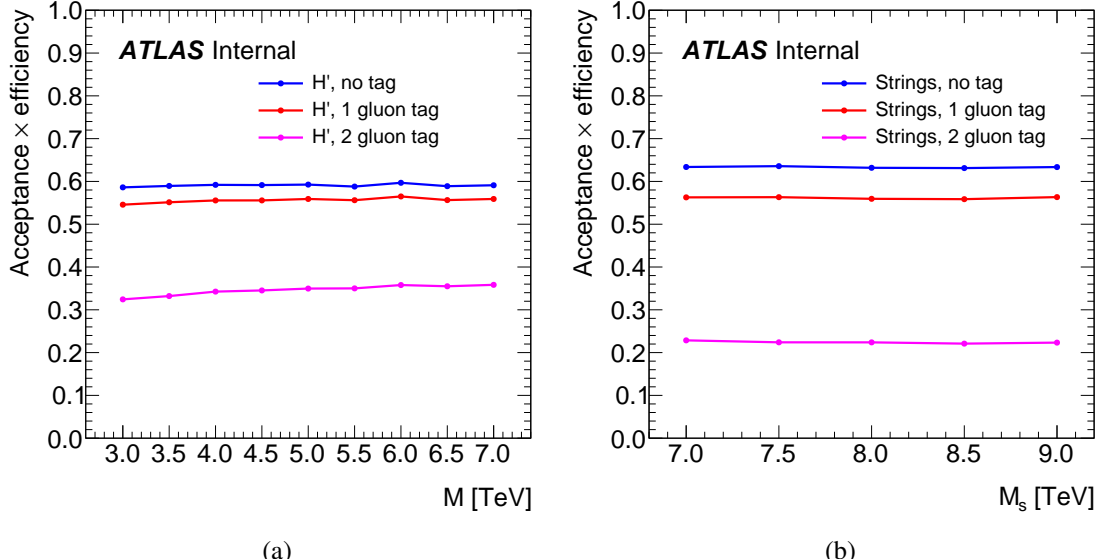


Figure 6.71 Acceptance times efficiency for the (a) H' signal and (b) String signal.

1532 6.4.4 Selected Kinematic Plots

1533 In this section a selection of kinematic and monitoring plots processed with sam-
 1534 ples passed the gluon-gluon selection criteria are shown in Figure 6.72, 6.73, 6.74. The
 1535 distributions of kinematics in MC are consistent with full dataset.

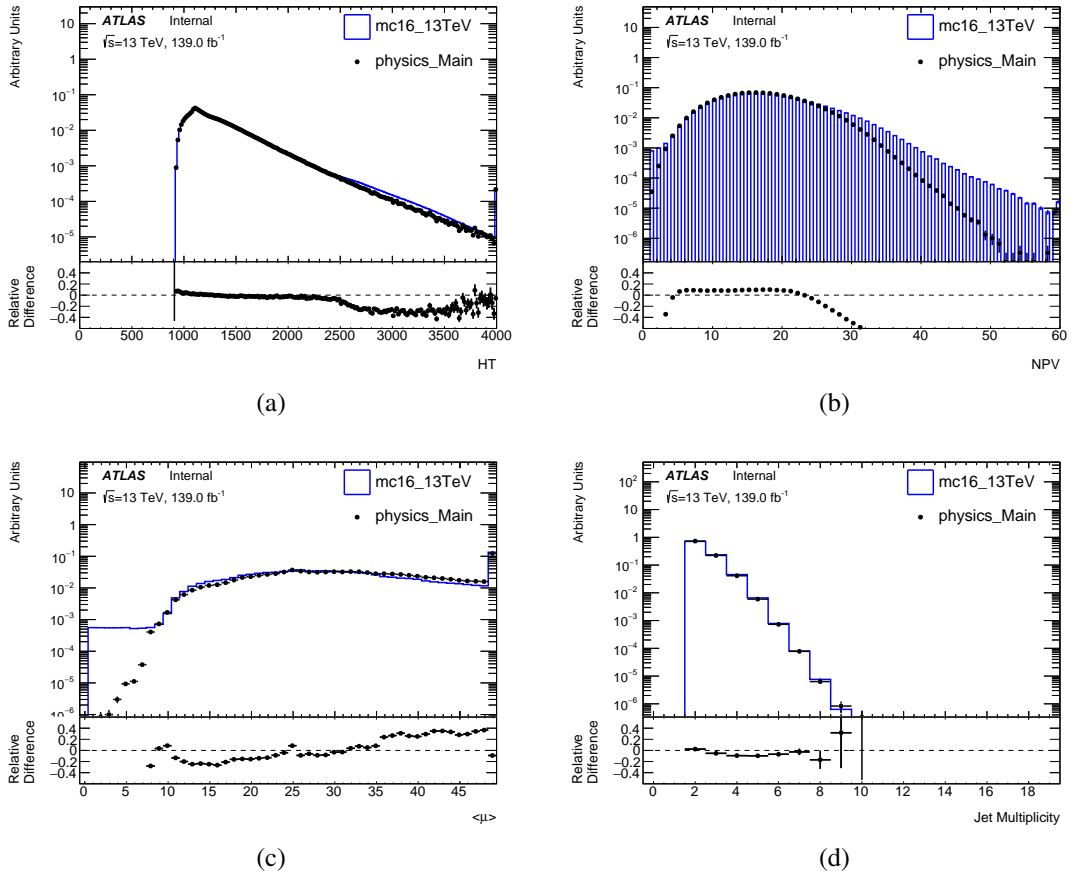


Figure 6.72 Monitoring plots for the gluon-gluon selection. (a) scalar p_T sum of all parton-level jets (H_T), (b) number of primary interaction vertices (NPV), (c) average interactions per bunch crossing, and (d) number of jets.

Search for new phenomena in dijet events

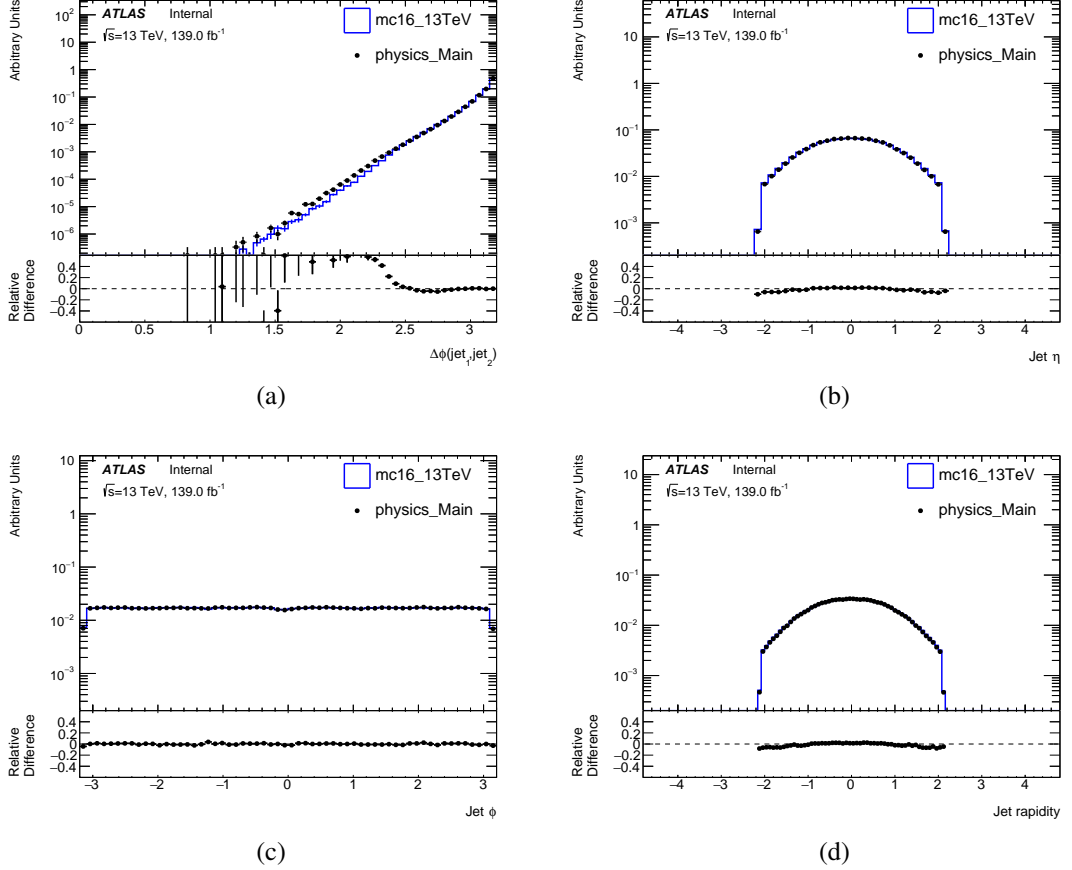


Figure 6.73 Monitoring plots on the gluon-gluon sample. (a) $\Delta\phi$ between the two jets, (b) jet η , (c) jet ϕ , and (d) jet rapidity.

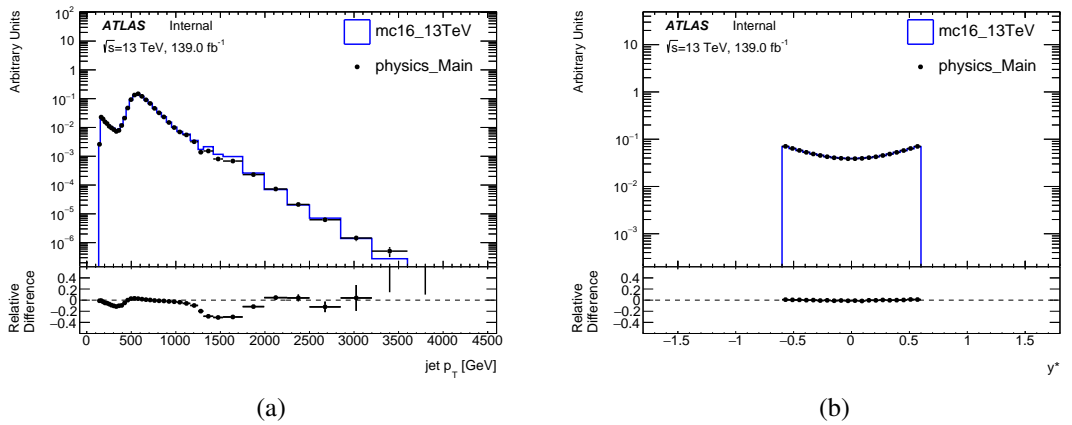


Figure 6.74 Monitoring plots on the gluon-gluon sample. (a) jet p_T , (b) y^* .

1536 6.5 Statistical Framework

1537 6.5.1 Fitting Framework

1538 The fitting framework used to parameterise QCD background is based on XML
 1539 Analytic Workspace Builder [?] (`xmlAnaWSBuilder`), which employs one-dimensional
 1540 observables to create RooFit [?] workspaces. The workflow of the framework is sum-
 1541 marised in Figure 6.75.

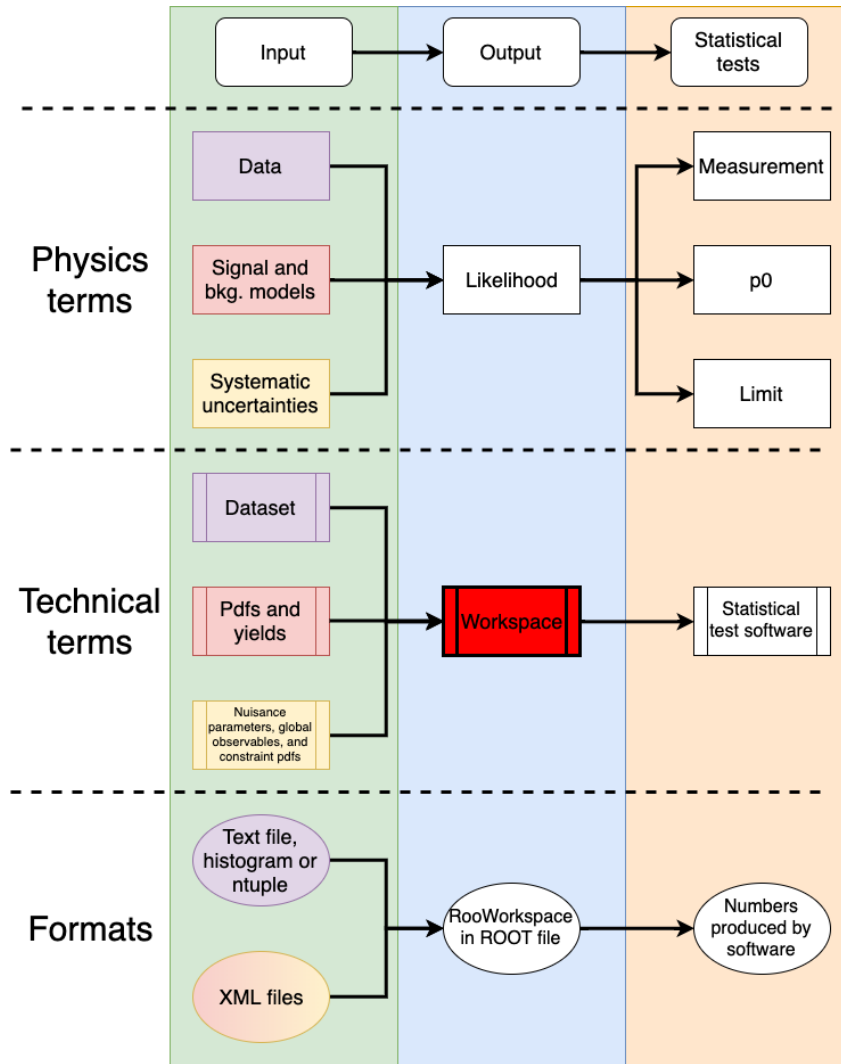


Figure 6.75 Workflow of the XmlAnaWSBuilder.

1542 The quickFit framework [?] that based on RooFit data fitting package is used for
 1543 data fitting. Modifications are needed so that it can integrate over binned data, as RooFit
 1544 evaluates its fit functions using the centre value of each bin rather than the actual average

mass in each bin. As a result, significant biases could occur in the fit results [?]. Recent developments introduce a new class of `RooBinSamplingPdf` in to `RooFit` package, which solve such issue.

6.5.2 Statistical Method

In this analysis, the discriminating variable is set to the dijet invariant mass m_{jj} , and the distribution of it is used as a probability density function (pdf) to build the likelihood function.

6.5.2.1 Parametric background models

The distribution of m_{jj} of background is parameterized by

$$f_b(m_{jj}; \mathbf{p}_b) = f_b(m_{jj}; p_1, p_2, p_3, p_4, p_5) = p_1 \left(1 - \frac{m_{jj}}{\sqrt{s}}\right)^{p_2} \left(\frac{m_{jj}}{\sqrt{s}}\right)^{p_3 + p_4 \ln\left(\frac{m_{jj}}{\sqrt{s}}\right) + p_5 \left[\ln\left(\frac{m_{jj}}{\sqrt{s}}\right)\right]^2}, \quad (6.13)$$

where \mathbf{p}_b are free parameters determined by fitting to data (or pseudo data), and $\sqrt{s} = 13$ TeV. In some cases, $p_5 = 0$ is taken. We will assume Equation (6.13) is normalized to unity as needed.

Given that we are employing a binned likelihood approach and working with histograms, it becomes essential to determine the average count of events in the i th bin, arising from both the signal and background contributions:

$$s_i = s_{\text{tot}} \int_{\text{bin } i} f_s(m_{jj}; \mathbf{p}_s) dm_{jj}, \quad (6.14)$$

$$b_i = b_{\text{tot}} \int_{\text{bin } i} f_b(m_{jj}; \mathbf{p}_b) dm_{jj}, \quad (6.15)$$

where f_s and f_b are pdfs of m_{jj} for the signal and background, respectively. The quantities s_{tot} and b_{tot} represent the total mean numbers of signal and background events. The variable b_{tot} is an additional nuisance parameter. The signal normalization s_{tot} is not treated as a parameter that can be adjusted, but rather is set to the value determined by the nominal signal model. The parameter can be expressed as $s_{\text{tot}} = \sigma L \epsilon$, where σ is fixed by the model cross section, and L and ϵ represent the nominal luminosity and total acceptance times efficiency, respectively.

1567 6.5.2.2 Uncertainties

1568 In this analysis, there are six sources of systematic uncertainties on the signal studied:

1569 δL an uncertainty on the integrated luminosity of the data sample,

1570 $\delta \epsilon$ an uncertainty on the signal efficiency times acceptance,

1571 δt an uncertainty on the gluon-tag efficiency,

1572 δE_{JER} an uncertainty on the jet energy resolution, and

1573 δE_{JES} an uncertainty on the jet energy scale.

1574 δS an uncertainty due to spurious signals.

1575 All these uncertainties are treated as shape uncertainties except for δL which is a normal-
 1576 ization uncertainty. These uncertainties are associated to nuisance parameters denoted
 1577 by $\alpha_L, \alpha_\epsilon, \alpha_t, \alpha_{E_{\text{JER}}}, \alpha_{E_{\text{JES}}}, \alpha_S$, respectively, and the values of the auxiliary measurements
 1578 by $\theta_b, \theta_L, \theta_\epsilon, \theta_t, \theta_{E_{\text{JER}}}, \theta_{E_{\text{JES}}}, \theta_S$, respectively.

1579 6.5.2.3 Likelihood function definition

1580 A binned likelihood is used in this analysis. Consider the m_{jj} histogram of $n =$
 1581 (n_1, \dots, n_N) events, the likelihood function without uncertainties is built as:

$$\mathcal{L}(\mu; b_{\text{tot}}, \mathbf{p}_s, \mathbf{p}_b) = \prod_{i=1}^N \frac{(\mu s_i + b_i)^{n_i}}{n_i!} e^{-(\mu s_i + b_i)}, \quad (6.16)$$

1582 where the parameter of interest (POI) μ is the signal strength parameter, b_i is the num-
 1583 ber of background events in the i bin, s_i is the number of signal events in the i bin.
 1584 Background-only hypothesis corresponding to $\mu = 0$, whereas nominal signal hypothe-
 1585 sis corresponding to $\mu = 1$.

1586 The full likelihood function with uncertainties included is defined as:

$$\begin{aligned} \mathcal{L}(\mu; b_{\text{tot}}, \mathbf{p}_s, \mathbf{p}_b, \boldsymbol{\alpha}_s) &= \prod_{i=1}^N \frac{(\mu_i^T)^{n_i}}{n_i!} e^{-\mu_i^T} N_i(\alpha_L; \theta_L, \delta_L) N_i(\alpha_\epsilon; \theta_\epsilon, \delta \epsilon) \\ &\cdot N_i(\alpha_t; \theta_t, \delta E_t) N_i(\alpha_{E_{\text{JER}}}; \theta_{E_{\text{JER}}}, \delta E_{\text{JER}}) \end{aligned} \quad (6.17)$$

$$\cdot N_i(\alpha_{E_{\text{JES}}}; \theta_{E_{\text{JES}}}, \delta E_{\text{JES}}) N_i(\alpha_S; \theta_S, \delta_S), \quad (6.18)$$

1587 where μ_i^T is the total number of expected event in the i bin, which is given by:

$$\mu_i^T = \mu s_i \eta_i^L(\alpha_L) \eta_i^\epsilon(\alpha_\epsilon) \eta_i^t(\alpha_t) \eta_i^{E_{\text{JER}}}(\alpha_{E_{\text{JER}}}) \eta_i^{E_{\text{JES}}}(\alpha_{E_{\text{JES}}}) + b_i. \quad (6.19)$$

1588 The parameter $\eta^s(\alpha_s)$ are response functions for uncertainty s , and the subsidiary mea-
1589 surements are constrained by the $N(\alpha; \theta, \delta)$ functions.

1590 In this analysis, constraint functions are built from standard Gaussians, together
1591 with uncertainties that mapped in the response functions. Luminosity uncertainty is
1592 fitted by a log-normal response function, the JER and JES uncertainties are given by
1593 Gaussian and asymmetric response functions, respectively. For each bin, a vertical inter-
1594 polation strategy called piece-wise linear method is used independently. In the case of
1595 the asymmetric error, the polynomial interpolation and exponential extrapolation method
1596 is used.

1597 The parameters $(\mu, N_b, p_s, p_b, \alpha_L)$ are fixed from the fit to data (pseudo-data) and
1598 are common for all bins, whereas parameters $(\alpha_\epsilon, \alpha_t, \alpha_{E_{\text{JER}}}, \alpha_{E_{\text{JES}}}, \alpha_S)$ are different from
1599 bin to bin.

1600 For simplicity in notation, the 18 nuisance parameters are written as the vector α ,
1601 where six of them have corresponding uncertainties. The simplified likelihood function
1602 is written as:

$$\mathcal{L}(\mu; \alpha) = \prod_{i=1}^N \frac{[\mu_i^T(\mu, \alpha)]^{n_i}}{n_i!} e^{-\mu_i^T(\mu, \alpha)} \prod_{s=1}^6 G_{i,s}(\alpha_s). \quad (6.20)$$

1603 6.5.2.4 Statistical Method

1604 A hypothesis test is used for estimating the compatibility between data and a theoreti-
1605 cal hypothesis, where the pseudo datasets are generated according to a given hypothesis,
1606 and compared to the tested dataset in terms of a test statistic.

1607 The procedure is demonstrated as follows: first, the agreement between the col-
1608 lected data and the null hypothesis is evaluated through a hypothesis test. The null hy-
1609 pothesis ($\mu = 0$) posits that only the SM background is present. If the data does not
1610 exhibit any substantial excess under this hypothesis test, the subsequent step involves es-
1611 tablishing an exclusion limit for the targeted signal model on the resonance cross section
1612 for m_{jj} . In this scenario, the hypothesis transforms into a signal + background assump-
1613 tion, leading to the construction of a test statistic based on the signal + background PDF
1614 of the discriminating variable.

1615 The statistical measurement's p-value serves as a quantification of the degree of
 1616 agreement or discrepancy between a hypothesis and the observed data. Mathematically,
 1617 it represents the integral of the distribution of the test statistic from the value obtained
 1618 for the dataset in question to infinity. This value characterizes the probability of achiev-
 1619 ing the observed outcomes assuming the null hypothesis. A lower p-value indicates a
 1620 higher degree of statistical significance for the observed incompatibility. For instance,
 1621 if the p-value of the data is below 0.05, it signifies that the likelihood of the observed
 1622 data aligning with the hypothesis is less than 5%. This prompts the assertion that the
 1623 hypothesis can be excluded at the 95% confidence level (CL).

1624 **6.5.2.5 Test statistic and p-value definitions**

1625 A binned maximum likelihood (ML) fitting method is used to extract the signal, to-
 1626 gether with profile likelihood ratio test statistic. The test statistics used for claiming a
 1627 positive signal is defined as:

$$q_0 = \begin{cases} -2 \ln \frac{\mathcal{L}(0, \hat{\alpha}(0))}{\mathcal{L}(\hat{\mu}, \hat{\alpha})} & \hat{\mu} \geq 0, \\ 0 & \hat{\mu} < 0. \end{cases} \quad (6.21)$$

1628 and the test statistic used for evaluating the upper limits is given as:

$$\tilde{q}_\mu = \begin{cases} -2 \ln \frac{\mathcal{L}(\mu, \hat{\alpha}(\mu))}{\mathcal{L}(0, \hat{\alpha}(0))} & \hat{\mu} < \mu, \\ -2 \ln \frac{\mathcal{L}(\mu, \hat{\alpha}(\mu))}{\mathcal{L}(\hat{\mu}, \hat{\alpha})} & 0 \leq \hat{\mu} \leq \mu, \\ 0 & \hat{\mu} > \mu. \end{cases} \quad (6.22)$$

1629 where the parameter μ represents the signal strength associated with the hypothesis being
 1630 tested. The maximum likelihood (ML) estimators that optimize the likelihood function
 1631 \mathcal{L} without constraints are referred to as $\hat{\mu}$ for the signal strength and $\hat{\alpha}$ for the other pa-
 1632 rameters. The parameter $\hat{\alpha}$ represents the conditional ML estimator of α that maximizes
 1633 \mathcal{L} while considering a specific value of μ .

1634 The p-value corresponding to the background-only hypothesis is expressed as:

$$p_0 = \int_{q_0, \text{obs}}^{\infty} f(q_0 | 0) dq_0. \quad (6.23)$$

1635 The values of \tilde{q}_μ are calculated for different values of μ by fitting a dataset where
 1636 the pseudo data is represented by μ' . This calculation of \tilde{q}_μ is conducted for each pseudo
 1637 dataset at various selected signal mass points, resulting in a distribution of \tilde{q}_μ denoted as

1638 $f(\tilde{q}_\mu | \mu = \mu')$. As a result, a p-value for the tested dataset is determined based on this
 1639 distribution:

$$p_{\mu'} = \int_{\tilde{q}'_{\mu,\text{obs}}}^{\infty} f(\tilde{q}_\mu | \mu = \mu') dq_\mu, \quad (6.24)$$

1640 the term $\tilde{q}'_{\mu,\text{obs}}$ represents the computed value of the test statistic based on the dataset
 1641 being tested. These p-values are also referred to as p_{s+b} , which signifies that they are
 1642 associated with the signal plus background hypothesis.

1643 6.5.2.6 Generation of pseudo-data

1644 The PDF of a certain model is used for generating the pseudo datasets. Signal +
 1645 background pseudo datasets are utilized to estimate the observed confidence level (CL) of
 1646 a signal + background hypothesis, while background-only pseudo datasets are employed
 1647 for expected CL estimations.

1648 During the generation of pseudo datasets, all parameters in the PDF are set to their
 1649 nominal values. The expected event counts in each bin follow a Poisson distribution.
 1650 Nuisance parameters (NPs), which represent systematic uncertainties, are treated ac-
 1651 cording to the "unconditional ensemble" approach: for each pseudo dataset, the values
 1652 of α_i (associated with the NPs) are drawn from their respective constraint terms, and
 1653 these values are used in both the likelihood \mathcal{L} and the computation of \tilde{q}_μ .

1654 6.5.2.7 Definition of exclusion limit

1655 The data is interpreted by the modified frequentest method (CL_s method), where p-
 1656 value is modified to take into account downward background fluctuations and quoted as
 1657 CL_s . The definition of CL_s is:

$$CL_s = \frac{p_{s+b}}{1 - p_b}, \quad (6.25)$$

1658 where $p_{b(s+b)}$ is the integrated value of the background-only (signal + background) dis-
 1659 tribution from zero to $\tilde{q}_\mu^{\text{obs}}$. Thus $1 - p_b$ is also referred to as the confidence level of the
 1660 background-only hypothesis (CL_b). The CL_s limit claims exclusion at 95% CL when
 1661 $CL_s = 0.05$.

1662 6.5.2.8 Implementation

1663 The statistical approach employed in this analysis differs slightly from previous dijet

1664 analyses and aligns with the current trigger-level analysis. In previous approaches, a
 1665 background model devoid of NPs was fitted to the data, and the resulting background
 1666 fit parameters were employed (and held constant) in subsequent likelihood fits involving
 1667 nuisance parameters. However, in this analysis, the background fit parameters are treated
 1668 as unconstrained NPs within the complete likelihood framework used in all fits.

1669 To create the RooFit workspaces, the XML Analytic Workspace Builder is utilized.
 1670 The xRooFit tool processes these workspaces and performs operations like setting limits,
 1671 among others, using classes from the RooFit and RooStats libraries.

1672 **6.5.3 Background Estimation**

1673 In the resonant search the SM background of the m_{jj} spectrum is established
 1674 through a functional fitting procedure applied to the data. Refs. [?, ?, ?, ?, ?, ?, ?]) have
 1675 found that a parametric function of the form

$$f(x) = p_1(1-x)^{p_2}x^{p_3+p_4\ln x+p_5(\ln x)^2}, \quad (6.26)$$

1676 where $x \equiv m_{jj} / \sqrt{s}$, accurately describes dijet mass distribution predicted by leading and
 1677 next-to-leading-order QCD Monte Carlo. In the ATLAS Run 2 analysis with 139.0 fb^{-1}
 1678 of data [?, ?], the four parameter version of the function ($p_5 = 0$) was found to sufficiently
 1679 described the data. The introduction of gluon tagging may require more parameters to
 1680 properly describe the full invariant mass spectrum.

1681 To avoid introducing any potential bias due to the selection of a specific background
 1682 function, an alternative functional form is employed. This alternative form is inspired by
 1683 the one used by the UA2 experiment [?, ?] when observing the decay of W and Z bosons
 1684 into two jets, followed by a subsequent search.

$$f(x) = p_1 x^{p_2} \exp(p_3 x + p_4 x^2). \quad (6.27)$$

1685 **6.5.4 Analysis Strategy**

1686 The analysis begins with the utilization of skimmed ntuples, which are the result
 1687 of applying the event selection criteria outlined in Section 6.4.3. These ntuples serve as
 1688 the basis for generating pseudo-data using the background-only model. Subsequently,
 1689 a 4-parameter ($p_5 = 0$) fit function described by Equation 6.26 is employed to fit this

1690 pseudo-data. The fit to the data is deemed satisfactory if it meets the following criterion:

- 1691 • Global χ^2 p -value > 0.05

1692 If the conditions mentioned above are satisfied, the background is chosen for the
 1693 purpose of upper limit estimations. Conversely, if the criteria are not met, the 5-parameter
 1694 version of Equation 6.26 is employed for background fitting and is subjected to the same
 1695 selection criterion. If the fit using the 5-parameter function also fails to meet the cri-
 1696 teria, the analysis reduces the range of the window and repeats the fitting process with
 1697 the 5-parameter function to see if a satisfactory fit can be achieved. If this attempt still
 1698 does not meet the criteria, the analysis switches to an alternative option for generating
 1699 pseudo-data. Once a fit satisfying the criteria is obtained, the fit function undergoes var-
 1700 ious validation tests to ensure the appropriateness of the fit strategy. The flowchart of
 1701 Figure 6.76 shows the analysis strategy.

1702 **6.5.5 Spurious Signal Tests**

1703 The spurious signal test is designed to estimate the difference between the signal
 1704 yields from the fit and the expected signal yields that given by fitting a known template
 1705 signal model on a smooth background distribution. Such difference is considered as fit
 1706 bias and defined as S_{spur} :

$$S_{\text{spur}} = S_{\text{fit}} - S_{\text{template}} \quad (6.28)$$

1707 It is crucial to verify the stability of the fit when applied to a background-only
 1708 distribution. In this context, no signal is intentionally introduced into the yields, ensuring
 1709 that the extracted number of signal events remains zero. In the spurious signal test, S_{spur}
 1710 is determined by fitting a model comprising both signal and background components
 1711 onto a background-only template. The corresponding uncertainty from the fit is denoted
 1712 as σ_{fit} . Both the spurious signal S_{spur} and its associated uncertainty σ_{fit} are expected to be
 1713 consistent with zero.

1714 The estimation of the spurious signal is consequently conducted through these pseudo-
 1715 experiments. The mean value across all experiments is calculated, and a total of 100
 1716 pseudo-experiments have been employed. For each individual signal hypothesis, the
 1717 assessment of spurious signals is conducted at various mass points. This is done in-
 1718 dividually for each signal hypothesis and at each mass point. The outcomes of the

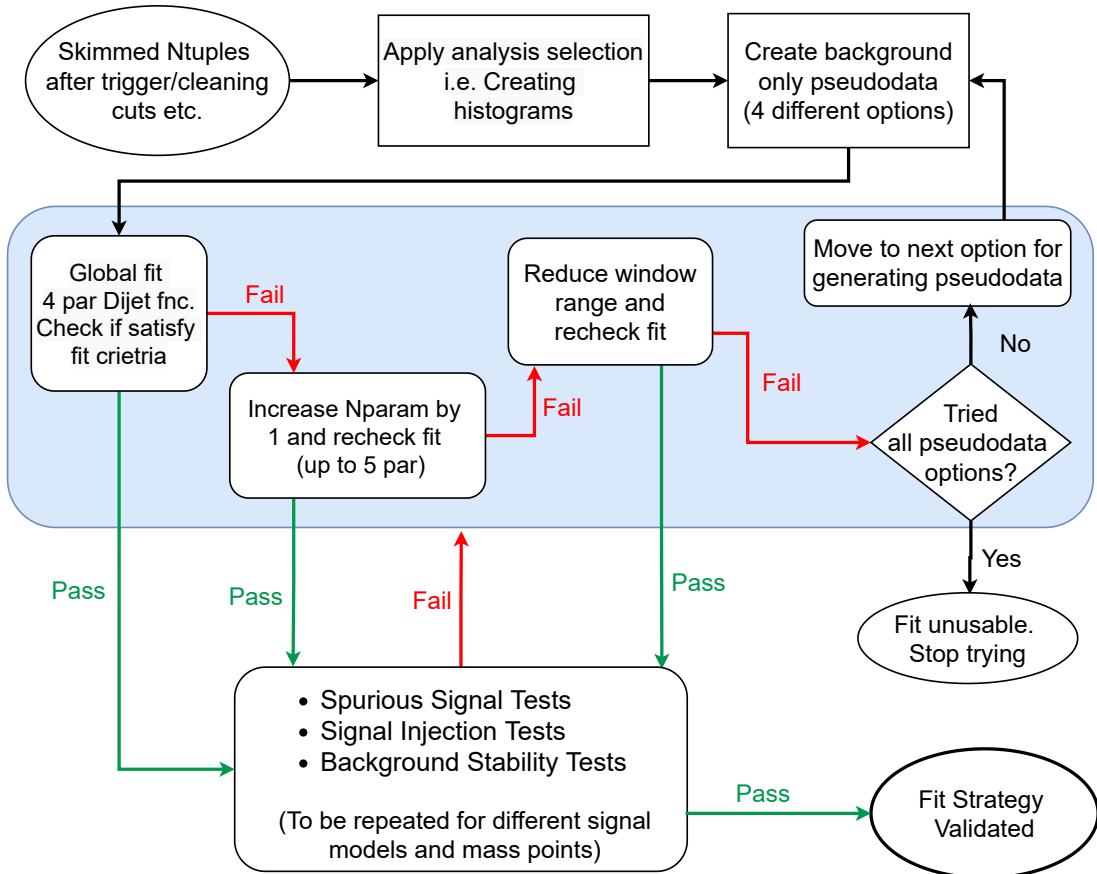


Figure 6.76 Analysis top-level flowchart.

1719 model-independent tests for Gaussian signals, considering different masses and widths,
 1720 are consolidated in Table 6.35 for the 1 gluon-tagged category and in Table 6.36 for the
 1721 2 gluon-tagged category. Correspondingly, the findings for string signals characterized
 1722 by different string scales are presented in Table 6.37.

1723 Following the recommendations of the Statistical PUB Note [?], the spurious signal
 1724 is required to be

$$S_{\text{spur}} < (20\% - 50\%) \sigma_{\text{fit}} \quad (6.29)$$

1725 The idea criteria is when the spurious signal satisfy: $S_{\text{spur}} < 30\% \sigma_{\text{fit}}$, but can be
 1726 loosen up to 50% σ_{fit} . Most of the tested mass points and widths satisfy the spurious
 1727 signal criteria.

Mass TeV	Width percentage [%]	Median ± Rms S_{spurious} ± Uncertainty	Ratio $S_{\text{spurious}}/\text{Uncertainty}$
2	5	0.19 2 ± 802.85 2	2.36E-042
2	10	3.35 2 ± 1313.792	2.55E-032
2	15	154.92 2 ± 1666.6 2	0.093 2
3	5	1.76 2 ± 249.13 2	7.06E-032
3	10	82.55 2 ± 520.85 2	0.158 2
3	15	344.74 2 ± 803.85 2	0.429 2
4	5	48.42 2 ± 112.34 2	0.431 2
4	10	115.89 2 ± 200.83 2	0.577 2
4	15	2.02 2 ± 242.15 2	8.34E-032
5	5	0.021 2 ± 31.77 2	6.61E-042
5	10	0.012 2 ± 31.96 2	3.75E-042
5	15	0.006 2 ± 18.98 2	3.16E-042
6	5	7.82E-042 ± 5.54 2	1.41E-042
6	10	2.84E-042 ± 5.93 2	4.79E-052
6	15	3.62E-042 ± 5.79 2	6.25E-052
7	5	8.65E-042 ± 2.66 2	3.25E-042
7	10	1.6E-04 2 ± 2.59 2	6.18E-052
7	15	8.34E-052 ± 2.71 2	3.08E-052

Table 6.35 Spurious Signal tests using Gaussian signals for 1 gluon tagged category.

Mass TeV	Width percentage [%]	Median ± Rms $S_{\text{spurious}} \pm \text{Uncertainty}$	Ratio $S_{\text{spurious}}/\text{Uncertainty}$
2	5	179.84 2 ± 635.08 2	0.283 2
2	10	757.07 2 ± 1265.99 2	0.598 2
2	15	1666.24 2 ± 2126.08 2	0.784 2
3	5	1.83E-032 ± 85.31 2	2.14E-05 2
3	10	0.27 2 ± 125.63 2	2.15E-03 2
3	15	0.021 2 ± 113.74 2	1.85E-04 2
4	5	1.91E-032 ± 25.6 2	7.46E-05 2
4	10	3.55E-032 ± 38.68 2	9.18E-05 2
4	15	1.50E-032 ± 27.01 2	5.55E-05 2
5	5	2.72E-042 ± 7.13 2	3.81E-05 2
5	10	9.99E-052 ± 5.57 2	1.79E-05 2
5	15	2.1E-04 2 ± 4.72 2	4.45E-05 2
6	5	1.37E-042 ± 1.92 2	7.14E-05 2
6	10	1.47E-042 ± 3.25 2	4.52E-05 2
6	15	6.49E-052 ± 2.59 2	2.51E-05 2
7	5	1.88E-042 ± 1.19 2	1.58E-04 2
7	10	1.17E-042 ± 1.17 2	1.0E-04 2
7	15	7.83E-052 ± 1.20 2	6.53E-05 2

Table 6.36 Spurious Signal tests using Gaussian signals for 2 gluon tagged category.

String scale TeV	Median ± Rms	Ratio
	S_{spurious} ± Uncertainty	$S_{\text{spurious}}/\text{Uncertainty}$
7	4.12E-042 ± 5.832	7.07E-052
7.5	1.6E-042 ± 3.722	2.84E-052
8	6.77E-052 ± 2.112	3.21E-052
8.5	3.83E-052 ± 1.842	2.08E-052
9	3.87E-052 ± 1.932	2.01E-052

Table 6.37 Spurious Signal tests using String signals.

 1728 **6.5.6 Fit Stability Tests**

1729 The fit stability tests are employed to assess the behaviour of the background fit
 1730 function under different scenarios: when applied to the background-only template and
 1731 the signal + background template. A comparison is made between the fit results obtained
 1732 from these two templates. Ideally, the background fit function should yield consistent
 1733 outcomes in both cases. The results of these fit stability tests are presented in Table 6.38
 1734 through Table 6.39, encompassing various signal strengths and mass points.

1735 Notably, the background estimation derived from the signal + background fit (B_1)
 1736 aligns with the background estimation obtained from the background-only fit (B_2), indi-
 1737 cating good agreement between the two approaches.

Mass (TeV)	Width (percentage)	Signal Strength	B_1 from S+B fit	B_2 from B-only fit
			Mean \pm Rms	Mean \pm Rms
2	5	1	20062716.452 \pm 4370.572	20064025.612 \pm 4003.072
2	5	3	20063730.272 \pm 4882.092	20067248.182 \pm 4003.142
2	5	5	20062961.532 \pm 4521.622	20070470.902 \pm 4003.362
5	5	1	20062414.492 \pm 4005.802	20062458.642 \pm 4003.052
5	5	3	20062420.852 \pm 4002.942	20062547.112 \pm 4003.092
5	5	5	20062420.962 \pm 4002.822	20062635.822 \pm 4003.252
5	10	1	20062435.182 \pm 4010.372	20062483.502 \pm 4002.872
5	10	3	20062448.752 \pm 4007.222	20062622.262 \pm 4002.952
5	10	5	20061413.122 \pm 3682.052	20062761.082 \pm 4003.122
7	5	1	20062420.382 \pm 4002.682	20062420.292 \pm 4002.982
7	5	3	20062422.562 \pm 4002.862	20062432.082 \pm 4003.082
7	5	5	20062422.862 \pm 4002.982	20062444.092 \pm 4003.202

Table 6.38 Fit Stability tests using Gaussian signals for 1 gluon tagged category.

Mass (TeV)	Width (percentage)	Signal Strength	B_1 from S+B fit		B_2 from B-only fit	
			Mean ± Rms	Mean ± Rms	Mean ± Rms	Mean ± Rms
2	5	1	3901512.922 ± 2163.272	3902240.712 ±	2048.042	
2	5	3	3901530.762 ± 2166.982	3903253.552 ±	2047.372	
2	5	5	3901621.902 ± 2291.012	3905032.952 ±	2050.682	
5	5	1	3901529.752 ± 2049.312	3901559.922 ±	2046.182	
5	5	3	3901528.522 ± 2049.152	3901589.412 ±	2044.932	
5	5	5	3901533.992 ± 2047.482	3901621.882 ± 3901586.682		
5	10	1	3901536.862 ± 2047.402	3901566.442 ±	2048.232	
5	10	3	3901535.712 ± 2054.622	3901616.492 ±	2050.262	
5	10	5	3901538.472 ± 2049.542	3901670.562 ±	2047.942	
7	5	1	3901531.272 ± 2047.302	3901538.452 ±	2049.162	
7	5	3	3901540.722 ± 2068.732	3901542.752 ±	2048.462	
7	5	5	3901533.132 ± 2052.642	3901540.092 ±	2048.942	

Table 6.39 Fit Stability tests using Gaussian signals for 2 gluon tagged category.

1738 **6.6 Systematic uncertainties**

1739 **6.6.1 String resonance systematic uncertainties**

1740 As described in Section 4.2, JES and JER systematic uncertainties are considered
1741 for the String resonances. In this study, three NPs from the JES and 7 NPs from the JER
1742 are studied on the normalised template shapes.

1743 The impact from JES on the signal template is evaluated by comparing the nominal
1744 distribution to the distribution from each JES NP. The impact from JER on the signal
1745 template is estimated by examining the shift in the RMS (or standard deviation) of the
1746 distribution from each JER NP. Such signal shifts are parameterised by fitting a Gaus-
1747 sian function to the most significant bins surrounding the maximum mean value of the
1748 distribution.

1749 Figure 6.77 shows an example for the $M_s = 8$ TeV signal sample. This histogram
1750 exemplifies one of the systematic variations employed in the subsequent limit calcula-
1751 tion. Among the various systematic sources, GroupedNP_3 emerges as having the most
1752 substantial impact, leading to a significant shift in the signal mean. Across signal samples
1753 of diverse masses and widths, the reconstructed peak of the signal demonstrates a shift
1754 towards lower values in comparison to the generated peak, amounting to approximately
1755 $0.92 \times M_s$. It is important to note that this shift is present even before accounting for the
1756 JES or JER systematic uncertainties.

1757 In Figure 6.78, the proportional shift in the mean of the m_{jj} distribution attributed
1758 to the JES uncertainty and the relative change in RMS of the m_{jj} distribution due to the
1759 JER uncertainty are depicted. While all the NPs are independently incorporated in the
1760 limit computations, this illustration presents a combined display of the three JES mean
1761 shifts in quadrature and the seven JER resolution differences in quadrature.

1762 The alterations in signal acceptance from the inclusion of JES and JER uncertainties
1763 are combined in quadrature and determined to be less than 0.06%. Such small uncertainty
1764 can be ignored for the signal acceptance.

1765 The shifts in the mean of the signal distributions, resulting from the inclusion of
1766 JES uncertainty, are primarily driven by GroupedNP_3 and amount to less than 4%.
1767 Conversely, the alterations in the RMS of the signal distributions following the incor-
1768 poration of JER uncertainty remain below 1.2%. Among the seven values combined in
1769 quadrature, none exhibit a dominant influence. Notably, the JER uncertainty emerges as

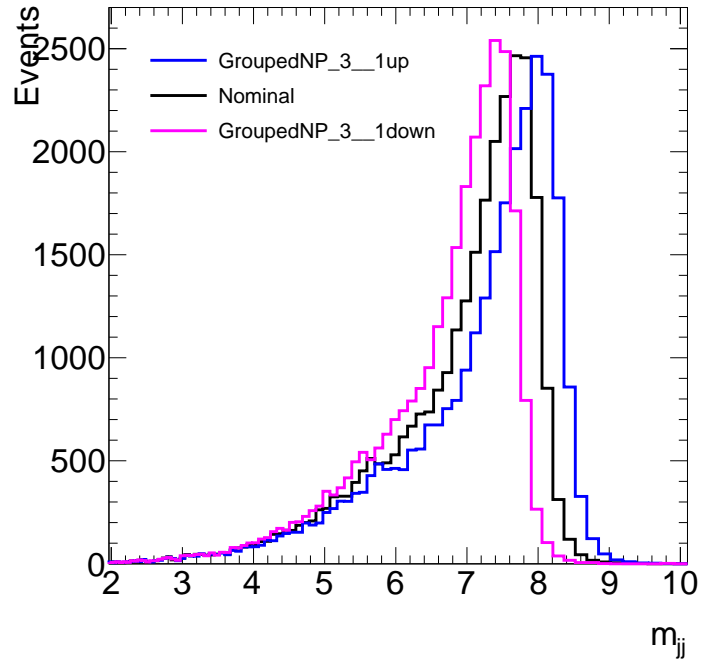


Figure 6.77 m_{jj} distribution for the $M_s = 8$ TeV string sample (nominal). Also shown are the distributions using the jet energy scale GroupedNP_3 one standard deviation up and down systematic uncertainties.

¹⁷⁷⁰ the most substantial source of uncertainty for the lowest M_s signal sample.

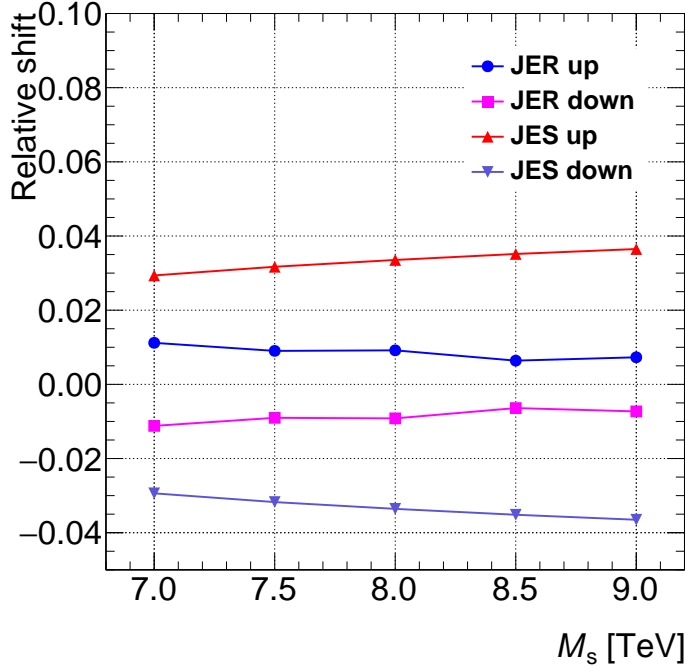


Figure 6.78 Relative shift in the mean of the m_{jj} distributions for each string sample due to jet energy scale uncertainty, and relative change in the RMS of the m_{jj} distributions for each string sample due to the jet energy resolution uncertainty. The changes due to each nuisance parameter group are added in quadrature.

1771 6.6.2 q/g tagging Systematics

1772 6.6.2.1 Pure MC Systematics

1773 Indeed, obtaining uncertainties for a q/g tagger built upon track multiplicity poses
 1774 challenges, particularly in the higher p_T range. This difficulty is partly attributed to the
 1775 limited statistics available beyond 1 TeV, where fewer gluon-jets are present due to their
 1776 tendency to be produced at lower masses compared to quark-jets. Consequently, an issue
 1777 arises in equations that necessitate the average number of tracks in quark- or gluon-jets to
 1778 facilitate calculations. The scarcity of data points at higher p_T values hampers the robust
 1779 estimation of these averages, contributing to the uncertainty challenge in this context.

1780 The determination of the fraction of jets classified as quark- or gluon-initiated jets
 1781 is accomplished through the ratio f_q^f/f_g^c , where the superscript f (c) designates the jet
 1782 with the higher (lower) η value in simulated dijet events. These fractions are derived by
 1783 convolving parton distribution functions with matrix element calculations. The number
 1784 of charged tracks events in the jet with higher η can be described by the following system

1785 of equations [?]:

$$\langle n_{\text{charged}}^f \rangle = f_q^f \langle n_{\text{charged}}^q \rangle + f_g^f \langle n_{\text{charged}}^g \rangle \quad \langle n_{\text{charged}}^c \rangle = f_q^c \langle n_{\text{charged}}^q \rangle + f_g^c \langle n_{\text{charged}}^g \rangle. \quad (6.30)$$

1786 These equations require two samples with different fractions of quark- and gluon-
 1787 jets. While theoretically valid even at high p_T values, their applicability diminishes in the
 1788 high p_T regime due to the exceedingly small fractions of gluon jets. Notably, the main
 1789 sources of uncertainty stem from discrepancies in the MC modelling and the challenges
 1790 associated with reconstructing charged tracks within jets. This is especially relevant as
 1791 the separation between tracks is comparable to the resolution of the detector. Conse-
 1792 quently, the efficiency of the tagger relies on the accurate resolution of tracks for precise
 1793 N_{trk} determination, which in turn is constrained by available statistics.

1794 They systematic uncertainty can be estimated by using pure MC simulations and
 1795 is expected to be substantial, yet smaller than that obtained from data at the edges of
 1796 the mass range. This technique is particularly effective where statistics are not limited,
 1797 such as in the central region of the p_T distribution. Such an approach has proven to be
 1798 the optimal choice. To extend the uncertainties into the higher p_T regime, particle-level
 1799 effects and MC reconstruction effects are incorporated. These uncertainties pertain to
 1800 "in-situ" considerations, making it reasonable to employ them during an extrapolation
 1801 procedure.

1802 The procedure is performed at constant p_T ranges, as N_{trk} depends only on p_T and
 1803 the parton type that initiating jets, uncertainties can be computed by comparing the dis-
 1804 tribution of N_{trk} in bins of jet p_T , which generated from different simulation models.
 1805 Thus different type of MC generators could introduce underlying uncertainties to the re-
 1806 sults. Details on different types of uncertainties and the samples used to estimate them
 1807 are described in Section 5.7. Six working points (10%, 25%, 40%, 50%, 60% and 75%)
 1808 are provided for fixed efficiency curves.

1809 **6.7 Results**

1810 **6.7.1 Untagged Resonances: Model-independent Gaussian Limits**

1811 One way to demonstrate the search in the analysis is to set limits on the cross-section
1812 of signal modes. Here a model-independent signal as Gaussian are used to expand the
1813 sensitivity of the search to new signals that may be detectable with this analysis but
1814 not currently theoretically described. Besides, a model-independent signal could help to
1815 evaluate and compare the strength of different analyses without bias, as the case where
1816 specific models are applied and leads less sensitive to the search.

1817 Therefore, model-independent limits are produced based on model-independent sig-
1818 nals resonances. Because this analysis is sensitive to the shape of resonance, specific
1819 models with different shapes would influence the results strongly. In general, a model-
1820 independent signal is a good feature of the analysis which verify the ability to distinguish
1821 different signal models, although the model-independent limits are still influenced by the
1822 shape of the resonance in an implicit way. The motivation to choose a Gaussian reso-
1823 nance as a proxy is the fact that it is similar to the ‘average’ signal with specific width.
1824 Besides, the shape of reconstructed jet p_T of any realistic signal without very specific
1825 model is produced approximately as a Gaussian resonance, without applied JER. Hence
1826 it is straightforward to use Gaussian resonances to represent any realistic resonance:

1827 The untagged $y^* < 0.8$, 1-g tagged $y^* < 0.6$ and 2-g tagged $y^* < 0.8$ model-independent
1828 Gaussian limits are shown in fig 6.79, 6.80 and 6.81 respectively, for Gaussians with
1829 width equal to 0, 3, 5, 7, 10 and 15% of their peak position, without systematics in-
1830 cluded.

Search for new phenomena in dijet events

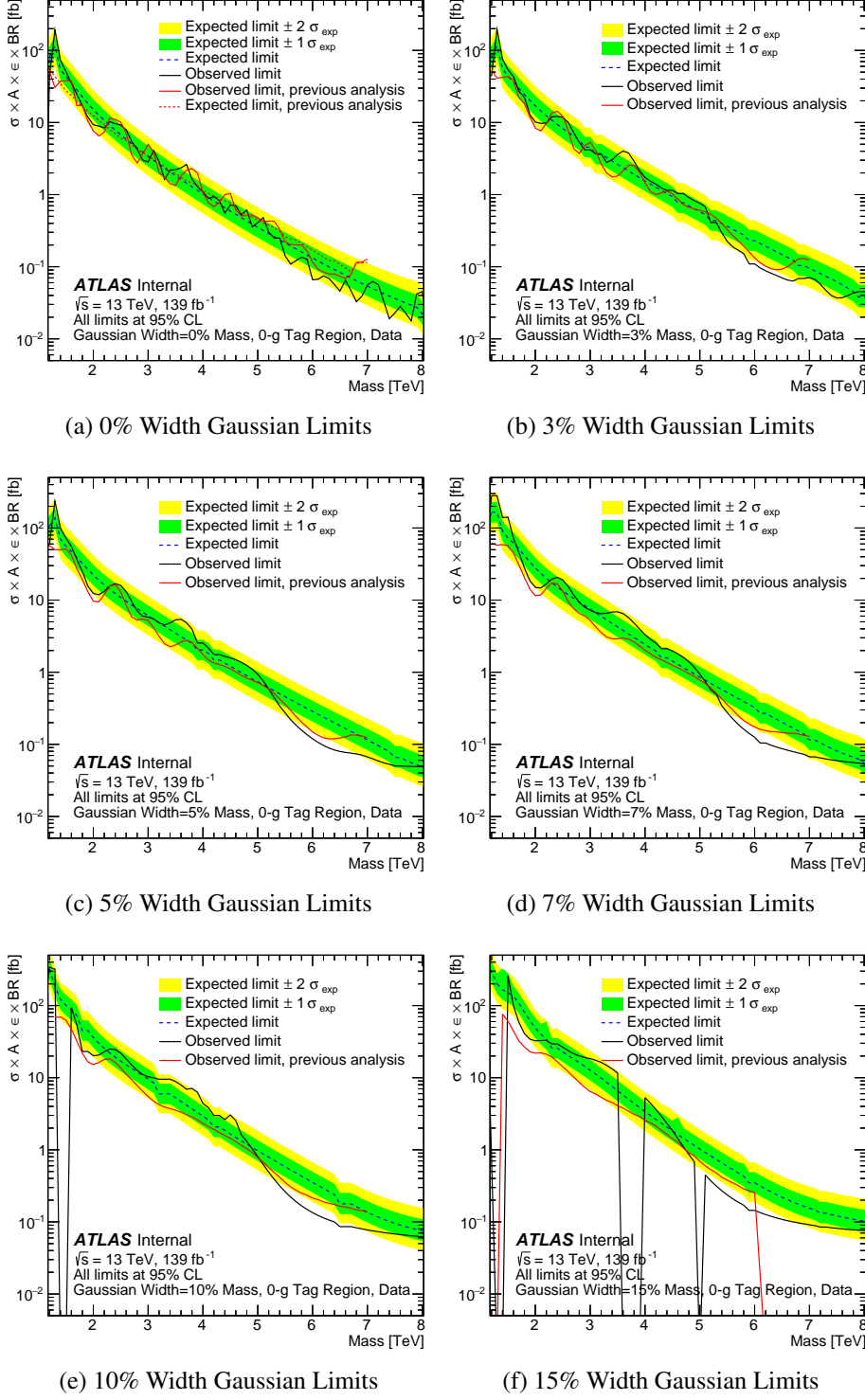


Figure 6.79 Model-independent limits set in the untagged $y^* < 0.8$ Signal Region using Gaussian resonances of varying widths from 0% to 15% of their peak position without systematics included using the full 139fb^{-1} Run-2 dataset.

Search for new phenomena in dijet events

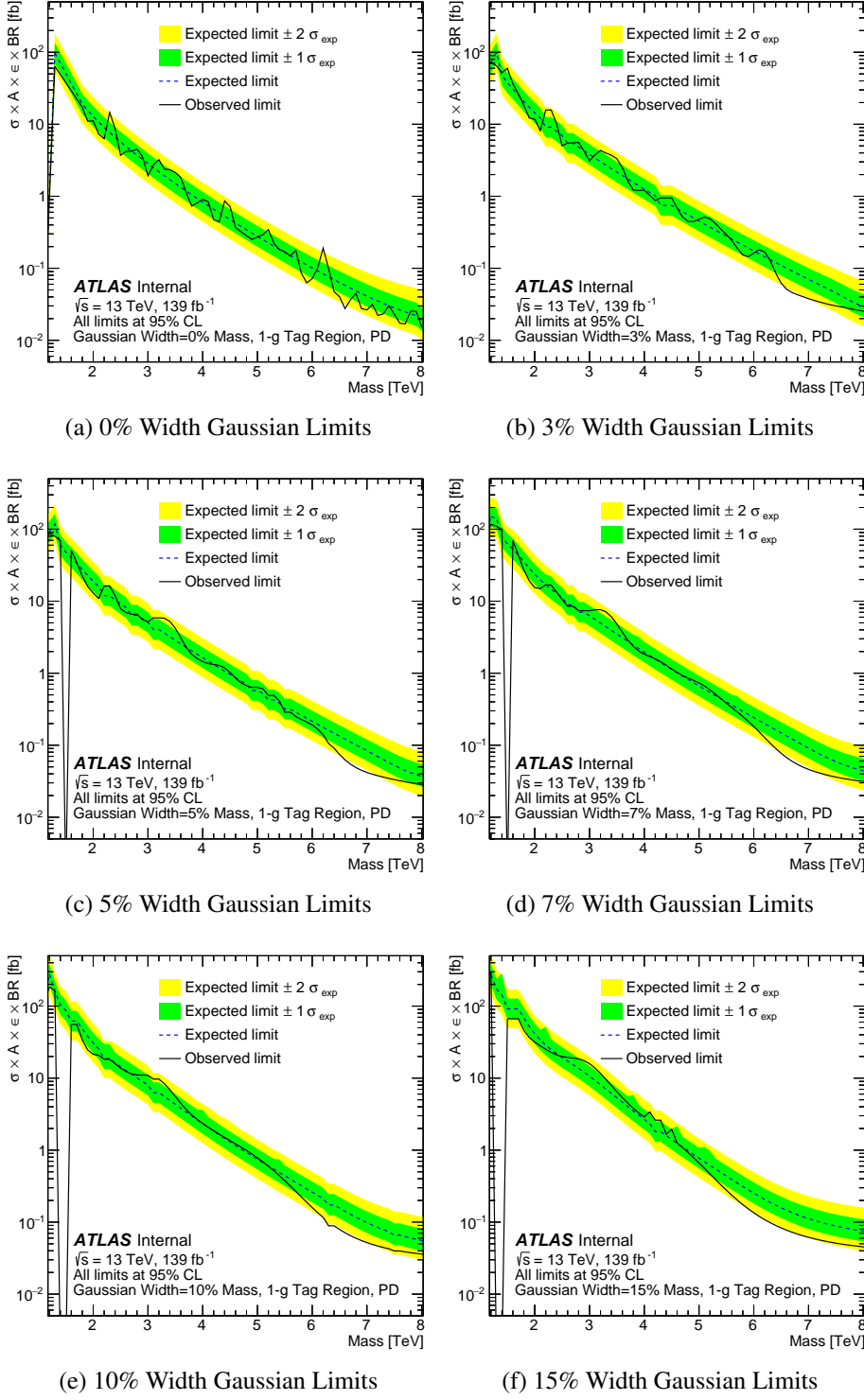


Figure 6.80 Model-independent limits set in the 1-g tagged $y^* < 0.6$ Signal Region using Gaussian resonances of varying widths from 0% to 15% of their peak position without systematics included using the full 139fb^{-1} Run-2 dataset.

Search for new phenomena in dijet events

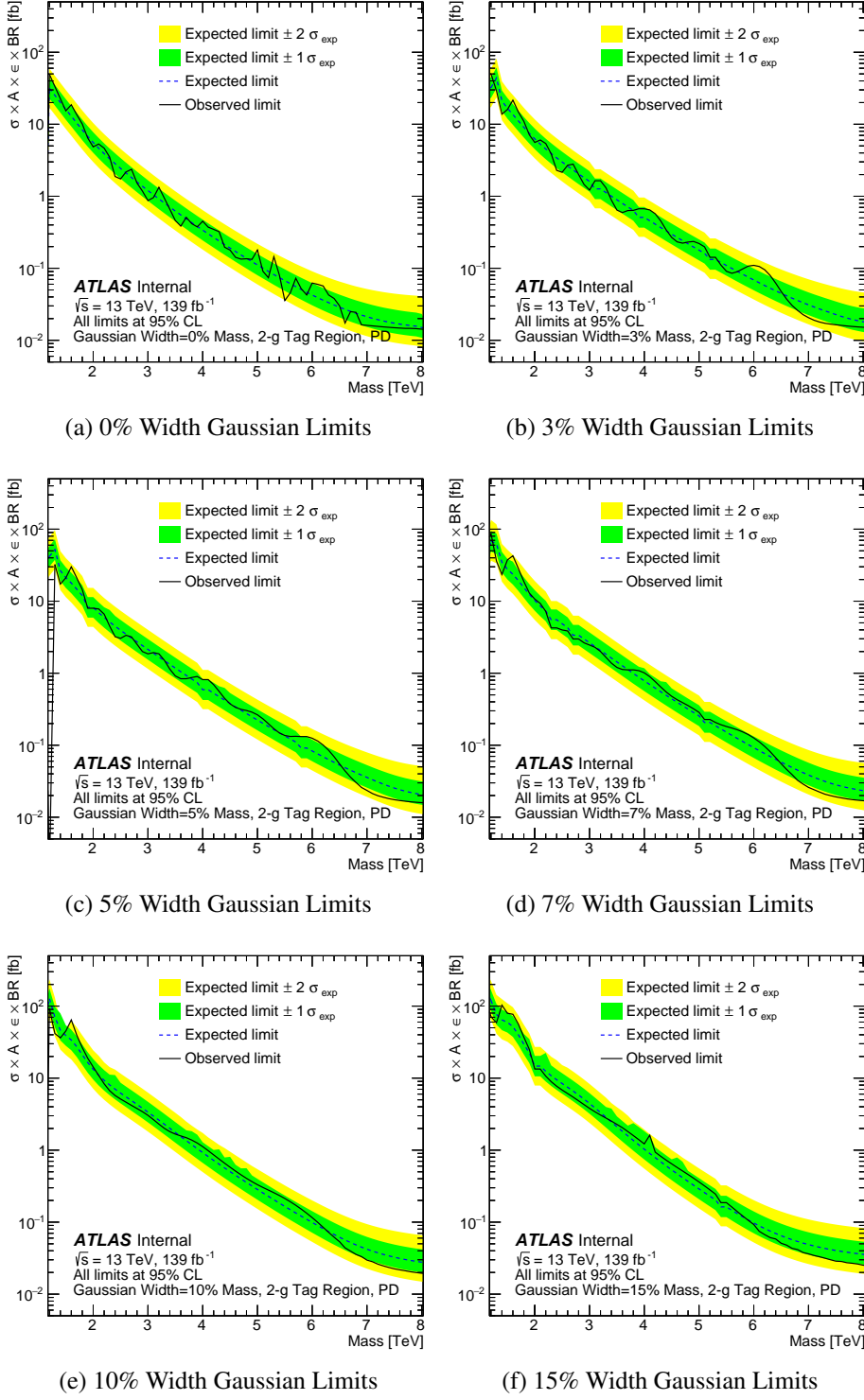


Figure 6.81 Model-independent limits set in the 2-g tagged $y^* < 0.8$ Signal Region using Gaussian resonances of varying widths from 0% to 15% of their peak position without systematics included using the full 139 fb^{-1} Run-2 dataset.

1831

7 Conclusions

1832 From 2015 to 2018, the proton-proton collision at the LHC have achieved an unprece-
1833 dented centre-of-mass energy of $\sqrt{s} = 13$ TeV, with a total integrated luminosity of 140
1834 fb^{-1} that have been recorded by the ATLAS experiment. Such huge amount of collision
1835 data allow scientists test models beyond the SM in a more efficient way, leading a deeper
1836 understanding of physics beyond the SM.

1837 In this thesis, jet taggers are built using the charged multiplicity information pro-
1838 vided by the ID to distinguish quark-initiated and gluon-initiated jets. In order to com-
1839 pensate the data and MC difference, a calibration procedure has been done using matrix
1840 method. Four working points of 50%, 60%, 70%, 80% together with all systematics are
1841 provided so that analyses can use it based on their own interest.

1842 This thesis presents the search for new resonances that potentially decay into a pair
1843 of jets using the data collected by the ATLAS detector during 2015-2018. Resonances
1844 predicted by the BSM can decay into quarks and/or gluons, by introducing jet taggers,
1845 the sensitivity of the search could be significantly increased. In this analysis, searches
1846 are performed on m_{jj} spectrum. Benchmark models H' , String, and QBH are tested, as
1847 well as model-independent Gaussians. Because no significant excess in data are found,
1848 a upper limit is set to each model.